Catalytic Properties, Densification and Mechanical Properties of Nanocrystalline Yttria-Zirconia-based Materials

by

Jianyi Cui

M.S. Intercollege Program of Materials
Pennsylvania State University, 2000

B. E. Materials Science and Engineering
Tsinghua University, 1998

Submitted to the Department of Materials Science and Engineering
in Partial Fulfillment of the Requirements for the Degree of

Doctor of Philosophy in Structural and Environmental Materials

at the

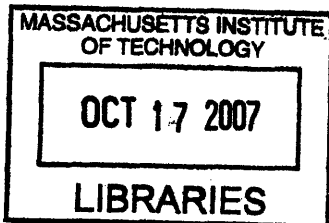MASSACHUSETTS INSTITUTE OF TECHNOLOGY

June 2007

Author:_____
Department of Materials Science and Engineering
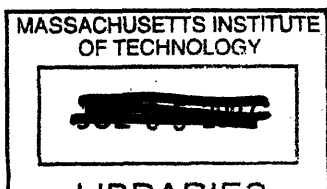April 10, 2007

Certified by:_____
Prof. Jackie Y. Ying
Adjunct Professor of Chemical Engineering
Thesis Supervisor

_____
Prof. Harry L. Tuller
Professor of Ceramics and Electronic Materials
Thesis Reader

Accepted by:_____
Prof. Samuel M. Allen
POSCO Professor of Physical Metallurgy
Chairman, Departmental Committee on Graduate Students

Catalytic Properties, Densification and Mechanical Properties of Nanocrystalline Yttria-Zirconia-based Materials

by

Jianyi Cui

M.S. Intercollege Program of Materials
Pennsylvania State University, 2000

B. E. Materials Science and Engineering
Tsinghua University, 1998

Abstract

Alumina, titania, ceria and manganese oxide were either coated onto or doped in cubic 7 mol% Y_2O_3-ZrO_2 (7YZ) nanocrystals to form nanocomposites for methane combustion. These novel catalysts were very active and thermally stable. In particular, 25 wt% Mn_2O_3-coated 7YZ and 25 wt% Mn_2O_3-doped 7YZ showed remarkably low light-off temperatures of 375°C and 358°C, respectively. These catalysts were highly attractive as they were competitive with the much more expensive supported noble metal catalysts. Their catalytic activity could be attributed to the availability of active surface oxygen species, which facilitated the methane activation at low temperatures.

Nanocrystalline 3 mol% and 8 mol% Y_2O_3-ZrO_2 (3YZ and 8YZ) were successfully densified with an ultrafine grain size of < 90 nm by pressureless sintering at 1100°C and 1150°C, respectively. The low-temperature sinterability could be attributed to the well-defined nanocrystalline particles obtained via hydrothermal synthesis, and the effective elimination of secondary porosity through the dry compact processing. Submicron-sized 3 mol% Y_2O_3-ZrO_2 ceramics with a grain size of ~ 150 nm was also obtained with commercial TOSOH© powders. Grain growth during densification of TOSOH© powders was successfully suppressed by presintering to 93% density under an argon atmosphere, followed by hot isostatic pressing at a temperature lower than the presintering temperature.

The grain sizes of dense 3YZ and 8YZ ceramics were controlled between 100 nm and 5 μm. This allowed for the systematic study of 3YZ and 8YZ in indentation hardness, Young's modulus and fracture toughness as a function of grain size through micro-indentation and instrumented nano-indentation. The Hall-Petch effect was found to be extended to the nanocrystalline regime for 3YZ. 8YZ showed the Hall-Petch effect only in the micrometer and submicrometer regime. Maximum H_V values of 19 and 20 GPa

were achieved for 3YZ and 8YZ, respectively. A continuous decrease in Young's modulus with decreasing grain size was observed in both 3YZ and 8YZ. This could be partially explained by the percolation theory. Transgranular fracture was observed in 3YZ as the grain size approached ~ 100 nm. This was in contrast with the dominant intergranular fracture mode observed in ceramics with fine grain sizes. Transgranular fracture was found in 8YZ over an even broader range of grain sizes (150 nm to 5.0 μm). A significant reduction in fracture toughness from 7.9 MPa·m$^{-1/2}$ to 3.1 MPa·m$^{-1/2}$ was observed as the grain size was reduced from 1.1 μm to 100 nm in 3YZ. Fracture toughness was much lower for 8YZ than for 3YZ, and showed little dependence on grain size. The stability of tetragonal phase at small grain sizes could account for the considerable reduction in the fracture toughness in 3YZ, and the transgranular fracture mode as grain size approached 100 nm.

Thesis Supervisor: Jackie Y. Ying
Title: Adjunct Professor of Chemical Engineering

Acknowledgments

I wish to express my special thanks to all my friends at MIT and from Tsinghua University, especially Hong He, my ACCA friends, and Miao Jin for their friendship.

Last but not least, I thank my family profoundly for their love and encouragements. I am very fortunate to have my parents, Quan Huang and Shikun Wang, and my brother and sister-in-law, Jianfeng Huang and Yongxiang Qin, always there for me. My husband, Dr. Hao Wang, who went through all the tough and good times with me over the past nine years, has been a wonderful partner and colleague. This thesis would not have been completed without the support of my family.

Table of Contents

List of Figures

9

11

List of Tables

13

Chapter 1 – Background and Research Motivation

1.1 Synthesis of Yttria-Zirconia-based Methane Combustion Catalysts

Compared to other forms of fossil fuels, natural gas is a very important source of clean energy (Table 1.1) as it allows for the reduction of unwanted combustion by-products, such as NO_x, SO_2 and ash particles. The U.S. Energy Information Administration has forecasted natural gas as the fastest growing primary energy source worldwide over the period of 2002–2025. The global consumption of natural gas is projected to rise by 70%.[1]

Table 1.1 Fossil fuel emission levels in pounds per billion BTU of energy input.[2]

Pollutant	Natural Gas	Oil	Coal
Carbon Dioxide	117,000	164,000	208,000
Carbon Monoxide	40	33	208
Nitrogen Oxides	92	448	457
Sulfur Dioxide	1	1,122	2,591
Particulates	7	84	2,744
Mercury	0	0.007	0.016

Methane is the main component of natural gas (70–90%). Compared to coal, methane produces almost twice the energy content per unit mass of CO_2 emitted due to its low carbon-to-hydrogen ratio. Due to the absence of carbon-carbon bond, methane is the most unreactive hydrocarbon for combustion. A higher flame temperature is required for the stable combustion of methane compared to other hydrocarbons. With the higher combustion temperature, NO_x formation becomes an issue due to the undesired reaction between oxygen and nitrogen in the air feedstream. This environmental pollutant contributes considerably to the greenhouse effects and smog. To achieve high combustion efficiency while minimizing NO_x formation and unburned hydrocarbon emission, catalytic combustion of methane has been examined as a viable alternative to conventional flame combustion.

Besides decreasing greenhouse gas generation through the reduced combustion temperature, flameless combustion provides for (i) fewer constraints on reactor design, and (ii) flexibility of combustion outside the flammability limits of methane. The latter allows for the use of ultralean fuel mixtures (i.e. high air-to-fuel ratios).[3]

The most effective combustion catalysts are noble metals and metal oxides. Nobel metals are used with or without a support (e.g. alumina, zirconia and silica). Of these catalysts, supported palladium oxide shows the best activity at low temperatures ($\sim 300°C$).[4-9] However, it would be deactivated at temperatures above 700°C from the loss of surface area due to both sintering of the support and/or PdO clusters, and the phase transition from PdO to Pd metal.[5] In recent years, PdO/CeO_2 has been developed to further lower the start-up temperature,[10-12] but this catalyst still faces similar challenges at high temperatures.

Various single metal oxides have been studied as alternatives to noble metals. They offer improved thermal stability, while reducing the raw material costs. However, most oxides can not provide satisfactory activity for methane combustion at low temperatures.

Complex metal oxides, such as barium and strontium hexaaluminates,[13-16] perovskites,[17-23] and aluminosilicates,[24] have been evaluated as catalyst supports. They present high surface areas and thermal stability.

This thesis examines yttria-zirconia-based nanocomposites as cost-effective catalysts for methane combustion under high air-to-fuel ratios. By combining the thermal stability and oxygen-exchange capability of yttria-zirconia with the high surface area, high catalytic activity and oxygen-exchange capability of secondary oxides, such as alumina, titania, ceria and manganese oxide, novel combustion catalysts are derived. The structure-property relationships are established for doped and coated yttria-zirconia catalysts. The kinetics of selected yttria-zirconia-based nanocomposites are studied in detail.

1.2 Processing and Sintering of Nanocrystalline Yttria-Zirconia Ceramics

Zirconia has a monoclinic crystal structure at room temperature. Its structure can be modified by doping with ions, such as calcium or yttrium. In particular, 3 mol% yttria-doped zirconia (3YZ, tetragonal structure) and 7–8 mol% yttria-doped zirconia (7YZ or 8YZ, cubic

structure) are widely studied for their high mechanical strength and electrical conductivity, respectively.

Generally, yttria-zirconia powders are prepared by solid-state and solution methods. The latter,[25] which includes precipitation, sol-gel processing[26] and combustion synthesis,[27,28] can be used to achieve mixing of components at the atomic level, and excellent control of particle morphology. It also allows powders with finer and more uniform grain size and particle size to be derived, which are important for both catalytic and ceramic applications. Calcination or hydrothermal treatment[28-30] is used to crystallize yttria-zirconia systems. The latter allows finer crystallite size to be attained.

Yttria-zirconia requires a high sintering temperature (1200–1700°C) due to its high melting temperature (2700°C). Sinterability of ceramics may be improved significantly by reducing the grain size to the nanometer regime.[31] However, elimination of trapped pores in most yttria-zirconia ceramics is accomplished at $\geq$ 1500°C. The high sintering temperature gives rise to rapid grain growth. In order to maintain small grain size while achieving high density, high pressure (hot pressing[28,32] and hot isostatic pressing (HIP)[33]), rapid sintering (fast firing,[27] electric pulse,[34] and microwave sintering[35]), or a combination of both (spark plasma[36,37]) have been employed.

To achieve ceramic densification at lower sintering temperatures, some researchers have suggested starting with a green density of 70–75%.[38] Cold isostatic pressing (CIP) is commonly applied to green compacts to increase the green density.[39,40] Two-step sintering[38] and electrochemical control of the powder suspension by adjusting the zeta potential[41,42] have also been used. However, these methods only give green densities of ~ 50% in most cases, although enhanced final densities have been attained in some systems.

The degree of powder agglomeration is an important factor in the sintering process. Evans[43] and Vasylkiv et al.[29] have pointed out that the inhomogeneous particle packing and the presence of agglomerates would prevent the low-temperature densification of ceramics. To remove such non-uniformity, powders have been subjected to deagglomeration in liquid suspension by casting technique[41] to achieve better packing.

The attempts to control the green density and powder agglomeration have yielded 3YZ ceramics of > 97% dense with grain sizes of < 150 nm at a sintering temperature of ~

1150°C.[29,40] Fully dense nanocrystalline 8YZ was only obtained at extremely high pressures (~ 1 GPa) under spark plasma sintering.[44] Thus, to effectively hinder the final-stage grain growth while reducing the porosity to < 3% remains a challenge, especially for ceramics with simple structures and high melting temperatures, such as yttria-zirconia.

In this work, nanocrystalline yttria-zirconia powders are synthesized with uniform grain and pore size distributions via hydrothemal treatment. Their sinterability is examined and compared to commercial yttria-zirconia powders. Various processing methods are studied to successfully attain nanostructured ceramics with > 99% density.

1.3 Mechanical Properties of Yttria-Zirconia Ceramics

Various studies have examined the relationship between the grain structure of ceramics and composites and their mechanical properties,[45] such as fracture toughness,[46,47] indentation hardness,[48,49] and Young's modulus.[50,51] However, most research has ignored the effect of grain size, or has focused only on grain sizes in the micron regime. The studies on structure-property relationships of structural ceramics have been limited due to the difficulty in achieving dense ceramics[48] without significant grain growth. It would be of great interest to extend such investigations on sintered ceramics with submicron and nanometer grain sizes.

Although refractory ceramics are brittle materials, indentation tests can reveal their local plastic deformation by dislocation slip mechanism. Rice et al.[52] have indicated a Hall-Petch dependence ($H = H_0 + K / \sqrt{D}$, where K is a constant) for ceramics of fine grain sizes (D). Hardness (H) would reach a minimum at intermediate grain size, and then increase again at larger grain sizes (to single crystal values). This trend was demonstrated for yttria-zirconia with grain sizes larger than 1 μm (see Figure 1.1).
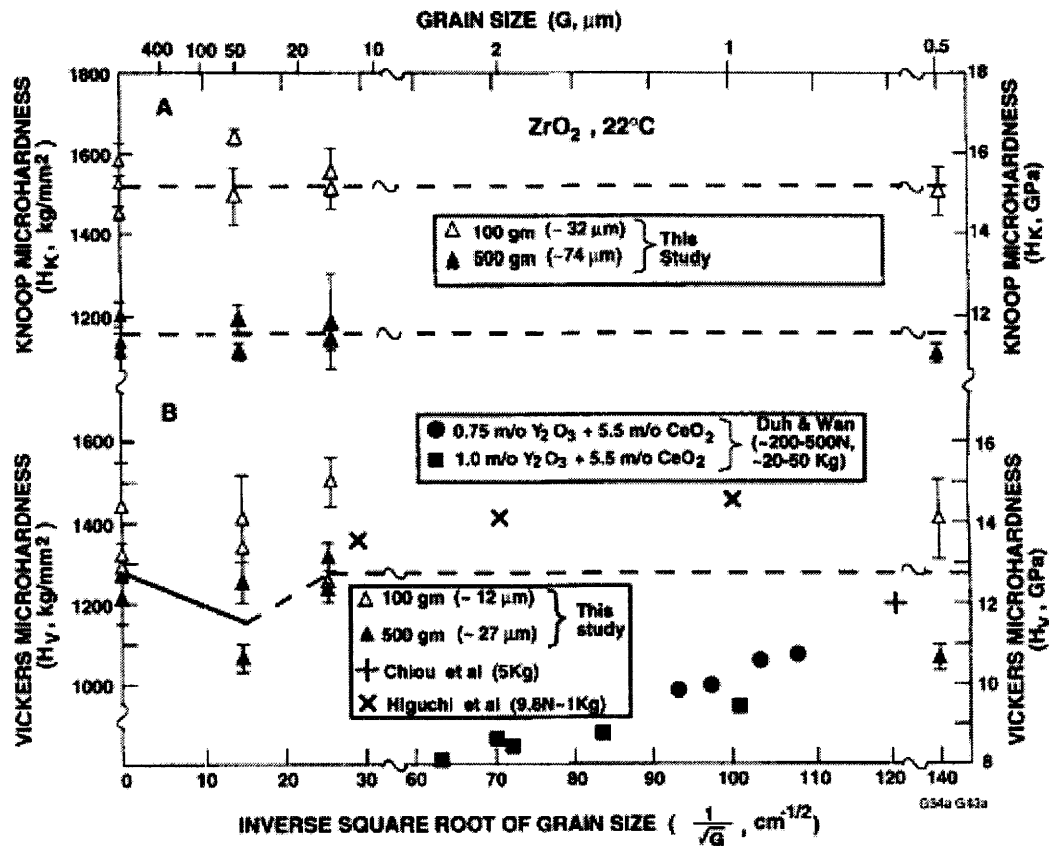
Figure 1.1 Room-temperature hardness vs. $G^{-\frac{1}{2}}$ for ZrO_2.[52]

Indentation leads to two types of fracture modes, transgranular and intergranular. In single crystals, the fracture would propagate along the lower toughness cleavage or the preferred fracture plane that has the lowest energy path (i.e. {110} in cubic zirconia).[45,53] If the transgranular mode also dominates in the polycrystalline materials, the fracture toughness would increase beyond the single crystalline value due to the availability of preferred fracture plane at the fracture tip. This is observed in most ceramics with no complication from anisotropy. When fracture toughness value reaches a local maximum, the influence from grain boundary toughness would emerge. Due to the weaker interaction between atoms in grain boundaries, a lower fracture toughness would then be observed, with intergranular fracture as the dominant fracture mode. In this regime, the relative grain size with respect to fracture length would affect the fractography of the indentation.[54] When $D \ll$ fracture length (c), an intergranular fracture path would be observed. As D approaches c, heavily disrupted pattern would emerge. Transgranular fracture path is found when $D \gg c$.

19

Most studies on the fracture toughness of ceramics made reference to synthesis parameters instead of grain size.[37,48] In the micron regime, some ceramics with cubic structure were reported to exhibit little dependence of fracture toughness on grain size, while some systems showed a local maximum at intermediate grain sizes.

Young's modulus were shown to be essentially constant at large grain sizes, and were reduced significantly at very small grain sizes (< 100 nm).[50,51] However, compared with fracture toughness and indentation hardness, the variation of Young's modulus vs. grain size has not been studied very extensively.

Nanocrystalline yttria-zirconia ceramics have attracted substantial attention due to their high-temperature mechanical and thermomechanical performance. In this thesis, fully densified yttria-zirconia ceramics with controlled grain sizes in the nanometer to micrometer regimes are obtained. They are tested for indentation hardness, Young's modulus and fracture toughness, so that these mechanical properties can be investigated systematically as a function of grain size. Additionally, instrumented indentation is used to provide real-time deformation under various loadings. The indent is analyzed to reveal the fracture modes of the ceramic samples and elucidate their plastic deformation.

1.4 References

[1]Energy Information Administration, *International energy outlook 2005*, July 2005, Report # DOE/EIA-0484(2005) (2005).

[2]Energy Information Administration, *Natural gas 1998: issues and trends*, April 1999, Report # DOE/EIA-0560(98) (1999).

[3]R. E. Hayes, S. T. Kolaczkowski, "Introduction"; pp. 1-95 in *Introduction to Catalytic Combustion*, Gordon and Breach, Australia, (1997).

[4]P. Araya, S. Guerrero, J. Robertson, F. J. Gracia, "Methane combustion over Pd/SiO$_2$ catalysts with different degrees of hydrophobicity," *Appl. Catal. A - Gen.*, 283 [1-2] 225-233 (2005).

[5]O. Demoulin, G. Rupprechter, I. Seunier, B. Le Clef, M. Navez, P. Ruiz, "Investigation of parameters influencing the activation of a Pd/gamma-alumina catalyst during methane combustion," *J. Phys. Chem. B*, 109 [43] 20454-20462 (2005).

[6]L. S. Escandon, S. Ordonez, A. Vega, F. V. Diez, "Oxidation of methane over palladium catalysts: Effect of the support," *Chemosphere*, 58 [1] 9-17 (2005).

[7]M. Faticanti, N. Cioffi, S. De Rossi, N. Ditaranto, P. Porta, L. Sabbatini, T. Bleve-Zacheo, "Pd supported on tetragonal zirconia: Electrosynthesis, characterization and catalytic activity toward CO oxidation and CH_4 combustion," *Appl. Catal. B - Environ.*, 60 [1-2] 73-82 (2005).

[8]S. Guerrero, P. Araya, E. E. Wolf, "Methane oxidation on Pd supported on high area zirconia catalysts," *Appl. Catal. A - Gen.*, 298 243-253 (2006).

[9]K. Persson, A. Ersson, S. Colussi, A. Trovarelli, S. G. Jaras, "Catalytic combustion of methane over bimetallic Pd-Pt catalysts: The influence of support materials," *Appl. Catal. B - Environ.*, 66 [3-4] 175-185 (2006).

[10]V. Ferrer, A. Moronta, J. Sanchez, R. Solano, S. Bernal, D. Finol, "Effect of the reduction temperature on the catalytic activity of Pd-supported catalysts," *Catal. Today*, 107-108 487-492 (2005).

[11]G. Pecchi, P. Reyes, R. Zamora, T. Lopez, R. Gomez, "Effect of the promoter and support in the catalytic activity of Pd-CeO$_2$-supported catalysts for CH_4 combustion," *J. Chem. Technol. Biotechnol.*, 80 [3] 268-272 (2005).

[12]L. H. Xiao, K. P. Sun, X. L. Xu, X. N. Li, "Low-temperature catalytic combustion of methane over Pd/CeO$_2$ prepared by deposition-precipitation method," *Catal. Commun.*, 6 [12] 796-801 (2005).

[13]A. J. Zarur, *Catalytic Combustion of Methane with Nanostructured Barium Hexaaluminate-based Materials*, Ph.D. Thesis, Massachusetts Institute of Technology, Cambridge, MA, (2000).

[14]S. G. Lee, H. Lee, C. H. Lee, J. Y. Kwon, H. C. Park, S. S. Hong, S. S. Park, "Synthesis and catalytic properties of barium hexaaluminates incorporated with chromium and lanthanum," *React. Kinet. Catal. Lett.*, 86 [2] 299-306 (2005).

[15]F. Teng, P. Xu, Z. J. Tian, G. X. Xiong, Y. P. Xu, Z. S. Xu, L. W. Lin, "Synthesis of the high-surface-area $Ce_xBa_{12x}MnAl_{11}O_y$ catalyst in reverse microemulsions using inexpensive inorganic salts as precursors," *Green Chem.*, 7 [7] 493-499 (2005).

[16]J. G. Xu, F. Teng, Z. J. Tian, X. H. Qu, P. Q. Zhang, Y. P. Xu, G. X. Xiong, L. W. Lin, "Novel reverse microemulsion and its application to synthesis of nanostructured $La_{0.95}Ba_{0.05}MnAl_{11}O_{19-\alpha}$ catalyst for methane combustion," *Acta Chim. Sin.*, 63 [24] 2205-2210 (2005).

[17]M. Alifanti, N. Blangenois, M. Florea, B. Delmon, "Supported Co-based perovskites as catalysts for total oxidation of methane," *Appl. Catal. A - Gen.*, 280 [2] 255-265 (2005).

[18]N. H. Batis, P. Delichere, H. Batis, "Physicochemical and catalytic properties in methane combustion of $La_{1-x}Ca_xMnO_{3\pm y}$ ($0 \leq x \leq 1$; $-0.04 \leq y \leq 0.24$)," *Appl. Catal. A - Gen.*, 282 [1-2] 173-180 (2005).

[19]J. D. G. Fernandes, D. M. A. Melo, A. M. G. Pedrosa, M. J. B. Souza, D. K. S. Gomes, A. S. Araujo, "Synthesis and catalytic properties of lanthanum nickelate perovskite materials," *React. Kinet. Catal. Lett.*, 84 [1] 3-9 (2005).

[20]N. Sangar, *Nanocrystalline Perovskites for Catalytic Combustion and Oxygen Separation*, Ph.D. Thesis, Massachusetts Institute of Technology, Cambridge, MA, (2002).

[21]F. He, H. Wang, Y. N. Dai, "Preparation and characterization of $La_{0.8}Cu_{0.2}MnO_{3\pm\delta}$ perovskite-type catalyst for methane combustion," *Trans. Nonferrous Met. Soc. China*, 15 [3] 691-696 (2005).

[22]R. Ran, X. D. Wu, C. Z. Quan, D. Weng, "Effect of strontium and cerium doping on the structural and catalytic properties of $PrMnO_3$ oxides," *Solid State Ion.*, 176 [9-10] 965-971 (2005).

[23]S. Specchia, A. Civera, G. Saracco, "*In situ* combustion synthesis of perovskite catalysts for efficient and clean methane premixed metal burners," *Chem. Eng. Sci.*, 59 [22-23] 5091-5098 (2004).

[24]A. G. Anshits, E. N. Voskresenskaya, E. V. Kondratenko, E. V. Fomenko, E. V. Sokol, "The study of composition of novel high temperature catalysts for oxidative conversion of methane," *Catal. Today*, 42 [3] 197-203 (1998).

[25]J. Y. Ying, T. Sun, "Research needs assessment on nanostructured catalysts," *J. Electroceram.*, 1 [3] 219-238 (1997).

[26]C. J. Brinker, G. W. Scherer, "Particulate sols and gels"; pp. 235-302 in *Sol-Gel Science: The Physics and Chemistry of Sol-Gel Processing*, Academic Press, Boston, MA, (1990).

[27]K. R. Venkatachari, D. Huang, S. P. Ostrander, W. A. Schulze, G. C. Stangle, "Preparation of nanocrystalline yttria-stabilized zirconia," *J. Mater. Res.*, 10 [3] 756-761 (1995).

[28]N. Sangar, J. Y. Ying, To be submitted.

[29]O. Vasylkiv, Y. Sakka, "Synthesis and colloidal processing of zirconia nanopowder," *J. Am. Ceram. Soc.*, 84 [11] 2489-2494 (2001).

[30]T. Tsukada, S. Venigalla, A. A. Morrone, J. H. Adair, "Low-temperature hydrothermal synthesis of yttrium-doped zirconia powders," *J. Am. Ceram. Soc.*, 82 [5] 1169-1174 (1999).

[31]H. Hahn, "Microstructure and properties of nanostructured oxides," *Nanostruct. Mater.*, 2 [3] 251-265 (1993).

[32]Y. M. Chiang, E. B. Lavik, I. Kosacki, H. L. Tuller, J. Y. Ying, "Nonstoichiometry and electrical conductivity of nanocrystalline CeO_{2-x}," *J. Electroceram.*, 1 [1] 7-14 (1997).

[33]J. Li, H. Liao, L. Hermansson, "Sintering of partially-stabilized zirconia and partially-stabilized zirconia-hydroxyapatite composites by hot isostatic pressing and pressureless sintering," *Biomaterials*, 17 [18] 1787-1790 (1996).

[34]M. Yoshimura, T. Ohji, M. Sando, K. Niihara, "Rapid rate sintering of nano-grained ZrO_2-based composites using pulse electric current sintering method," *J. Mater. Sci. Lett.*, 17 [16] 1389-1391 (1998).

[35]D. D. Upadhyaya, A. Ghosh, G. K. Dey, R. Prasad, A. K. Suri, "Microwave sintering of zirconia ceramics," *J. Mater. Sci.*, 36 [19] 4707-4710 (2001).

[36]U. Anselmi-Tamburini, J. E. Garay, Z. A. Munir, A. Tacca, F. Maglia, G. Spinolo, "Spark plasma sintering and characterization of bulk nanostructured fully stabilized zirconia: Part I. Densification studies," *J. Mater. Res.*, 19 [11] 3255-3262 (2004).

[37]U. Anselmi-Tamburini, J. E. Garay, Z. A. Munir, A. Tacca, F. Maglia, G. Chiodelli, G. Spinolo, "Spark plasma sintering and characterization of bulk nanostructured fully stabilized zirconia: Part II. Characterization studies," *J. Mater. Res.*, 19 [11] 3263-3269 (2004).

[38]I. W. Chen, X. H. Wang, "Sintering dense nanocrystalline ceramics without final-stage grain growth," *Nature*, 404 [6774] 168-171 (2000).

[39]W. F. M. G. Zevert, A. J. A. Winnubst, G. S. A. M. Theunissen, A. J. Burggraaf, "Powder preparation and compaction behavior of fine-grained Y-TZP," *J. Mater. Sci.*, 25 [8] 3449-3455 (1990).

[40]W. Li, L. Gao, "Compacting and sintering behavior of nano ZrO_2 powders," *Scripta Mater.*, 44 [8-9] 2269-2272 (2001).

[41]W. H. Rhodes, "Agglomerate and particle-size effects on sintering yttria-stabilized zirconia," *J. Am. Ceram. Soc.*, 64 [1] 19-22 (1981).

[42]A. Krell, P. Blank, H. W. Ma, T. Hutzler, M. P. B. van Bruggen, R. Apetz, "Transparent sintered corundum with high hardness and strength," *J. Am. Ceram. Soc.*, 86 [1] 12-18 (2003).

[43]A. G. Evans, "Considerations of inhomogeneity effects in sintering," *J. Am. Ceram. Soc.*, 65 [10] 497-501 (1982).

[44]U. Anselmi-Tamburini, J. E. Garay, Z. A. Munir, "Fast low-temperature consolidation of bulk nanometric ceramic materials," *Scripta Mater.*, 54 [5] 823-828 (2006).

[45]R. W. Rice, "Grain dependence of microcracking, crack propagation, and fracture toughness at ~ 22°C" and "Grain dependence of indentation hardness at ~ 22°C;" pp. 43-126 and 245-294 in *Mechanical Properties of Ceramics and Composites: Grain and Particle Effects*, Marcel Dekker, New York, NY, (2000).

[46]A. Bravo-Leon, Y. Morikawa, M. Kawahara, M. J. Mayo, "Fracture toughness of nanocrystalline tetragonal zirconia with low yttria content," *Acta Mater.*, 50 [18] 4555-4562 (2002).

[47]N. M. Gokhale, R. Dayal, S. C. Sharma, R. Lal, "Investigation on crystalline phases and mechanical-properties of TZP ceramics prepared from sol-gel powders," *J. Mater. Sci.*, 29 [21] 5709-5714 (1994).

[48]O. Vasylkiv, Y. Sakka, V. V. Skorokhod, "Low-temperature processing and mechanical properties of zirconia and zirconia-alumina nanoceramics," *J. Am. Ceram. Soc.*, 86 [2] 299-304 (2003).

[49]B. Basu, J. H. Lee, D. Y. Kim, "Development of nanocrystalline wear-resistant Y-TZP ceramics," *J. Am. Ceram. Soc.*, 87 [9] 1771-1774 (2004).

[50]R. Chaim, M. Hefetz, "Effect of grain size on elastic modulus and hardness of nanocrystalline ZrO_2-3 wt% Y_2O_3 ceramic," *J. Mater. Sci.*, 39 [9] 3057-3061 (2004).

[51]O. Yeheskel, R. Chaim, Z. J. Shen, M. Nygren, "Elastic moduli of grain boundaries in nanocrystalline MgO ceramics," *J. Mater. Res.*, 20 [3] 719-725 (2005).

[52]R. W. Rice, C. C. Wu, F. Boichelt, "Hardness-grain-size relations in ceramics," *J. Am. Ceram. Soc.*, 77 [10] 2539-2553 (1994).

[53]A. Pajares, F. Guiberteau, A. Dominguez-Rodriguez, A. H. Heuer, "Indentation-induced cracks and the toughness anisotropy of 9.4-mol-percent-yttria-stabilized cubic zirconia single-crystals," *J. Am. Ceram. Soc.*, 74 [4] 859-862 (1991).

[54]G. R. Anstis, P. Chantikul, B. R. Lawn, D. B. Marshall, "A critical-evaluation of indentation techniques for measuring fracture-toughness: I, Direct crack measurements," *J. Am. Ceram. Soc.*, 64 [9] 533-538 (1981).

Chapter 2 – Yttria-Zirconia-based Nanocomposite Catalysts for Methane Combustion

2.1 Introduction

Methane has been proposed as an alternative fuel in many industrial applications since it leads to reduced greenhouse gas generation.[1] Catalytic combustion of methane is attractive as it allows for ultralean combustion (i.e. high air-to-fuel ratios), simplifies the combustor design, and minimizes the emissions of NO_x and unburned hydrocarbons.[2] However, it demands a catalytic material that possesses both low-temperature activity and high-temperature stability.

Zirconia is a unique metal oxide that possesses excellent thermal stability. In addition, yttria-stabilized zirconia is a well-known ionic conductor at elevated temperatures;[3] the oxygen-exchange capability may be useful in catalytic combustion. High surface area yttria-zirconia (YZ) powder has been examined as a heterogeneous catalyst[4] or catalyst support.[5] Such powder typically possesses nanometer-sized grains, and can be prepared by wet-chemical processes (e.g. chemical precipitation and sol-gel processing),[6] and gas-phase synthesis.[7]

The catalytic activity of YZ in methane combustion can be improved physically and chemically through the introduction of highly dispersed dopants and coatings. The secondary components may be metal oxides known for their high surface areas (e.g. Al_2O_3[8-10] and TiO_2[8,9,11]), or for their high catalytic activities and oxygen-exchange capabilities (e.g. Mn_2O_3[12,13] and CeO_2[13-16]). By adding these secondary oxides, enhanced catalytic properties may be achieved through the synergism between the different components.

2.2 Experimental

2.2.1 Synthesis

Nanocrystalline powder of 7 mol% Y_2O_3-ZrO_2 (7YZ) was prepared at room temperature by dissolving $Y(NO_3)_3$ (99.9%, Alfa Aesar) and $ZrOCl_2$ (99.9%, Alfa Aesar) in deionized water at a total cation concentration of 0.4 M. The solution was added to a basic ethanolic solution (C_2H_5OH/H_2O volume ratio ~ 1) of tetraethylammonium hydroxide (TEAH, 35% w/w in water, Alfa Aesar). The concentration of the base solution was 0.4 M.

The secondary component was added by dissolving the Al, Ti, Ce or Mn nitrate in deionized water at a concentration of 0.4 M. The additive was introduced as a dopant to YZ by mixing the additive precursor solution with the YZ precursor solution (see Figure 2.1). It was also coated onto YZ by introducing the additive precursor solution to the YZ precipitate sol after the latter has been aged for 22 h.

```
┌─────────────────┐   ┌─────────────────────────────┐
│  Base Solution  │   │  ZrOCl₂ + Y(NO₃)₃ + H₂O     │
└─────────────────┘   └─────────────────────────────┘
                                            ┌──────────────────────────┐
                         ↓  ←───────────────│  Metal Nitrate (Dopant)  │
                   ┌──────────────────┐     └──────────────────────────┘
                   │  Co-precipitation │
                   │     @ 25°C        │
                   └──────────────────┘
                            ↓
┌──────────────────────────┐  ┌──────────────────┐
│  Metal Nitrate (Coating) │→ │   Aging with     │
└──────────────────────────┘  │  Controlled pH   │
                              └──────────────────┘
                                       ↓
                   ┌──────────────────────────────┐
                   │   Water and Ethanol Washes   │
                   └──────────────────────────────┘
                                   ↓
                       ┌────────────────────┐
                       │    Calcination     │
                       └────────────────────┘
```
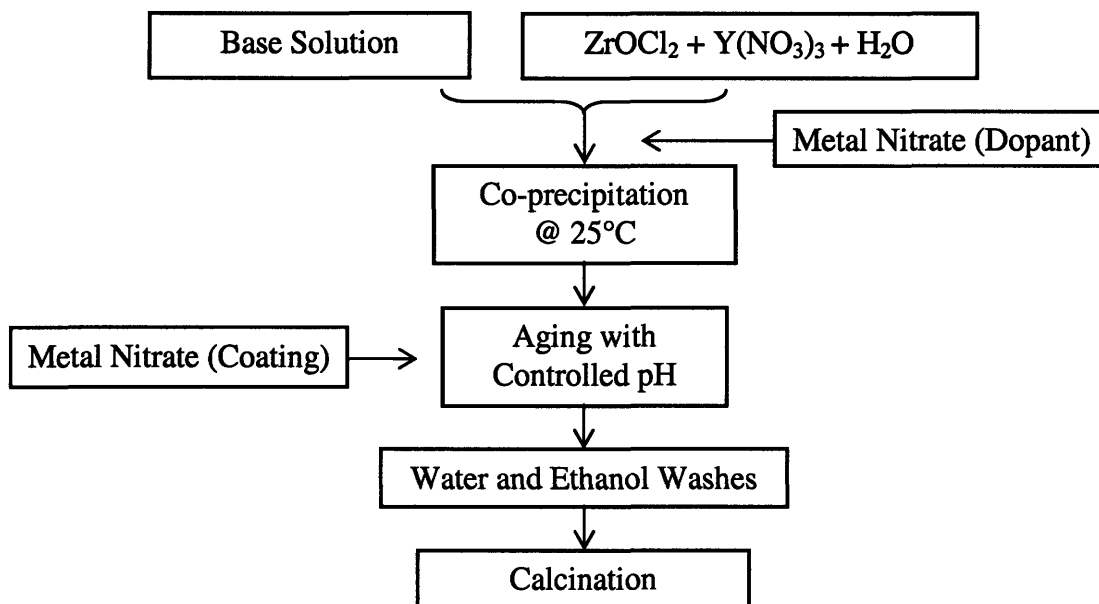
Figure 2.1 Synthesis of YZ-based nanocomposites.

The precipitated sol in all cases was aged for a total of 24 h, centrifuged, washed twice with water/alcohol solution, and washed with ethanol to remove excess base and nitrate salts. The hydroxides were dried overnight at room temperature in air, grounded, and calcined at 550–1000°C in air for 2 h. The calcined powder was then grounded and sieved. Where necessary, the powder was ball-milled for 24 h with 3YZ balls in a polyvinyl alcohol bottle to break up any soft agglomerates before sieving.

The choice of synthesis parameters, such as precursor solution concentration, base solution solvent, aging time, and washing conditions were based on previous studies performed in our group on optimizing the surface area of nanocrystalline powders.[17-20]

2.2.2 Materials Characterization

Surface area of the catalysts was determined by nitrogen adsorption analysis (Micromeritics ASAP 2000) using the 5-point BET (Brunauer-Emmett-Teller) method. Powder X-ray diffraction (XRD) (Siemens D5000 θ-θ diffractometer, 45 kV, 40 mA, Cu-Kα) was used for phase identification and grain size analysis. The volume-averaged crystallite size was calculated based on Scherrer's analysis of the XRD peak broadening. Lattice parameters were calculated in reference to the internal standards (silicon for the Mn-containing systems or silver for the Ce-containing systems). The sample compositions were analyzed by inductively coupled plasma-atomic emission spectroscopy (ICP-AES) (Desert Analytics, Tucson, TX). Powder morphology was investigated with high-resolution transmission electron microscopy (HR-TEM) (JEOL 2010) at 200 kV. The composition and elemental dispersion of the sample were obtained with a Vacuum Generators HB603 Scanning Transmission Electron Microscope (STEM) (250 kV) with energy dispersion X-ray (EDX) spectroscopy. Zeta potential measurements were performed with a Brookhaven Instruments ZetaPALS Zeta Potential Analyzer with 0.01 M of KCl as the supporting electrolyte. The powder suspension was sonicated to break up large agglomerates before analysis. Solution pH was adjusted by adding KOH or HCl, and measured by an Orion 420A pH meter. An Axis Ultra X-ray Photoelectron Spectrometer (XPS) was used to analyze the surface composition and oxidation state of samples.

2.2.3 Catalytic Activity

The activity of the catalysts was evaluated under steady state in a packed bed reactor. 50 mg of catalysts were loaded into a ¼"-O.D. quartz reactor tube, and placed between two quartz wool plugs. To control the reaction temperature accurately, a type-K thermocouple located right below the catalyst bed was used in conjunction with an Omega temperature controller and a Lindberg tube furnace. The gas flow was metered using mass flow controllers (MFC). The catalyst was first pretreated for 30 min at a temperature that was 50°C lower than its calcination temperature in a stream of 1% CH_4 in air at a flow rate of 50 ml/min. Subsequently, the reactor was cooled down to room temperature at a cooling rate of 1.5°C/min in the reactant gas. A gas hourly space velocity of 60,000 h^{-1} was used in all runs.

The exit stream was analyzed at an interval of ~ 30°C with a Hewlett Packard 6890 gas chromatograph (GC) equipped with molecular sieve 5A and Porapak Q chromatographic columns. CH_4, CO, CO_2, O_2 and N_2 were separated effectively and quantified. Carbon balance was achieved within 2% in all runs.

2.2.4 Mechanistic Studies

The investigation of reaction mechanism and the determination of kinetic parameters for catalytic methane oxidation were performed by measuring the apparent reaction rate as a function of methane and oxygen concentrations, while operating under steady-state, differential and reaction-limited conditions. High-purity gases (10% CH_4 in He, 10% O_2 in He, He, O_2 and N_2) were metered into the reactor individually by MFC; N_2 was used as the reference. Typically, the catalyst was pretreated at 50°C below its calcination temperature in 21% O_2 in He at a flow rate of 50 ml/min for 1 h to remove any surface contaminants. The reactor was then cooled to the desired reaction temperature. The reaction rate was calculated as a function of methane and oxygen inlet concentrations. The concentrations of CH_4 and O_2 were varied between 0.5–5% and 5–21%, respectively, to achieve a broad range of CH_4/O_2 stoichiometric ratios φ (0.02–1).

The catalytic property of combustion catalysts would depend strongly on the nature and amount of the oxygen adsorbed on catalyst surface. Thus, the materials were characterized by temperature-programmed desorption (TPD) of oxygen in He. A sample of ~ 300 mg was first pretreated in O_2 at a flow rate of 20 ml/min and 50°C below its calcination temperature for 1 h to remove any surface contaminants. Subsequently, the catalyst was cooled to room temperature, and purged in He until the signal was stabilized. TPD of oxygen was performed up to 750°C (ramp = 5°C/min) in He at a flow rate of 20 ml/min under atmospheric pressure. The exit stream was analyzed with Hewlett Packard 6890 GC equipped with a thermal conductivity detector (TCD).

Temperature-programmed reduction (TPR) of methane was used to characterize catalyst reducibility. A sample of ~ 50 mg was pretreated at 50°C below its calcination temperature in 21% O_2 in He at a flow rate of 20 ml/min for 1 h to remove any surface contaminants. It was then purged in He upon cooling to room temperature. The reducibility of

the catalyst was tested up to 750°C (ramp = 1°C/min) under 0.5% CH_4 in He at a flow rate of 20 ml/min. The exit stream was analyzed with the Hewlett Packard 6890 gas chromatograph at an interval of ~ 30°C. Thermal gravimetric analysis (TGA) of catalyst reduction under 5% CH_4 in He at a flow rate of 20 ml/min was performed with a Perkin Elmer TGA7 up to 550°C (ramp = 1°C/min). The samples were subjected to similar pretreatment as in the TPR studies.

2.3 Results and Discussion

2.3.1 Synthesis of 7YZ-based Nanocrystalline Powders

2.3.1.1 Effect of Precipitation pH on 7YZ

In colloidal chemistry, particle aggregation could be controlled by pH changes. This in turn would affect the surface area of the resulting powder. Figure 2.2 shows the Zeta potential of 7YZ as a function of pH. By precipitating at a pH of ~ 12, a high surface charge was achieved, minimizing particle growth and aggregation. This has led to a high surface area powder (Table 2.1). In contrast, a low pH of 4 gave rise to a much lower surface area, and the poor incorporation of yttrium dopants. Consequently, the resulting zirconia-based material was in the monoclinic phase instead of the desired cubic phase.[21] All further syntheses involved chemical precipitation at a pH of 12.
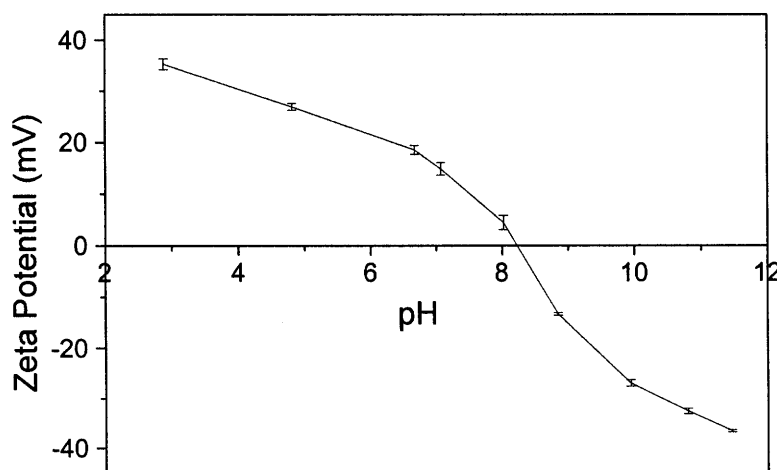
Figure 2.2 Zeta potential profile of as-precipitated 7YZ.

29

Table 2.1 BET surface area of 7YZ precipitated at various pH's and calcined at 600°C in air for 2 h.

Precipitation pH	4	9	12
BET Surface Area (m^2/g)	31	51	61

2.3.1.2 Thermal Evolution of Coated 7YZ

As demonstrated previously on aluminate system by our group,[13] nanocomposites could be formed by coating a secondary metal oxide onto the surface of the preformed primary metal oxide. Such approach could provide for the high dispersion of two separate metal oxides, giving rise to unique chemical and electronic synergistic effects. The secondary metal oxide could also form a coating that would prevent the grain growth and sintering of the primary metal oxide. This would enhance the thermal stability of the system, and help retain the surface area at high temperatures.

XRD patterns of 7YZ coated with 25 wt% of Al_2O_3, TiO_2, CeO_2 and Mn_2O_3 are shown in Figure 2.3 along with uncoated 7YZ. TiO_2, CeO_2 and Mn_2O_3 formed separate phases at this high loading, whereas Al_2O_3 remained highly dispersed as an amorphous phase on 7YZ after calcination at 800°C. In fact, Al_2O_3 XRD peaks were not observed even after calcination at 1000°C. Figure 2.4 shows that 7YZ doped with 25 wt% Al_2O_3, TiO_2, CeO_2 and Mn_2O_3 did not exhibit any secondary phases after calcination at 800°C. Only the cubic zirconia peaks were detected in the doped YZ samples.

Figures 2.5–2.8 illustrate the increase in grain size and the decrease in surface area of coated 7YZ with increasing calcination temperatures. Al_2O_3, TiO_2 and CeO_2 coatings reduced the grain growth and sintering of YZ at high temperatures, especially when high loadings of 20 and 25 wt% were used. 25 wt% of TiO_2 coating was particularly effective at suppressing grain growth at 1000°C; small zirconia crystallites of 18.5 nm were preserved. 25 wt% of TiO_2-coated 7YZ also demonstrated superior surface area at 550°C (224 m^2/g) compared to uncoated 7YZ (from 67 m^2/g).

On the other hand, Mn_2O_3 coating increased the grain size of 7YZ at all calcination temperatures, especially at low Mn_2O_3 loadings. This was in agreement with Kim and Choi's observation that low Mn levels could promote the sintering and grain growth of cubic yttria-

zirconia.[12] The average grain sizes of Mn_2O_3-coated 7YZ samples were too large to be estimated by Scherrer's analysis, which is only valid for grain size below 100 nm. Mn_2O_3 coating improved the surface area of 7YZ at a low calcination temperature of 550°C. However, it was not effective towards suppressing sintering at higher temperatures. At 1000°C, the surface areas of Mn_2O_3-coated 7YZ decreased drastically to less than 2 m^2/g, i.e. below the detection limit of the N_2 sorption analysis.
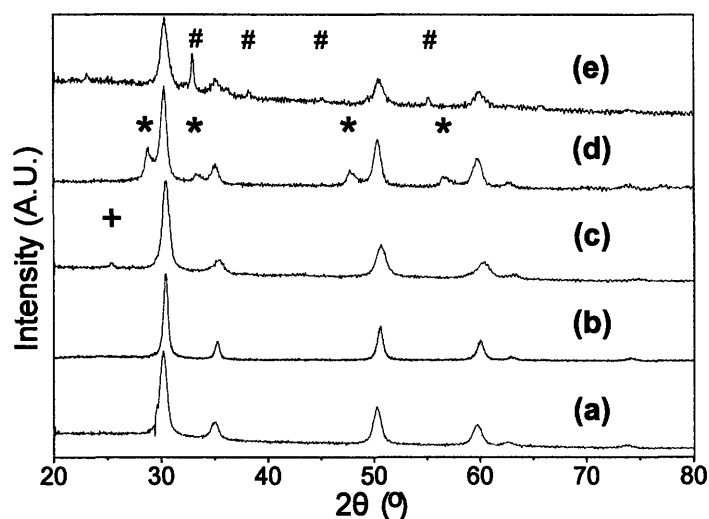
Figure 2.3 XRD patterns of (a) 7YZ, and 7YZ coated with 25 wt% of (b) Al_2O_3, (c) TiO_2, (d) CeO_2 and (e) Mn_2O_3, after calcination at 800°C in air for 2 h. Peaks of TiO_2, CeO_2 and Mn_2O_3 were denoted by +, * and #, respectively.
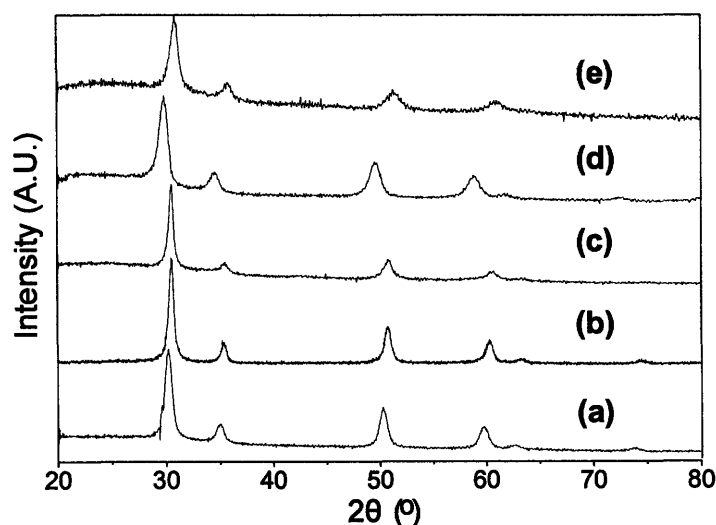
Figure 2.4 XRD patterns of (a) 7YZ, and 7YZ doped with 25 wt% of (b) Al_2O_3, (c) TiO_2, (d) CeO_2 and (e) Mn_2O_3, after calcination at 800°C for 2 h in air.

31
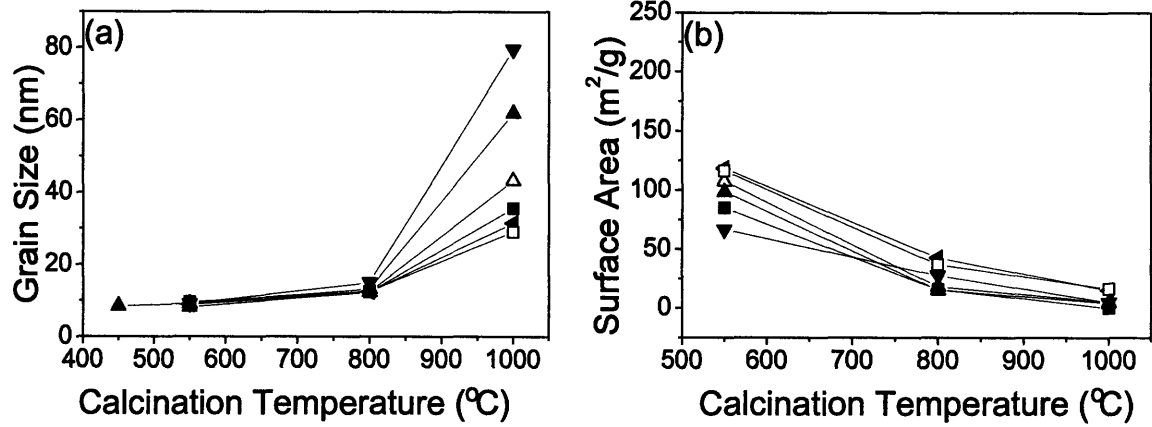
Figure 2.5 (a) Zirconia XRD grain sizes and (b) BET surface areas of 7YZ coated with (▼) 0, (▲) 5, (△) 10, (■) 15, (◄) 20 and (□) 25 wt% of Al_2O_3.
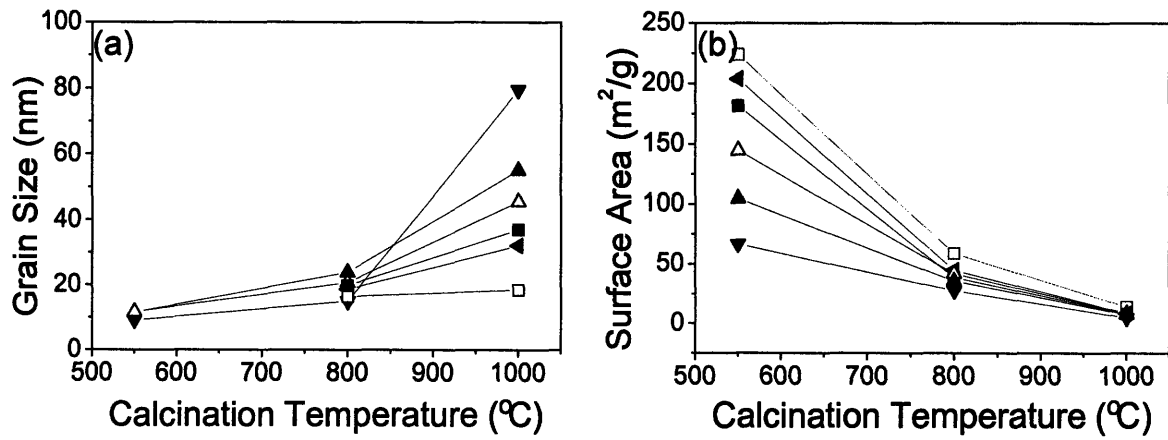
Figure 2.6 (a) Zirconia XRD grain sizes and (b) BET surface areas of 7YZ coated with (▼) 0, (▲) 5, (△) 10, (■) 15, (◄) 20 and (□) 25 wt% of TiO_2.
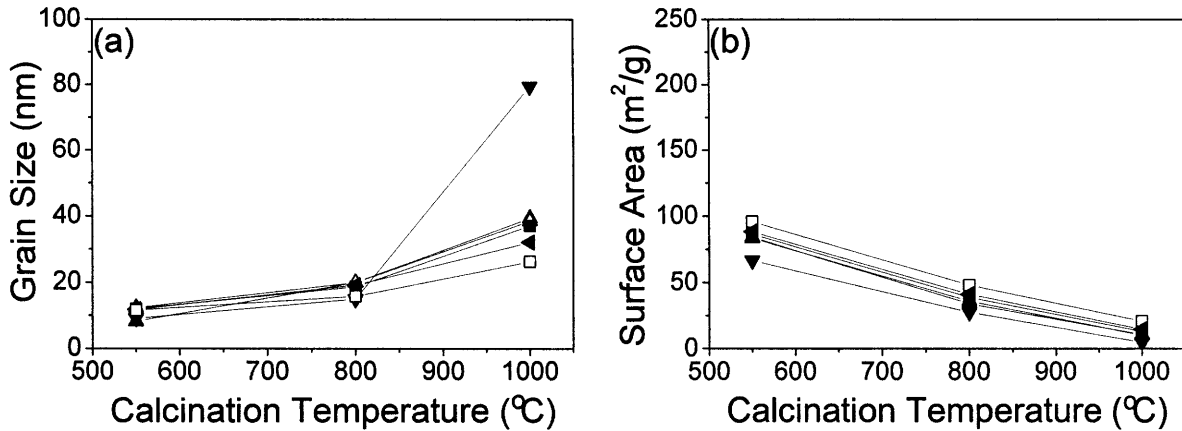
Figure 2.7 (a) Zirconia XRD grain sizes and (b) BET surface areas of 7YZ coated with (▼) 0, (▲) 5, (△) 10, (■) 15, (◄) 20 and (□) 25 wt% of CeO₂.
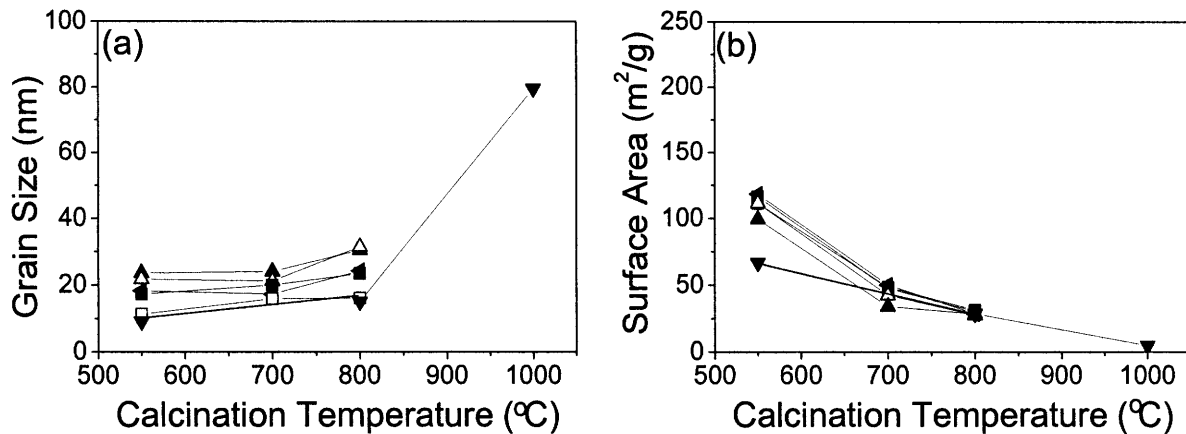
Figure 2.8 (a) Zirconia XRD grain sizes and (b) BET surface areas of 7YZ coated with (▼) 0, (▲) 5, (△) 10, (■) 15, (◄) 20 and (□) 25 wt% of Mn₂O₃.

2.3.2 Catalytic Activities of Coated and Doped 7YZ

Based on the results above, the powders with the highest thermal stability, 7YZ coated with 25 wt% of Al_2O_3, TiO_2, CeO_2 and Mn_2O_3, were selected for catalytic studies in methane combustion. These samples were calcined at 800°C for 2 h in air, and compared with 7YZ doped with 25 wt% of Al_2O_3, TiO_2, CeO_2 and Mn_2O_3.

Figure 2.9 shows that 25 wt% Mn_2O_3-coated 7YZ has the highest catalytic activity in methane combustion. The coatings of 25 wt% of Mn_2O_3 and CeO_2 enhanced the catalytic

activity of 7YZ. In contrast, the coatings of 25 wt% of Al_2O_3 and TiO_2 reduced the catalytic activity of 7YZ, despite improving its thermal stability. These two catalysts also did not fully combust the methane, generating CO as an undesired by-product (Figure 2.10).
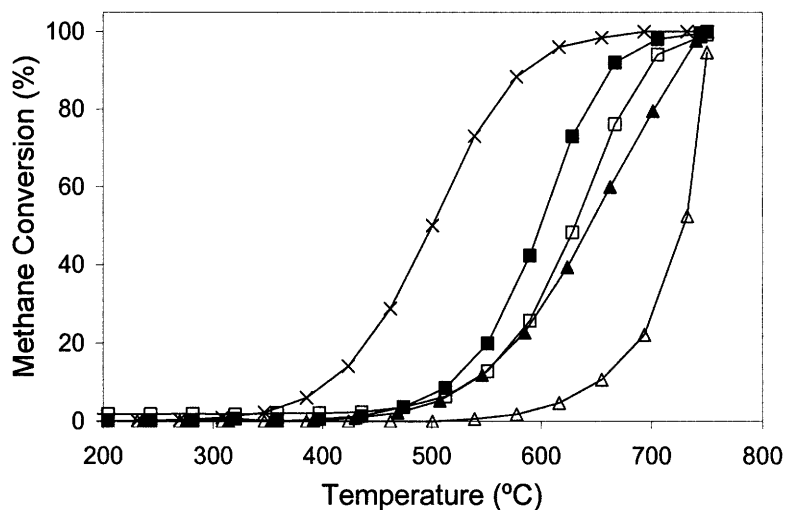
Figure 2.9 Methane conversion over 800°C-calcined (□) 7YZ, and 7YZ coated with 25 wt% of (▲) Al_2O_3, (△) TiO_2, (■) CeO_2 and (×) Mn_2O_3. Catalytic testing was performed with 1% CH_4 in air at a flow rate of 50 ml/min.
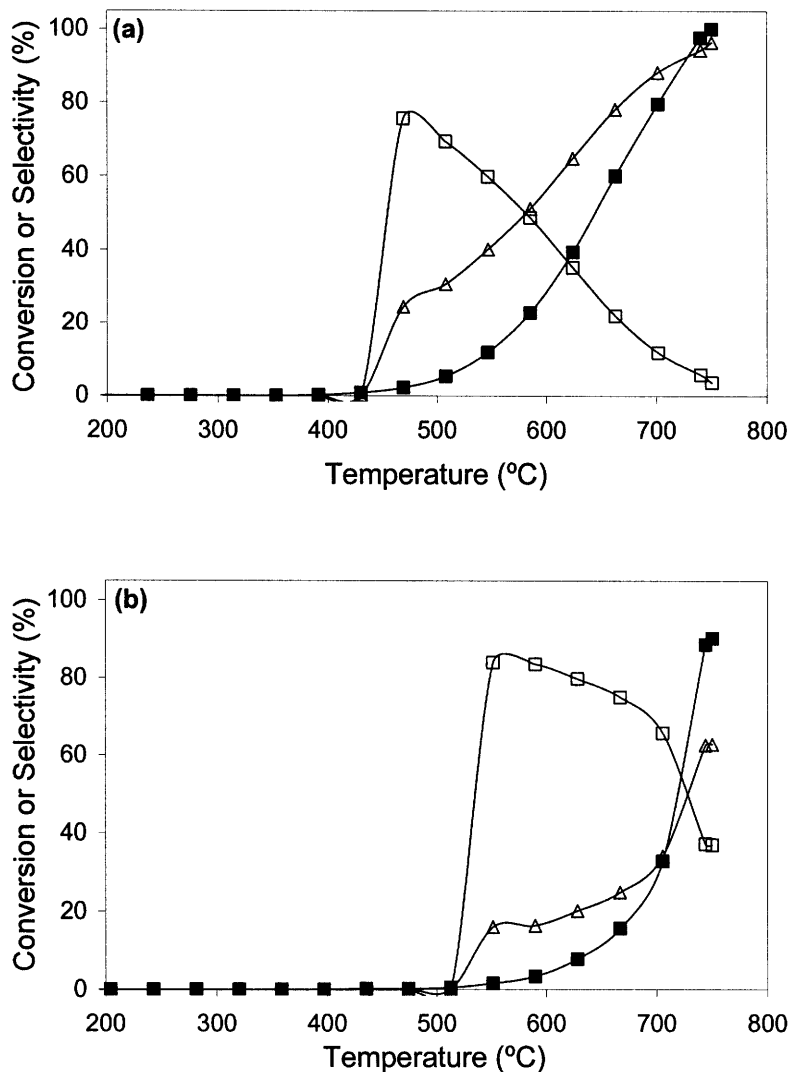
Figure 2.10 (■) CH₄ conversion, and selectivity for (Δ) CO₂ and (□) CO over 800°C-calcined 7YZ coated with 25 wt% of (a) Al₂O₃ and (b) TiO₂ in methane combustion. Catalytic testing was performed with 1% CH₄ in air at a flow rate of 50 ml/min.

For the doped samples, only the 25 wt% Mn₂O₃-doped 7YZ out-performed the undoped 7YZ (Figure 2.11). The doped 7YZ samples demonstrated different catalytic properties from their coated 7YZ counterparts. These studies illustrated that the catalytic performance was dependent on both the composition and the dispersion of the secondary component. Like their coated counterparts, the 7YZ samples doped with 25 wt% of Al₂O₃ and

TiO_2 generated undesired CO by-product due to incomplete methane combustion (Figure 2.12).

The low selectivity of 7YZ coated or doped with Al_2O_3 and TiO_2 prevented these catalysts from being effectively employed in methane combustion. Nakagawa *et al.* have also shown that TiO_2 and Al_2O_3 supports led to CO by-products in partial oxidation of methane.[22] Further studies were focused on 7YZ coated or doped with Mn_2O_3 and CeO_2, given the superior activity and selectivity of these systems.
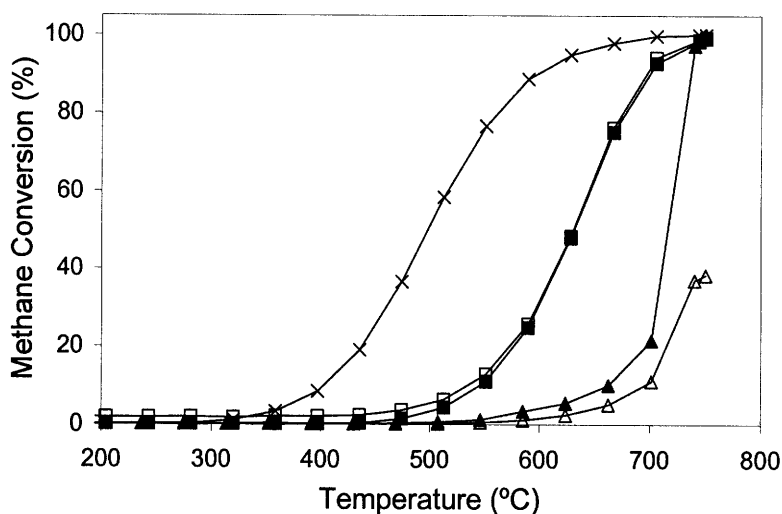
Figure 2.11 Methane conversion over 800°C-calcined (□) 7YZ, and 7YZ doped with 25 wt% of (▲) Al_2O_3, (△) TiO_2, (■) CeO_2 and (×) Mn_2O_3. Catalytic testing was performed with 1% CH_4 in air at a flow rate of 50 ml/min.
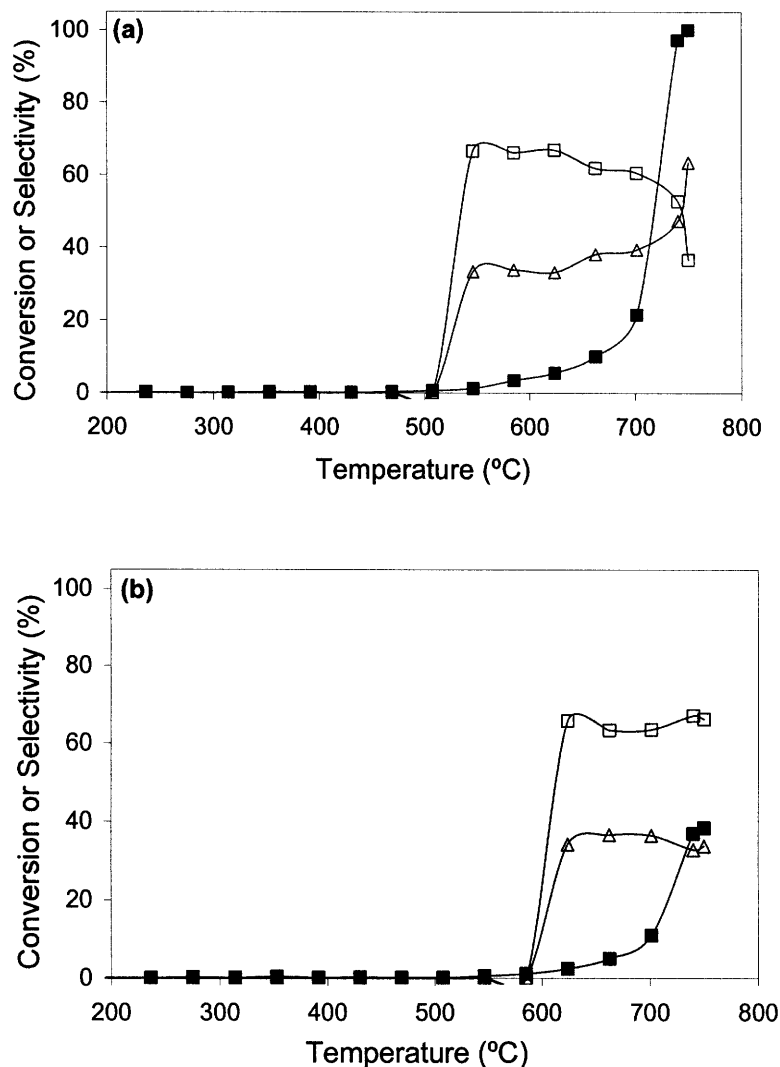
Figure 2.12 (■) CH₄ conversion, and selectivity for (Δ) CO₂ and (□) CO over 800°C-calcined 7YZ doped with 25 wt% of (a) Al₂O₃ and (b) TiO₂ in methane combustion. Catalytic testing was performed with 1% CH₄ in air at a flow rate of 50 ml/min.

2.3.3 Mn₂O₃-Coated and Doped 7YZ

2.3.3.1 Catalytic Activity

The full conversion of 800°C-calcined 25 wt% Mn₂O₃-coated or doped 7YZ was achieved by 700°C (Figures 2.9 and 2.11). Thus, 7YZ samples coated or doped with Mn₂O₃ could be calcined at 700°C for 2 h to take advantage of the higher surface area retained at this lower calcination temperature. Figure 2.13 illustrates the catalytic activities of 7YZ coated with different Mn₂O₃ loadings. The catalytic performance of 7YZ was enhanced with

increasing Mn_2O_3 coating. The 25 wt% Mn_2O_3-coated 7YZ gave the highest activity, with a light-off temperature of 375°C (corresponding to 10% methane conversion); full conversion of methane was achieved by 650°C. This system should not be calcined at a temperature below 700°C, as full conversion then would not be achieved below the calcination temperature (Figure 2.14).

Figure 2.15 shows that the catalytic performance of 7YZ was enhanced with increasing Mn_2O_3 doping. 25 wt% Mn_2O_3-doped 7YZ provided the highest catalytic activity, with a low light-off temperature of 358°C. Full conversion of methane was achieved by 650°C over 10, 15, 20 and 25 wt% Mn_2O_3-doped 7YZ.
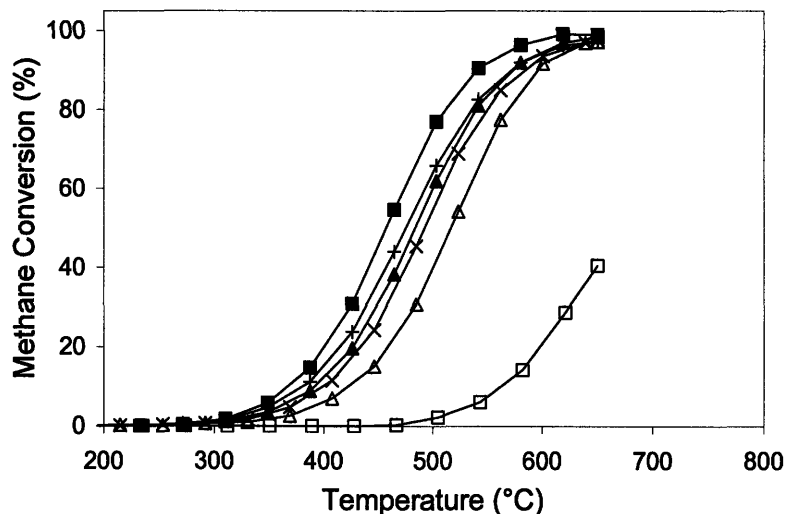
Figure 2.13 Methane conversion over 700°C-calcined 7YZ coated with (□) 0, (Δ) 5 (×) 10, (▲) 15, (+) 20 and (■) 25 wt% of Mn_2O_3. Catalytic testing was performed with 1% CH_4 in air at a flow rate of 50 ml/min.
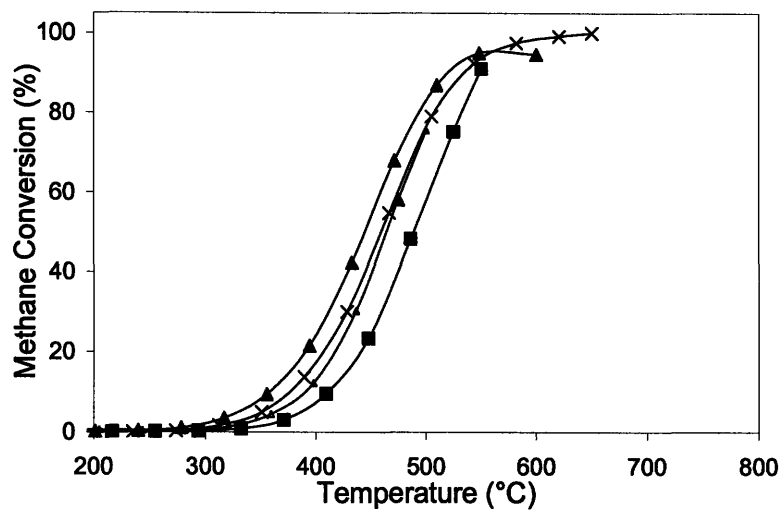
Figure 2.14 Methane conversion over 25 wt% Mn₂O₃-coated 7YZ calcined to (Δ) 550°C, (■) 600°C, (▲) 650°C, and (×) 700°C in air for 2 h. Catalytic testing was performed with 1% CH₄ in air at a flow rate of 50 ml/min to a maximum temperature that was 50°C below the calcination temperature.
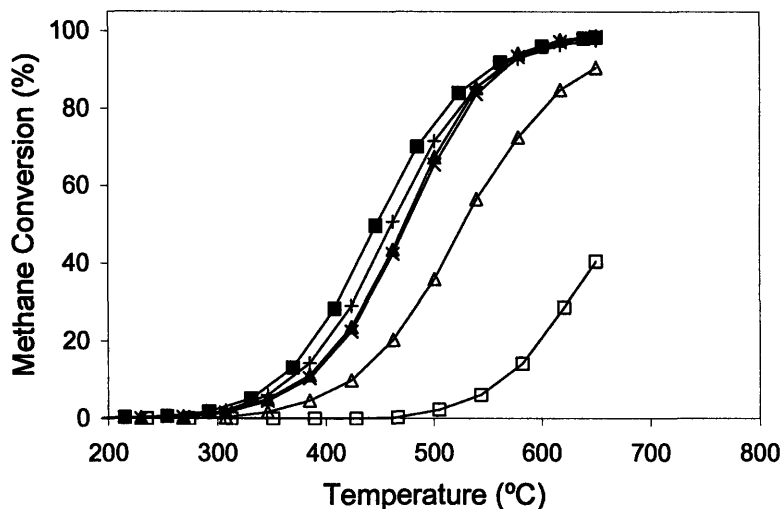
Figure 2.15 Methane conversion over 700°C-calcined 7YZ doped with (□) 0, (Δ) 5, (×) 10, (▲) 15, (+) 20 and (■) 25 wt% of Mn₂O₃. Catalytic testing was performed with 1% CH₄ in air at a flow rate of 50 ml/min.

Catalytic stability was examined over multiple reaction runs. The light-off temperatures of Mn₂O₃-coated and doped 7YZ samples are shown in Tables 2.2 and 2.3, respectively. The variation in the light-off temperatures between different runs was negligible

and within experimental error for each sample. This agreed with the zirconia XRD grain size results in Tables 2.4 and 2.5, which showed negligible grain growth after 2 runs.

Tables 2.2 and 2.3 also illustrated the general trend of decreasing light-off temperature with increasing Mn_2O_3 loading for both the Mn_2O_3-coated and doped 7YZ systems. This corresponded well with the finer zirconia grain size obtained by Mn_2O_3-coated and doped 7YZ samples at increasing Mn_2O_3 loading (Tables 2.4 and 2.5). For a given Mn_2O_3 loading, a lower light-off temperature was achieved with the Mn_2O_3-doped 7YZ sample than with the Mn_2O_3-coated 7YZ sample, especially at high Mn_2O_3 loadings.

Table 2.2 Light-off temperature of 700°C-calcined 7YZ coated with the specified Mn_2O_3 loading. Catalytic testing was performed with 1% CH_4 in air at a flow rate of 50 ml/min.

Light-off Temperature (°C)	0 wt%	5 wt%	10 wt%	15 wt%	20 wt%	25 wt%
Run #1	556	422	400	393	388	375
Run #2	564	420	403	395	385	375
Run #3	554	420	400	390	380	370

Table 2.3 Light-off temperature of 700°C-calcined 7YZ doped with the specified Mn_2O_3 loading. Catalytic testing was performed with 1% CH_4 in air at a flow rate of 50 ml/min.

Light-off Temperature (°C)	0 wt%	5 wt%	10 wt%	15 wt%	20 wt%	25 wt%
Run #1	556	424	396	377	367	358
Run #2	564	422	395	375	372	360
Run #3	554	425	395	373	365	356

Table 2.4 Zirconia XRD grain size of 700°C-calcined 7YZ coated with the specified Mn_2O_3 loading before and after 2 catalytic runs. Catalytic testing was performed with 1% CH_4 in air at a flow rate of 50 ml/min.

Grain Sizes (nm)	5 wt%	10 wt%	15 wt%	20 wt%	25 wt%
Before Run #1	26.9	23.8	22.1	20.3	13.7
After Run #2	26.2	23.9	21.9	20.1	14.2

Table 2.5 Zirconia XRD grain size of 700°C-calcined 7YZ doped with the specified Mn_2O_3 loading before and after 2 catalytic runs. Catalytic testing was performed with 1% CH_4 in air at a flow rate of 50 ml/min.

Grain Sizes (nm)	5 wt%	10 wt%	15 wt%	20 wt%	25 wt%
Before Run #1	32.0	20.5	18.6	15.2	13.4
After Run #2	31.9	20.0	18.8	14.9	14.0

Further investigation showed that the entire catalytic activity profile of 700°C-calcined 25 wt% Mn_2O_3-coated 7YZ was reproducible over 3 runs (Figure 2.16(a)). In contrast, 700°C-calcined 25 wt% Mn_2O_3-doped 7YZ displayed some decay in activity at high conversions (Figure 2.16(b)). This effect was increased when the calcination temperature of 25 wt% Mn_2O_3-doped 7YZ was raised to 800°C (Figure 2.17). In this case, not only was the temperature required for 100% conversion increased after 3 runs, the light-off temperature was also raised by 25°C between the first run and the third run. This could be attributed to the zirconia grain growth in 800°C-calcined 25 wt% Mn_2O_3-doped 7YZ from 16.2 nm (before run #1) to 17.8 nm (after run #3). It has been reported that the high surface area and mesoporous structure observed in Mn-doped ZrO_2 solid solution at low calcination temperature would became unstable at a temperature above 750°C.[23] Thus, it would be important to avoid using Mn_2O_3-doped 7YZ at high reaction temperatures. Mn_2O_3-coated 7YZ would be preferred for reactions to 650°C.

41
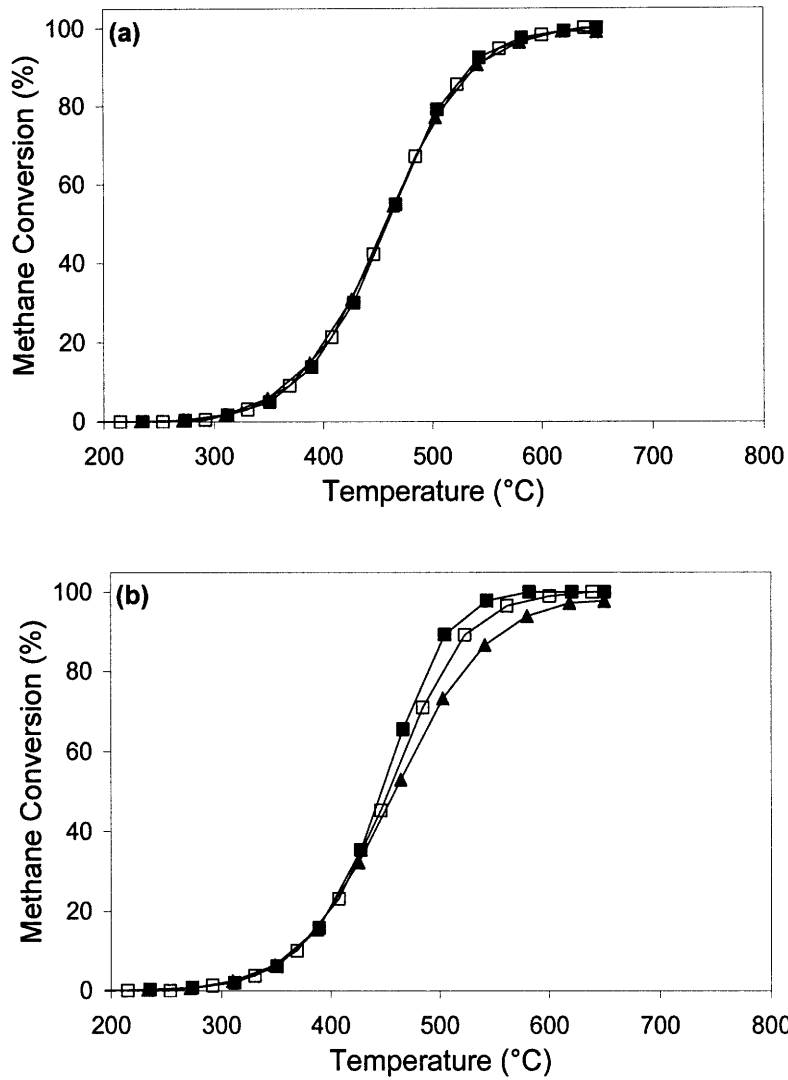
Figure 2.16 Methane conversion in runs (■) #1, (□) #2 and (▲) #3 over 700°C-calcined 7YZ (a) coated and (b) doped with 25 wt% of Mn₂O₃. Catalytic testing was performed with 1% CH₄ in air at a flow rate of 50 ml/min.
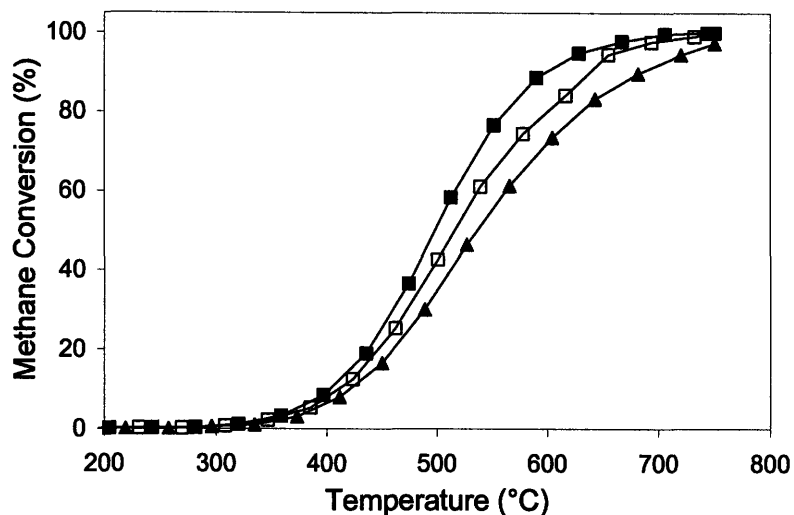
Figure 2.17 Methane conversion in runs (■) #1, (□) #2 and (▲) #3 over 800°C-calcined 25 wt% Mn₂O₃-doped 7YZ. Catalytic testing was performed with 1% CH₄ in air at a flow rate of 50 ml/min.

2.3.3.2 Materials Characterization

XRD patterns of 7YZ coated and doped with different Mn_2O_3 loadings are shown in Figure 2.18. Only 25 wt% Mn_2O_3-coated 7YZ showed a separate Mn_2O_3 phase besides the cubic zirconia phase. The cubic zirconia lattice parameter was shown to decrease with increasing Mn_2O_3 loading (Figure 2.19), indicating that increasing amount of manganese ions were introduced into the 7YZ lattice. This doping effect was relatively minor in the Mn_2O_3-coated 7YZ system. As expected, it was very significant for the Mn_2O_3-doped 7YZ system. However, it still deviated from the theoretical curve based on Kim's equation[24,25] at high Mn loadings (see Figure 2.19). This indicated that not all the Mn loaded in the heavily Mn_2O_3-doped samples was introduced into the 7YZ lattice, suggesting that some Mn_2O_3 was segregated to the surface of the 7YZ grains. ICP-AES confirmed that the actual Mn loadings in the samples were quite similar to that introduced during the synthesis (Table 2.6). Therefore, the lack of a separate Mn_2O_3 phase in the XRD pattern of most samples could be attributed to (i) the uniform dispersion of manganese as dopants in the 7YZ grains, and (ii) the presence of a highly dispersed amorphous Mn_2O_3 coating on the 7YZ grains. Both are present in the Mn_2O_3-coated and doped 7YZ samples, but in different relative amounts. The former

would be dominant in the Mn_2O_3-doped 7YZ system, while the latter would be dominant in the Mn_2O_3-coated 7YZ. The co-existence of Mn_2O_3 and Mn-Zr-O solid solution was also confirmed in Koh et al.'s study of co-precipitated Mn/Zr system.[26]

Figure 2.18 XRD patterns of 7YZ (i) coated and (ii) doped with (a) 0, (b) 5, (c) 10, (d) 15, (e) 20 and (f) 25 wt% of Mn_2O_3, after calcination at 700°C in air for 2 h. Peaks of Mn_2O_3 were denoted by #.

Figure 2.19 Lattice parameters of (▲) Mn₂O₃-coated and (■) Mn-doped 7YZ, after calcination at 700°C in air for 2 h. The dotted line represented the theoretical value calculated based on Kim's equation.[24]

Table 2.6 Theoretical and actual Mn loadings in Mn₂O₃-coated and doped 7YZ, after calcination at 700°C in air for 2 h.

Samples	Nominal Mn₂O₃ Loading (wt%)	Targeted Mn Loading (wt%)	Actual Mn Loading* (wt%)
Mn₂O₃-Coated 7YZ	5	3.9	3.9
	10	7.8	7.2
	15	11.5	10.8
	20	15.3	14.8
	25	19.1	20.6
Mn₂O₃-Doped 7YZ	5	3.9	4.1
	10	7.8	8.2
	15	11.5	12.1
	20	15.3	16.3
	25	19.1	20.3

*Determined by ICP-AES.

25 wt% Mn₂O₃-doped 7YZ remained a single phase after calcination at 700°C (Figure 2.18(ii)(f)) and 800°C (Figure 2.4(e)) for 2 h. However, Mn₃O₄ was segregated into a separate phase upon calcination at 1000°C (Figure 2.20), in agreement with the observation of Kim and Choi.[12] Thus, the single phase present in 25 wt% Mn₂O₃-doped 7YZ was only metastable.

45
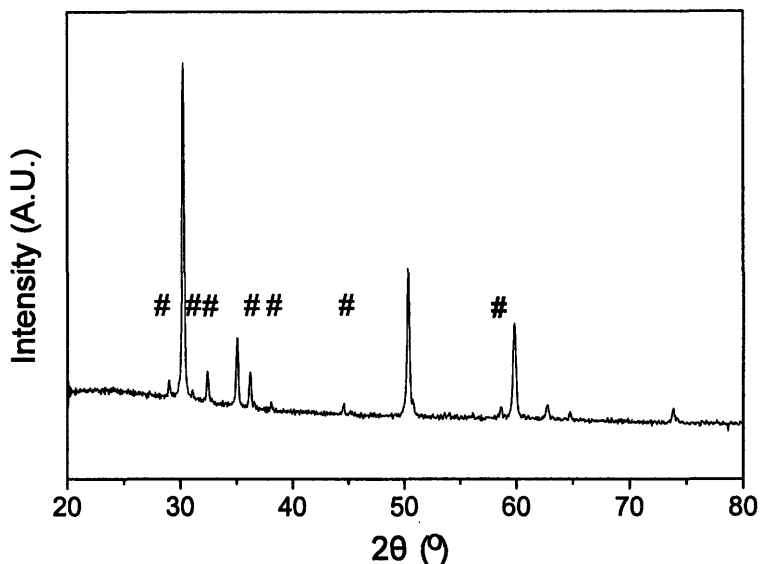
Figure 2.20 XRD of 25 wt% Mn-doped 7YZ after calcination at 1000°C in air for 2 h. Peaks of Mn_3O_4 were denoted by #.

The TEM images of 7YZ, and 25 wt% Mn_2O_3-coated and doped 7YZ are illustrated in Figures 2.21–2.23. All three powder samples were heavily agglomerated. For 25 wt% Mn_2O_3-coated 7YZ, no visible change was noted before and after 2 runs of methane combustion (Figure 2.22). Under higher TEM resolution, grains with two different sizes were distinguished in 25 wt% Mn_2O_3-coated 7YZ sample (Figure 2.21(b)). The smaller grains (10–20 nm) and larger grains (30–40 nm) in TEM corresponded to 7YZ and Mn_2O_3, respectively, as confirmed by lattice calculations (Figures 2.21(i–iii)). These were consistent with the average grain sizes determined by XRD for 7YZ (15.3 nm) and Mn_2O_3 (37.9 nm). A high dispersion of 7YZ and Mn_2O_3 grains were obtained on the nanometer scale, as further confirmed by STEM and elemental mapping (Figure 2.24). Such intimate mixing of two phases could not be achieved by mechanical mixing, and provided for a high level synergism between 7YZ and Mn_2O_3 in the catalytic combustion of methane. Consequently, the light-off temperature of 25 wt% Mn_2O_3-coated 7YZ nanocomposite (375°C) was lower than that of nanocrystalline Mn_2O_3 (395°C) and nanocrystalline 7YZ (558°C) (Figure 2.25).

The particles in 25 wt% Mn_2O_3-doped 7YZ were quite uniform in size, as they corresponded to 7YZ grains (Figure 2.23). No separate Mn_2O_3 phase was detected by TEM or

XRD when calcined at 700°C. There was no distinct difference in the TEM images of the sample before and after two runs of methane combustion, despite the minor decay at high conversions in the activity profiles (Figure 2.16(b)).
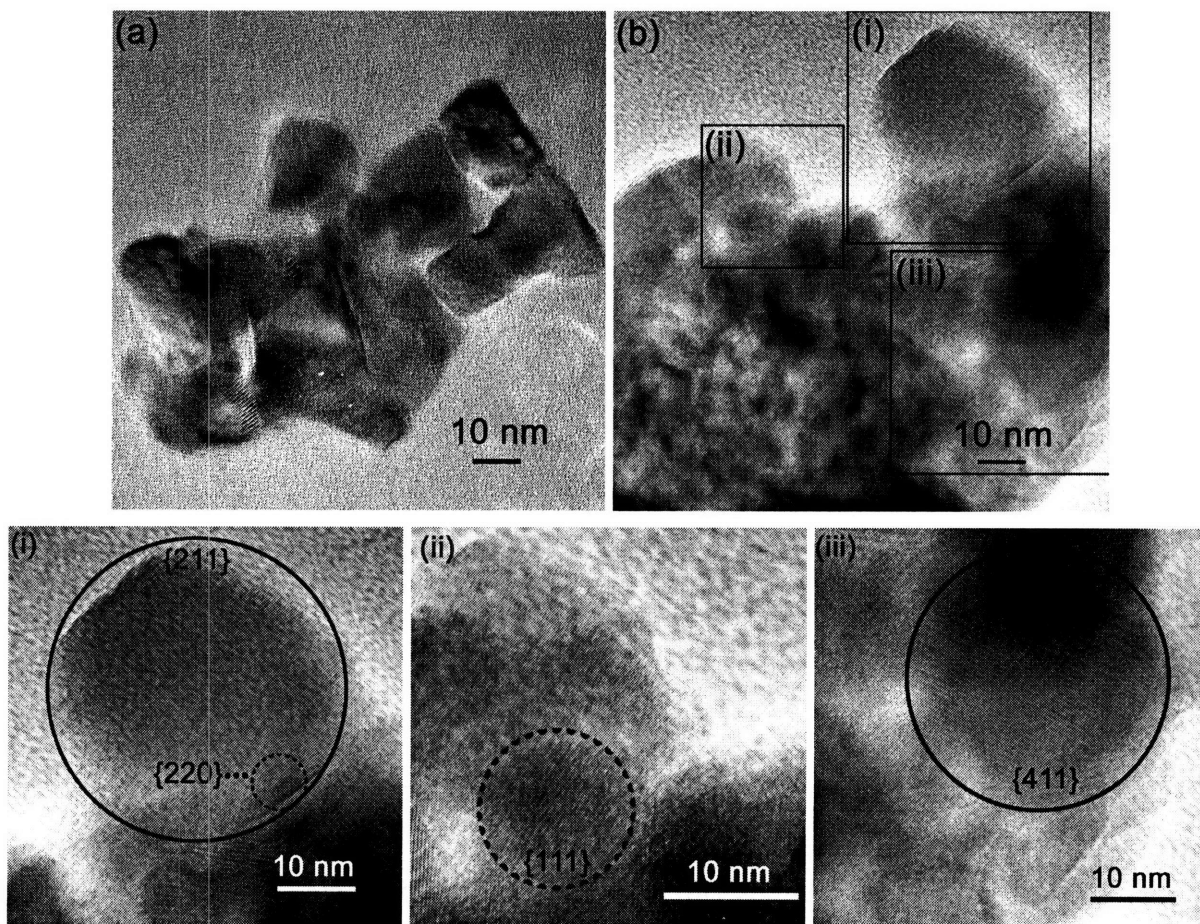
Figure 2.21   TEM micrographs of 700°C-calcined powders of (a) 7YZ, and (b) 25 wt% Mn_2O_3-coated 7YZ. Mn_2O_3 and 7YZ grains were identified by lattice fringes calculations, and denoted by solid circles and dotted circles, respectively, in (i), (ii) and (iii).
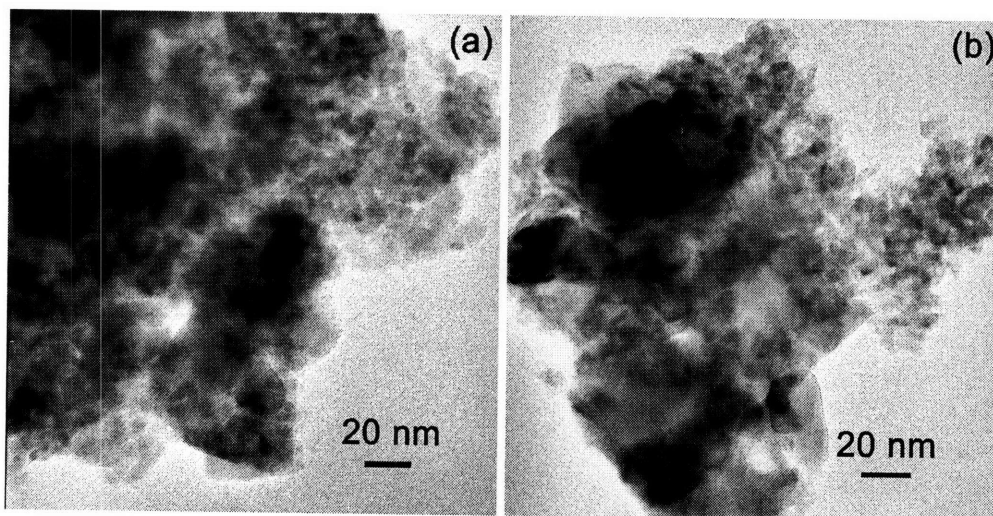
Figure 2.22 TEM micrographs of 700°C-calcined 25 wt% Mn_2O_3-coated 7YZ (b) before and (c) after 2 runs of methane combustion performed with 1% CH_4 in air at a flow rate of 50 ml/min.
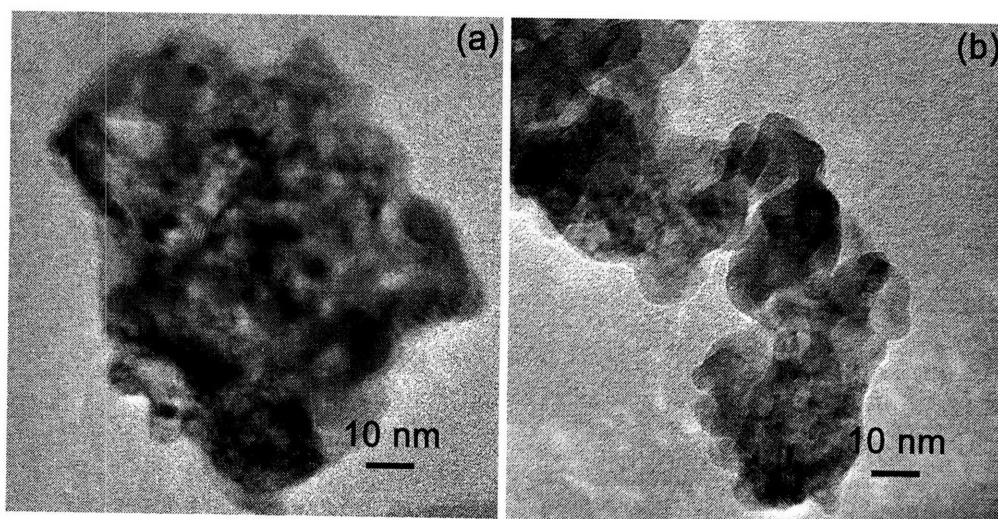
Figure 2.23 TEM micrographs of 700°C-calcined 25 wt% Mn_2O_3-doped 7YZ (a) before and (b) after 2 runs of methane combustion performed with 1% CH_4 in air at a flow rate of 50 ml/min.
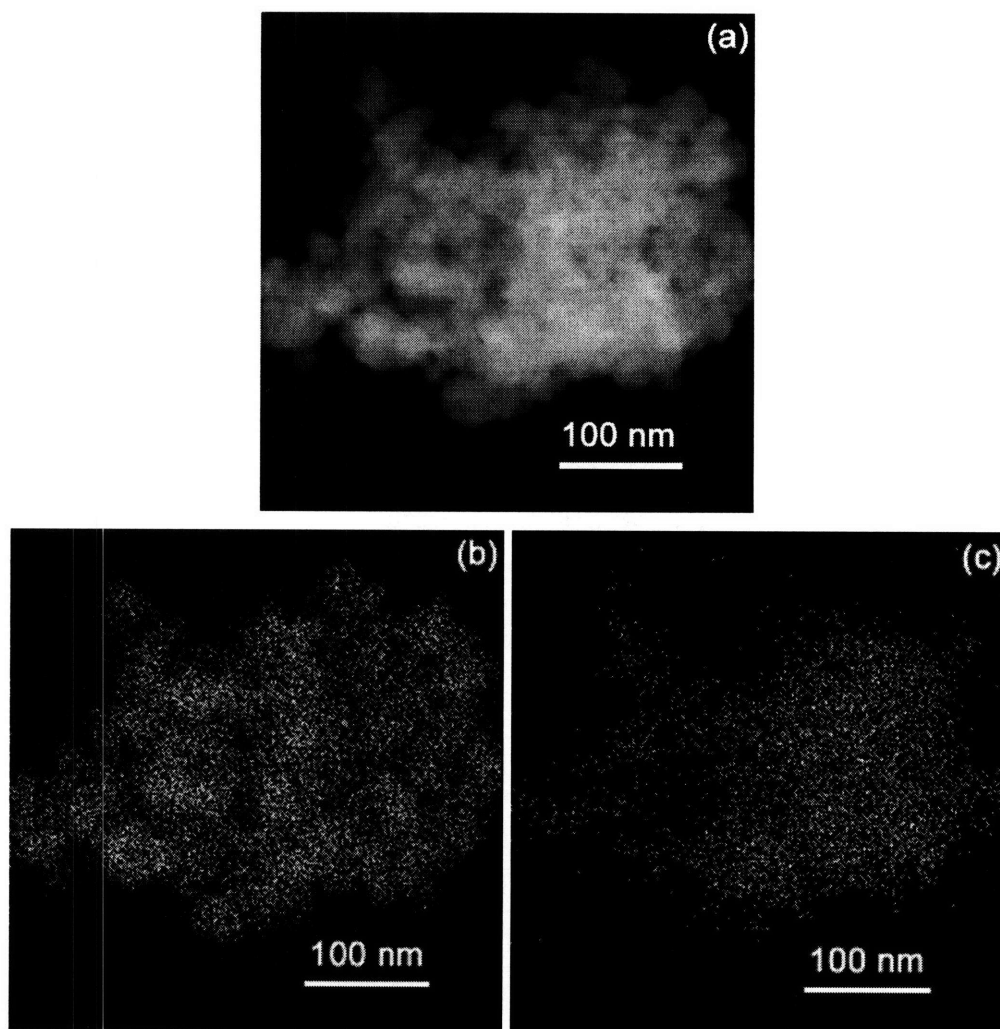
Figure 2.24 (a) STEM micrograph, and (b) Mn and (c) Zr elemental maps of 700°C-calcined 25 wt% Mn_2O_3-coated 7YZ.
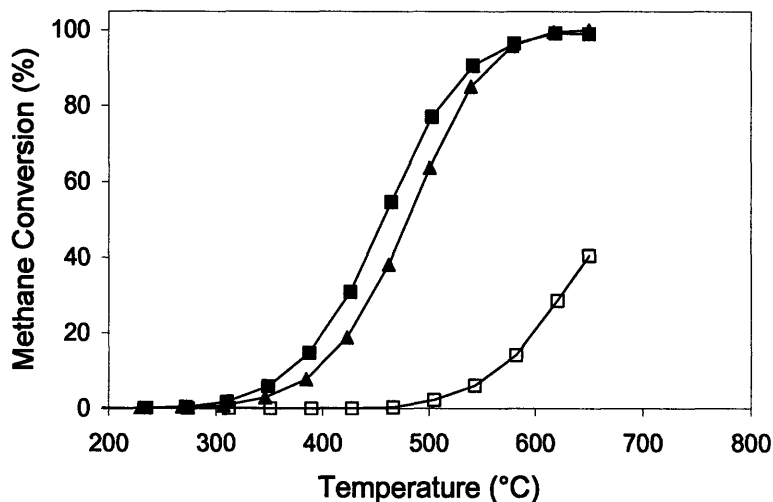
Figure 2.25 Methane conversion over 700°C-calcined (□) 7YZ, (▲) Mn₂O₃, and (■) 25 wt% Mn₂O₃-coated 7YZ. Catalytic testing was performed with 1% CH₄ in air at a flow rate of 50 ml/min.

2.3.4 CeO₂-Coated and Doped 7YZ

2.3.4.1 Catalytic Activity

Catalytic activities of CeO_2-coated and doped 7YZ are presented in Figure 2.26 and Figure 2.27, respectively. CeO_2-coated 7YZ samples showed significantly higher catalytic activities than the CeO_2-doped 7YZ samples at a given CeO_2 loading. 20 wt% CeO_2-coated 7YZ demonstrated the highest catalytic activity among the CeO_2-coated and doped 7YZ samples. It has a light-off temperature of 510°C, providing for full methane conversion at 750°C.

Unlike the CeO_2-coated 7YZ samples, the CeO_2-doped 7YZ samples actually showed lower catalytic activities than the unmodified 7YZ. Unlike the manganese dopants, cerium dopants have the same valence as the zirconium ions. Thus, they would not introduce any oxygen vacancies into zirconia, which might have improved the catalytic activity in the case of Mn_2O_3-doped 7YZ. In addition, cerium dopants could be readily introduced into the zirconia lattice, thus a highly dispersed amorphous CeO_2 coating might be absent on the 7YZ grains. Such a highly dispersed CeO_2 coating might be essential towards increasing the 7YZ activity in CeO_2-modified 7YZ samples.

50
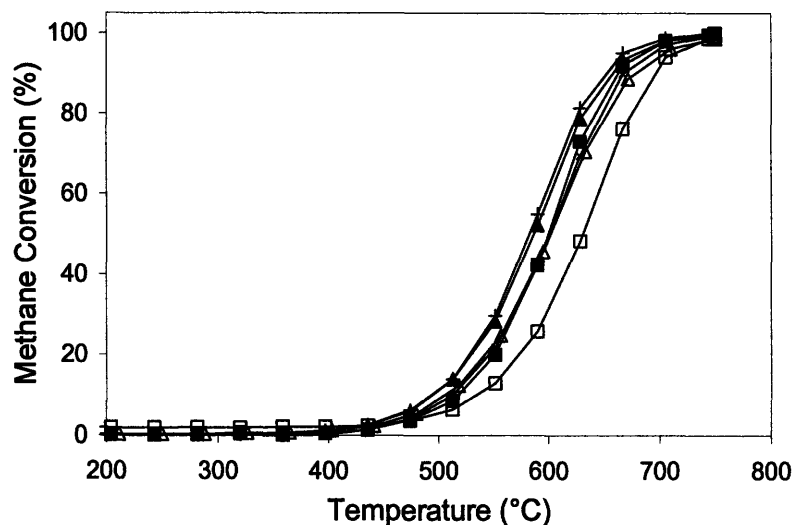
Figure 2.26 Methane conversion over 800°C-calcined 7YZ coated with (□) 0, (Δ) 5 (×) 10, (▲) 15, (+) 20 and (■) 25 wt% of CeO_2. Catalytic testing was performed with 1% CH_4 in air at a flow rate of 50 ml/min.
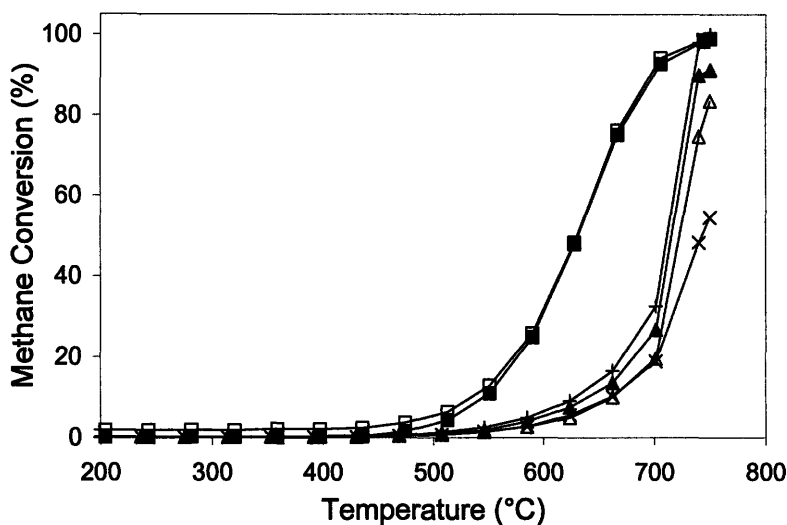
Figure 2.27 Methane conversion over 800°C-calcined 7YZ doped with (□) 0, (Δ) 5 (×) 10, (▲) 15, (+) 20 and (■) 25 wt% of CeO_2. Catalytic testing was performed with 1% CH_4 in air at a flow rate of 50 ml/min.

The light-off temperatures of 800°C-calcined CeO_2-coated 7YZ and 25 wt% CeO_2-doped 7YZ over multiple runs were summarized in Table 2.7. Like 7YZ, they showed negligible changes in light-off temperatures. 20 wt% CeO_2-coated 7YZ showed the lowest

light-off temperature. Its catalytic activity profile did not vary substantially over three consecutive runs (Figure 2.28). However, this best 800°C-calcined CeO_2-modified 7YZ catalyst could not compete with any of the 700°C-calcined Mn_2O_3-coated and doped 7YZ samples in catalytic activity (Tables 2.2 and 2.3), even though it significantly enhanced the catalytic activity of 7YZ.

Table 2.7   Light-off temperature of 800°C-calcined 7YZ coated[†] and doped* with the specified CeO_2 loading. Catalytic testing was performed with 1% CH_4 in air at a flow rate of 50 ml/min.

Light-off Temperature (°C)	CeO_2 Loading (wt%)						
	0[†]	5[†]	10[†]	15[†]	20[†]	25[†]	25*
Run # 1	540	510	505	500	485	510	540
Run # 2	540	510	505	500	495	510	545
Run # 3	540	510	510	495	485	515	540
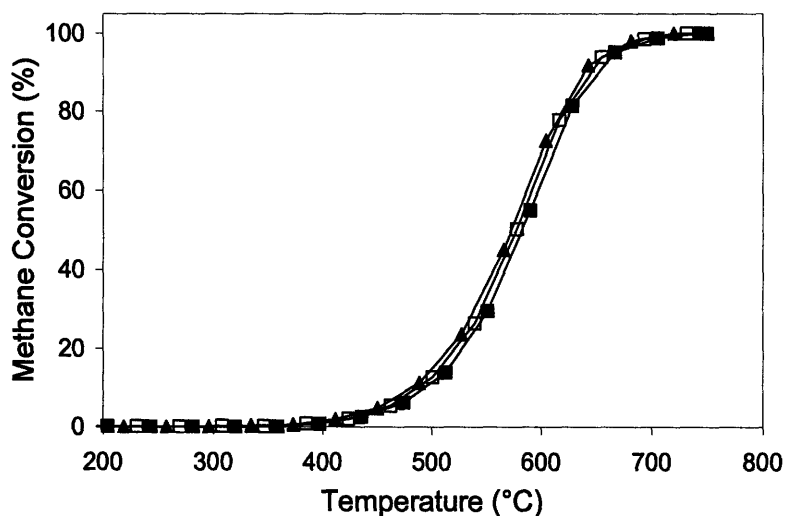
Figure 2.28   Methane conversion in runs (■) #1, (□) #2 and (▲) #3 over 800°C-calcined 20 wt% CeO_2-coated 7YZ. Catalytic testing was performed with 1% CH_4 in air at a flow rate of 50 ml/min.

2.3.4.2 Materials Characterization

Figure 2.29 illustrates the XRD patterns of 800°C-calcined CeO_2-coated and doped 7YZ samples. CeO_2 emerged as a separate phase when $\geq$ 10 wt% CeO_2 was coated onto 7YZ.

For the CeO_2-coated 7YZ system, negligible XRD peak shifts were noted, and the lattice parameter of cubic zirconia remained essentially unchanged for the range of CeO_2 loadings examined (Figure 2.30). This indicated that cerium was hardly substituted into the zirconia crystal structure by the coating route.

In contrast, at least 25 wt% of CeO_2 could be doped into 7YZ without forming a separate crystalline phase (Figure 2.29(ii)). With increasing doping of 7YZ with CeO_2, XRD peaks were shifted to the smaller diffraction angles. Figure 2.30 illustrates a steady increase in the lattice parameter of cubic zirconia with increasing CeO_2 loading. This confirmed the successful substitution of cerium ions into the zirconia crystal structure, expanding the latter due to the larger ionic radius of Ce^{4+} compared to Zr^{4+}.
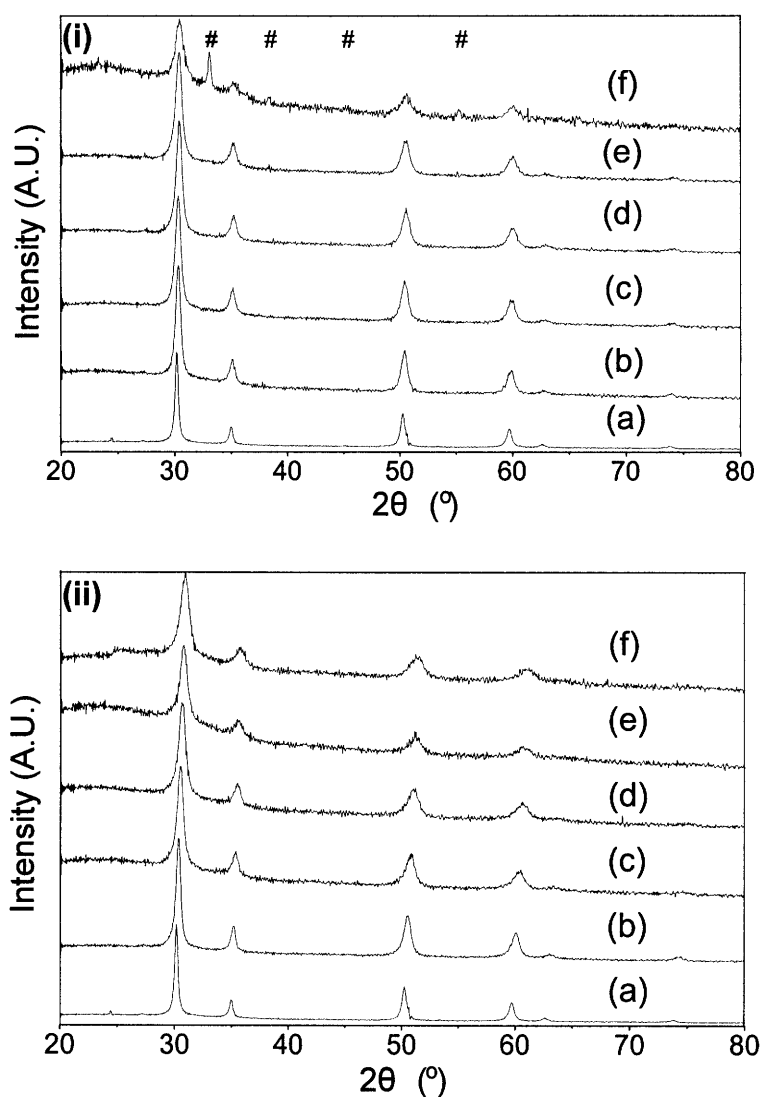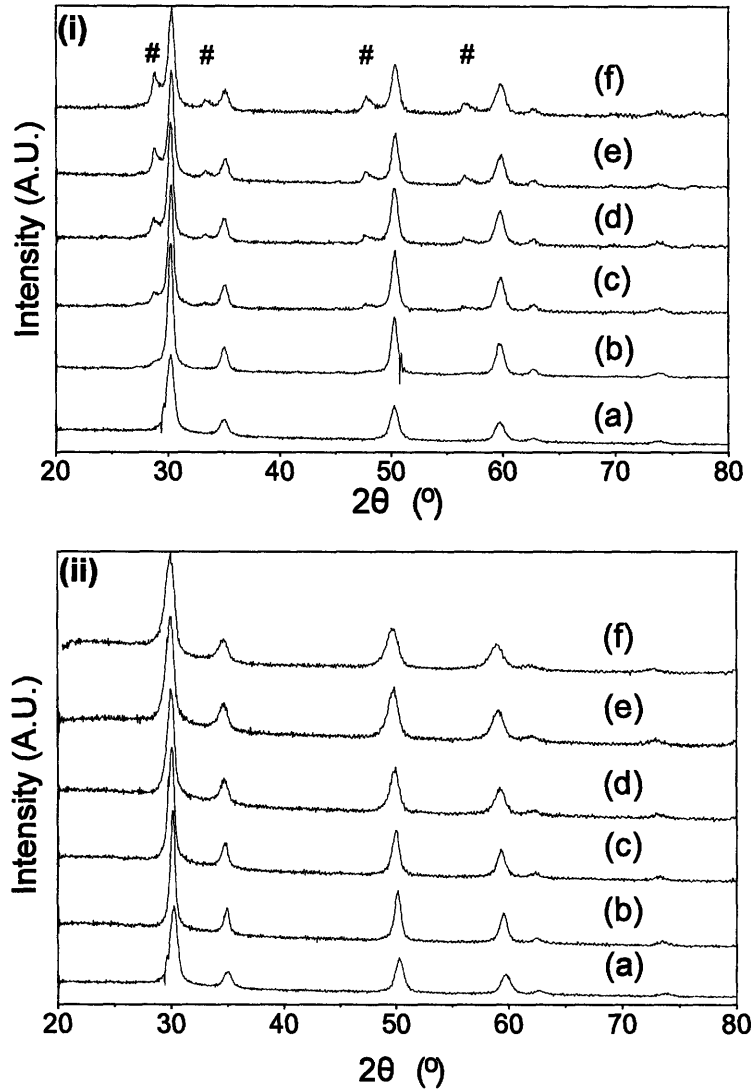
Figure 2.29 XRD patterns of 7YZ (i) coated and (ii) doped with (a) 0, (b) 5, (c) 10, (d) 15, (e) 20 and (f) 25 wt% of CeO_2, after calcination at 800°C in air for 2 h. Peaks of CeO_2 were denoted by #.
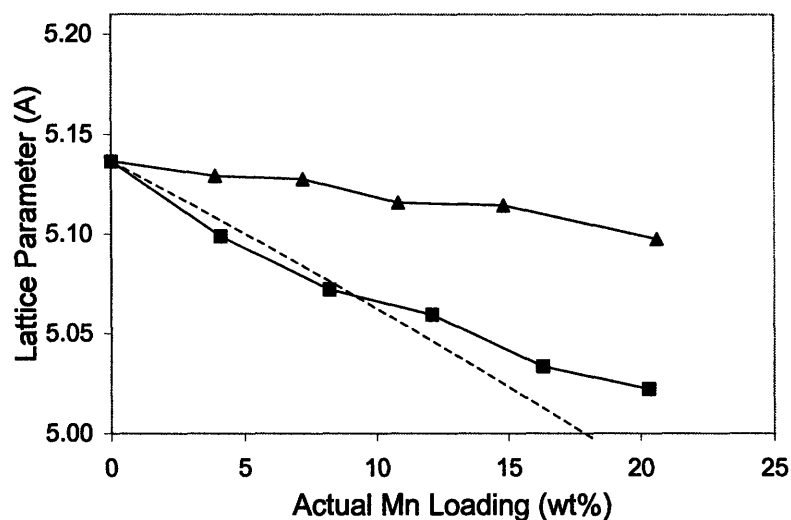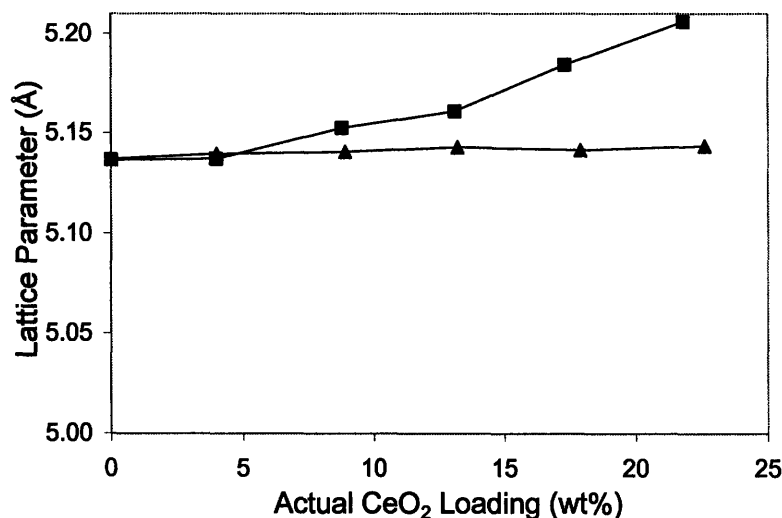
Figure 2.30 Lattice parameters of (▲) CeO_2-coated and (■) CeO_2-doped 7YZ, after calcination at 800°C in air for 2 h.

Table 2.8 Theoretical and actual Ce loadings in CeO_2-coated and doped 7YZ, after calcination at 800°C in air for 2 h.

Samples	Nominal CeO_2 Loading (wt%)	Targeted Ce Loading (wt%)	Actual Ce Loading* (wt%)
CeO₂-Coated 7YZ	5	4.1	4.0
	10	8.3	8.9
	15	12.4	13.2
	20	16.5	17.9
	25	20.6	22.6
CeO₂-Doped 7YZ	5	4.1	4.0
	10	8.3	8.8
	15	12.4	13.1
	20	16.5	17.3
	25	20.6	21.8

*Determined by ICP-AES.

The best CeO_2-modified 7YZ, 20 wt% CeO_2-coated 7YZ, was characterized by TEM, which showed negligible changes in the microstructure of the catalyst before and after two cycles of methane combustion (Figure 2.31). It has a similar particle morphology and a slightly finer grain size than unmodified 7YZ. The ceria and zirconia XRD grain sizes were 20.4 nm and 17.4 nm, respectively (Figure 2.29(i)(e)). The ceria and zirconia grains showed

similar particle size and morphology by TEM (Figure 2.31). STEM images confirmed that the two phases were highly dispersed and in close contact (Figure 2.32), providing a synergistic effect in catalytic performance.
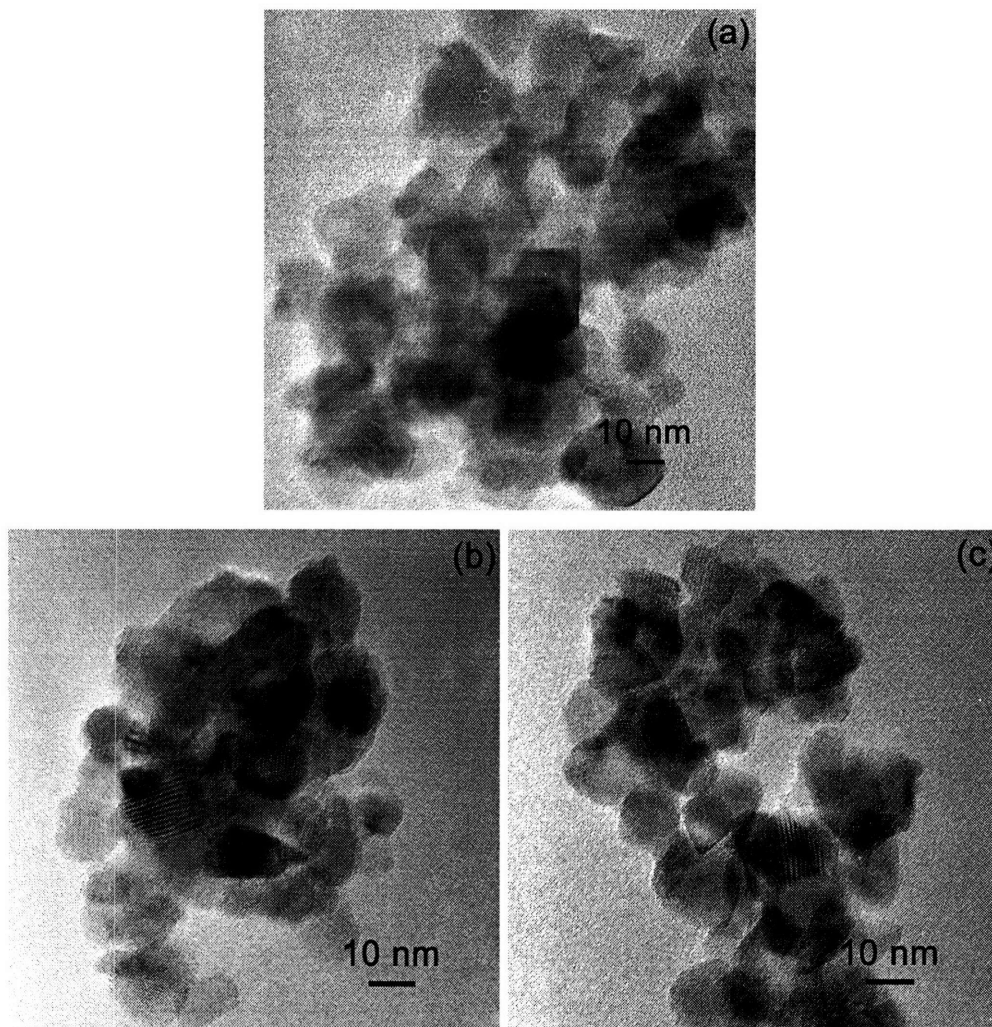
Figure 2.31 TEM micrographs of 800°C-calcined (a) 7YZ, and 20 wt% CeO_2-coated 7YZ (b) before and (c) after 2 runs of methane combustion performed with 1% CH_4 in air at a flow rate of 50 ml/min.
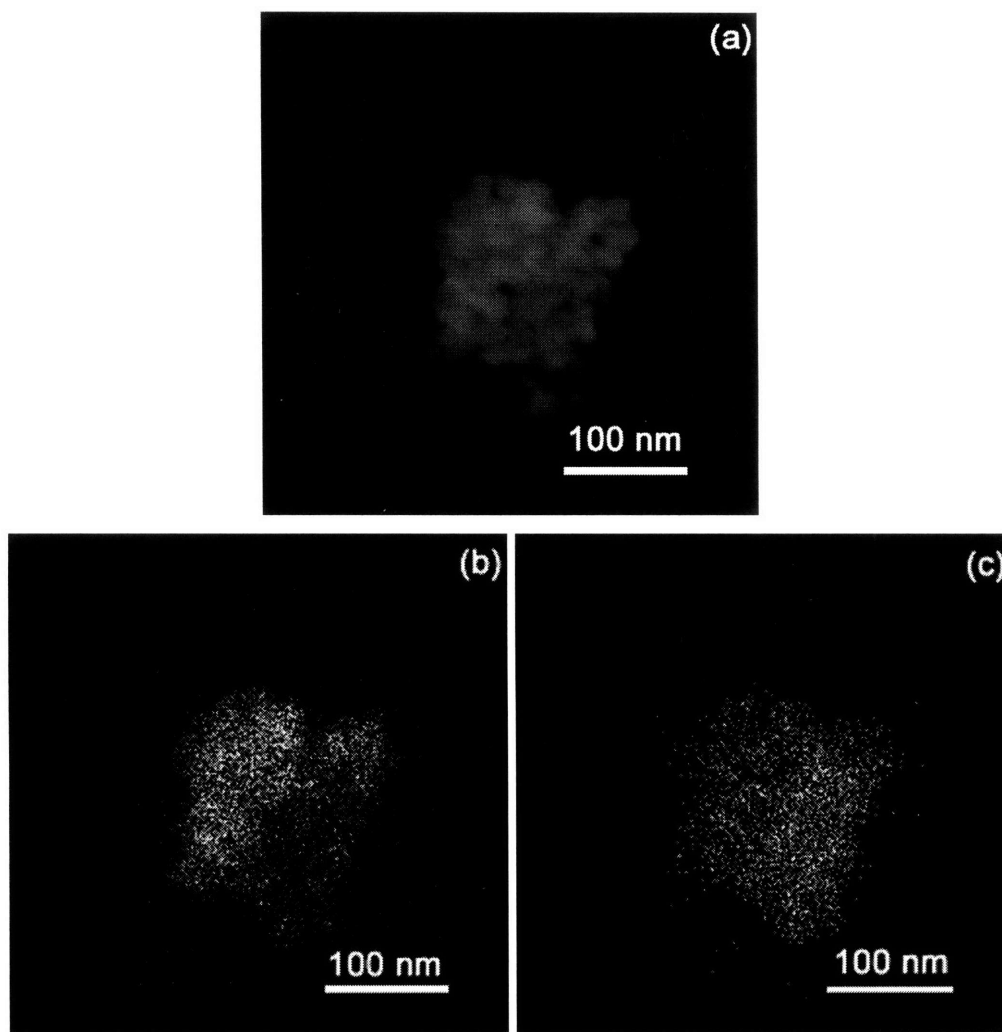
Figure 2.32 (a) STEM micrograph, and (b) Ce and (c) Zr elemental maps of 800°C-calcined 20 wt% CeO_2-coated 7YZ.

2.3.5 Kinetics and Mechanism of Methane Combustion

The catalysts with the highest activities, 25 wt% Mn_2O_3-coated and doped 7YZ, were subjected to further mechanistic studies.

2.3.5.1 Temperature-Programmed Reduction with Methane and Desorption of Oxygen

The catalytic oxidation of CH_4 to CO_2 would begin with the abstraction of hydrogen from methane, resulting in the formation of activated methane species. At temperatures above 700°C, these activated species would desorb from the catalyst surface to produce gas-phase methyl radicals. The methyl radicals would react with gas-phase oxygen or activated oxygen species on the catalyst surface, leading to the formation of CO_2. Since methane is a very

stable molecule, hydrogen abstraction from methane is typically considered to be the rate-limiting step. The activity and selectivity of methane oxidation depend on the nature and amount of oxygen species on the catalyst surface.[27-31]

At lower temperatures, the activated methane species might not desorb into the gas phase, but may further react with adsorbed oxygen species leading to carbonate formation. Subsequent desorption of carbonate and hydroxyl species from the catalyst surface would regenerate the active site. Therefore, the catalytic mechanism of methane oxidation could be divided into three steps (see Figure 2.33): (1) hydrogen abstraction from methane to form activated methane species, (2) oxidation of adsorbed methane species to surface carbonate, and (3) regeneration of active sites by carbonate and hydroxyl desorption, and oxygen adsorption.[18] To study the individual steps involved in this mechanism, TPR of 25 wt% Mn_2O_3-coated and doped 7YZ was performed with methane. On heating the catalyst in the presence of methane, the temperature at which methane was activated to form an adsorbed methoxy species could be determined, which might be related to the intrinsic activity for hydrogen abstraction from methane. The desorption temperatures of CO_2 would indicate the stability of surface carbonate species, and/or the kinetics of transformation of adsorbed methoxy species to surface carbonate species.

Figure 2.34 shows the TPR curves for 700°C-calcined 25 wt% Mn_2O_3-coated 7YZ. Methane activation was found to occur at ~ 300°C, with the simultaneous formation of CO_2. This suggested that conversion of adsorbed methoxy species to surface carbonate, and its subsequent desorption as CO_2 were fast reaction steps.

The TPR curves for 700°C-calcined 25 wt% Mn_2O_3-doped 7YZ are illustrated in Figure 2.35. Activation of methane was found to occur at a lower temperature of ~ 230°C, indicating that the greater substitution of Mn^{3+} for Zr^{4+} in the doped sample increased the intrinsic activity for hydrogen abstraction from methane. CO_2 formation was observed along with methane activation, suggesting that conversion of adsorbed methoxy species to surface carbonate, and its subsequent desorption as CO_2 were fast reaction steps.

$$CH_4 + 2O^* \longrightarrow CH_3O^* + OH^*$$

$$CH_3O^* + O^* \dashrightarrow CO_3^* + OH^* \dashrightarrow CO_2 + H_2O + O^*$$
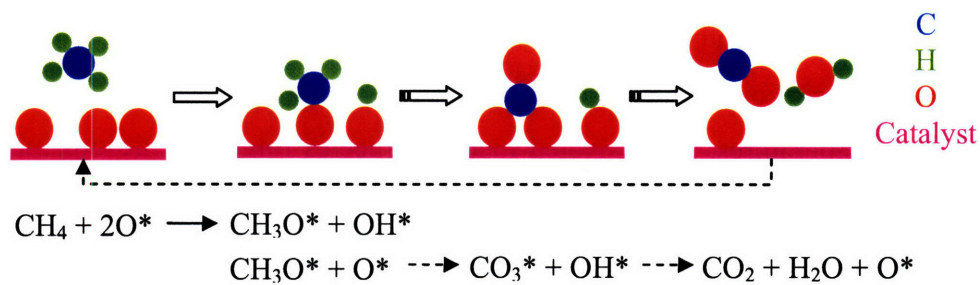
Figure 2.33 Graphical representation of catalyst activation in methane combustion.
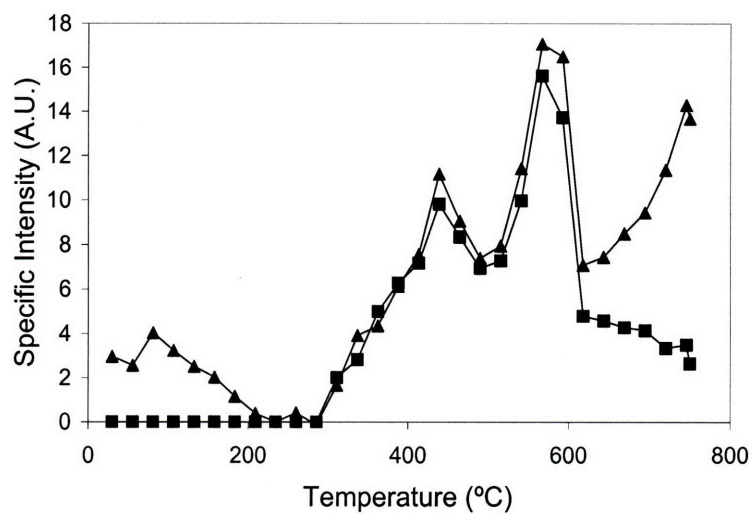
Figure 2.34 TPR curves for 700°C-calcined 25 wt% Mn_2O_3-coated 7YZ, showing (▲) CH_4 detected in outlet stream, and (■) CO_2 formation. TPR was performed under 0.5% CH_4 in He at a flow rate of 20 ml/min.
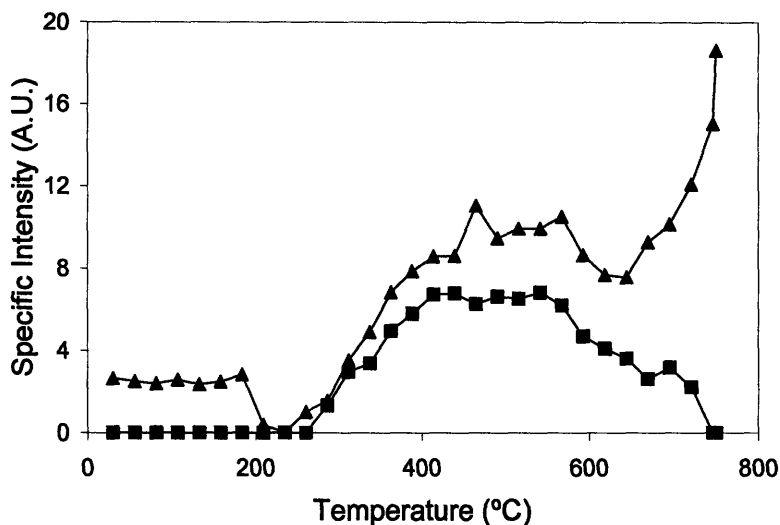
Figure 2.35 TPR curves for 700°C-calcined 25 wt% Mn_2O_3-doped 7YZ, showing (▲) CH_4 detected in outlet stream, and (■) CO_2 formation. TPR was performed under 0.5% CH_4 in He at a flow rate of 20 ml/min.

Figure 2.36 shows the TGA profiles of 7YZ, and 25 wt% Mn_2O_3-coated and doped 7YZ in the presence of CH_4. 7YZ showed very gradual weight loss. This could be attributed to the difficulty in significantly reducing 7YZ below 550°C. Figure 2.37 also illustrates that negligible oxygen desorption occurred below ~ 510°C. The observations correlated well with the high light-off temperature (558°C) for 7YZ. In contrast, Mn_2O_3 exhibited oxygen desorption at a much lower temperature (~ 250°C) (Figure 2.37), suggesting its ability to oxidize methane at a relatively low temperature, as demonstrated by Stobbe *et al.* and Dobber *et al.*[32,33] However, the amount of oxygen desorbed was small due to the low surface area of Mn_2O_3 (Figure 2.38(b)). This could be attributed to the large grain size of Mn_2O_3, which was greater than 100 nm upon calcination at 550°C, and was thus not shown in Figure 2.38(a).

Compared to 7YZ and Mn_2O_3, Mn_2O_3-modified 7YZ samples demonstrated much greater weight losses in methane (Figure 2.36) and much more oxygen desorption (Figure 2.37). This could be attributed to the superior thermal stability of the Mn_2O_3-modified 7YZ samples, especially 25 wt% Mn_2O_3-doped 7YZ, which exhibited a much higher surface area than 25 wt% Mn_2O_3-coated 7YZ, 7YZ and Mn_2O_3 after calcination at 700°C.

25 wt% Mn_2O_3-coated 7YZ showed a two-step weight loss in methane, and two major oxygen desorption peaks. The low-temperature peak centered at ~ 300°C might be attributed

to the desorption of weakly adsorbed oxygen species (such as O_2^-) from the surface of the Mn$_2$O$_3$ coatings on 7YZ. Such species did not participate in the hydrogen abstraction from methane, which was only initiated at $\sim$ 300°C (Figure 2.34). The second oxygen desorption peak emerged above 380°C. It could be attributed to the desorption of active chemisorbed oxygen species associated with the substitution of Mn^{3+} for Zr^{4+} in the zirconia lattice. This TPD peak temperature corresponded well to the light-off temperature of 375°C.

25 wt% Mn$_2$O$_3$-doped 7YZ presented even greater weight loss in methane than 25 wt% Mn$_2$O$_3$-coated 7YZ (Figure 2.36). Its weight loss occurred in four steps, and could be attributed to the ease of reducing zirconia substituted with a much higher concentration of manganese (Figure 2.19), which could exist in multiple valences (+2, +3, +4 and +7). The major oxygen desorption peak at $\sim$ 300°C could be attributed to the release of active chemisorbed oxygen species by the heavily doped zirconia (Figure 2.37). Such oxygen species corresponded to the low-temperature methane activation in 25 wt% Mn$_2$O$_3$-doped 7YZ (Figure 2.35), enabling a remarkably low light-off temperature of 358°C.
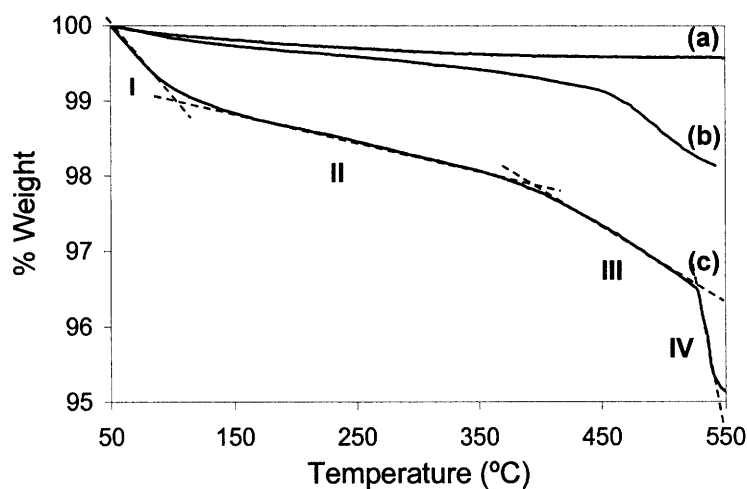
Figure 2.36 TGA profiles for (a) 7YZ, and 7YZ (b) coated and (c) doped with 25 wt% of Mn$_2$O$_3$, after calcination at 700°C in air for 2 h. TGA was performed under 5% CH$_4$ in He at a flow rate of 20 ml/min. The dotted lines were used to identify the four regions with different curvatures in (c).
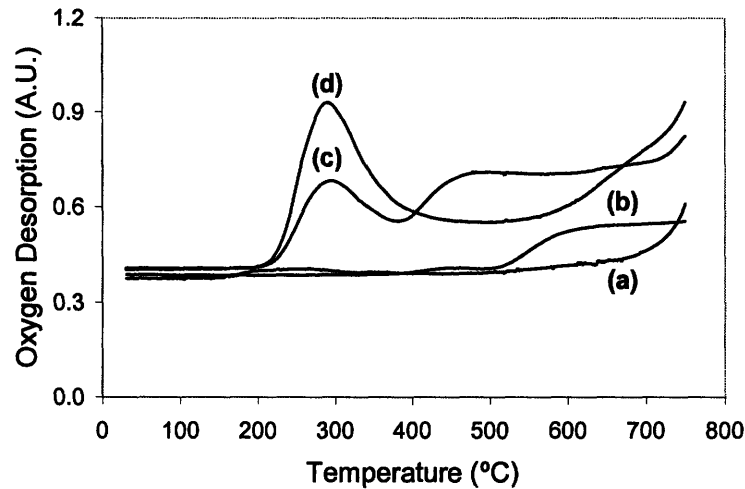
Figure 2.37 TPD of oxygen from (a) Mn_2O_3, (b) 7YZ, and 7YZ (c) coated and (d) doped with 25 wt% of Mn_2O_3, after calcination at 700°C in air for 2 h. TPD was performed in He at a flow rate of 20 ml/min.
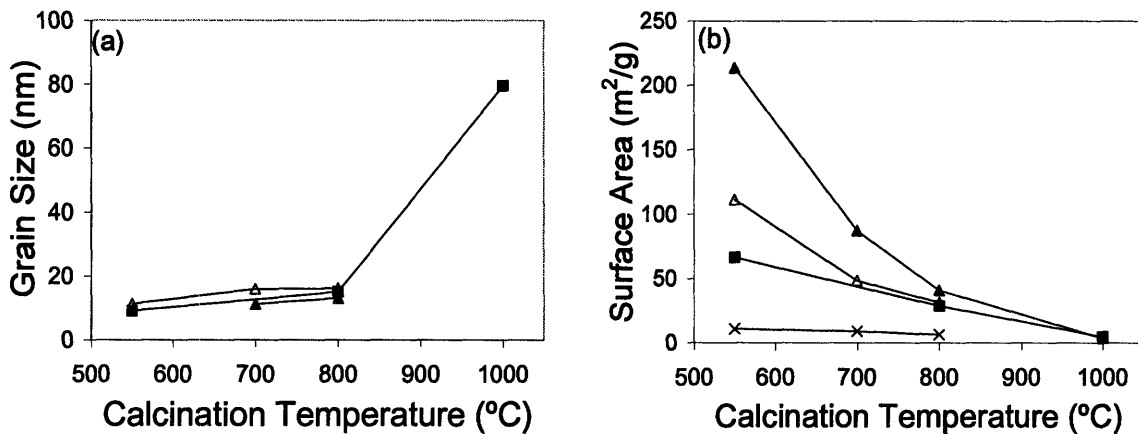
Figure 2.38 (a) Zirconia XRD grain sizes and (b) BET surface areas of (×) Mn_2O_3, (■) 7YZ, and 7YZ (△) coated and (▲) doped with 25 wt% of Mn_2O_3.

Figure 2.39 shows that 25 wt%-coated and doped 7YZ possessed similar XPS O1s and Mn2p$_{3/2}$ peak positions, which were similar to those observed for Mn_2O_3.[34] This indicated that the two samples have similar surface species and oxidation states (Mn^{3+}), This finding could partially explain the similarity in the light-off temperatures for 25 wt% Mn_2O_3-doped 7YZ (358°C) and 25 wt% Mn_2O_3-coated 7YZ (375°C). The two samples have similar bulk Mn concentrations by ICP-AES analysis (Table 2.9). However, 25 wt% Mn_2O_3-coated 7YZ

showed a much higher surface Mn concentration (by XPS analysis) than 25 wt% Mn_2O_3-doped 7YZ. This confirmed that there was more Mn_2O_3 segregated on the surface of the 25 wt% Mn_2O_3-coated 7YZ. However, this higher surface Mn loading did not lead to better catalytic activity. The greater surface area of the 25 wt% Mn_2O_3-doped 7YZ might have given this sample a slight edge in the light-off temperature by providing a superior surface dispersion of active sites.
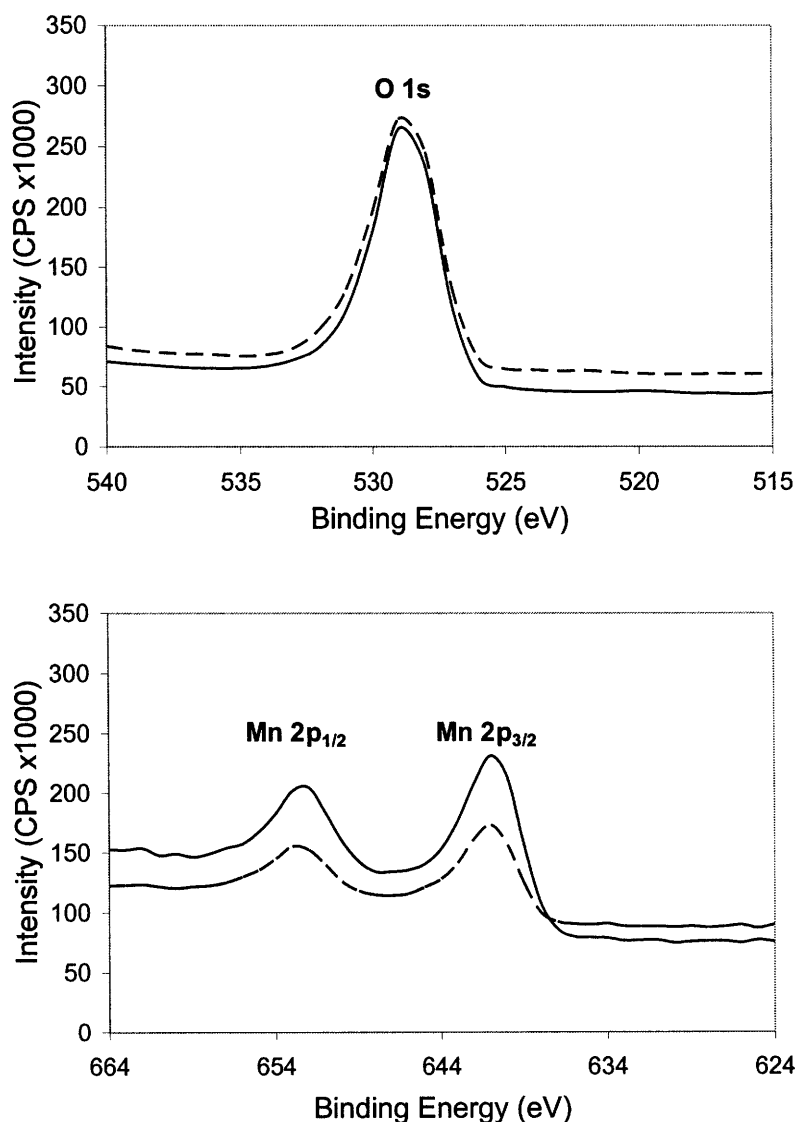
Figure 2.39 XPS spectra of 7YZ (—) coated and (---) doped with 25 wt% of Mn_2O_3.

Table 2.9 Surface and bulk compositions of 25 wt% Mn$_2$O$_3$-coated and doped 7YZ, after calcination at 700°C in air for 2 h.

Catalysts	Surface Concentration (wt%)			Bulk Concentration (wt%)
	Mn	Zr	O	Mn
25 wt% Mn$_2$O$_3$-Coated 7YZ	37.8	33.6	28.6	20.6
25 wt% Mn$_2$O$_3$-Doped 7YZ	20.5	52.9	26.6	20.3

2.3.5.2 Apparent Reaction Rates

Table 2.10 shows the methane and oxygen rate orders for 25 wt% Mn$_2$O$_3$-coated and doped 7YZ measured at 330°C under different gas concentrations, based on the data shown in Figure 2.40. The rate order for methane deviated significantly from unity. This suggested that methane was chemisorbed on the catalyst surface. The Eley-Rideal mechanism, generally accepted for oxidative coupling of methane,[27,30,31] was not applicable at lower temperatures where surface reactions dominated. 25 wt% Mn$_2$O$_3$-coated 7YZ has a similar methane rate order and oxygen rate order as 25 wt% Mn$_2$O$_3$-doped 7YZ, confirming our XPS observation that similar surface species were present in the two samples (Figure 2.39). As the oxygen concentration increased from 7.5% to 21%, methane rate order remained essentially unchanged for both 25 wt% Mn$_2$O$_3$-coated and doped 7YZ.

Table 2.10 Apparent reaction rate orders of CH$_4$ and O$_2$ for methane oxidation over 25 wt% Mn$_2$O$_3$-coated and doped 7YZ. The samples were calcined at 700°C in air for 2 h, and tested at 330°C at various feed gas concentrations.

Catalysts	CH$_4$ Rate Order (α)		O$_2$ Rate Order (β)
	7.5% O$_2$	21% O$_2$	2.0% CH$_4$
25 wt% Mn$_2$O$_3$-Coated 7YZ	0.78	0.80	0.45
25 wt% Mn$_2$O$_3$-Doped 7YZ	0.76	0.75	0.49
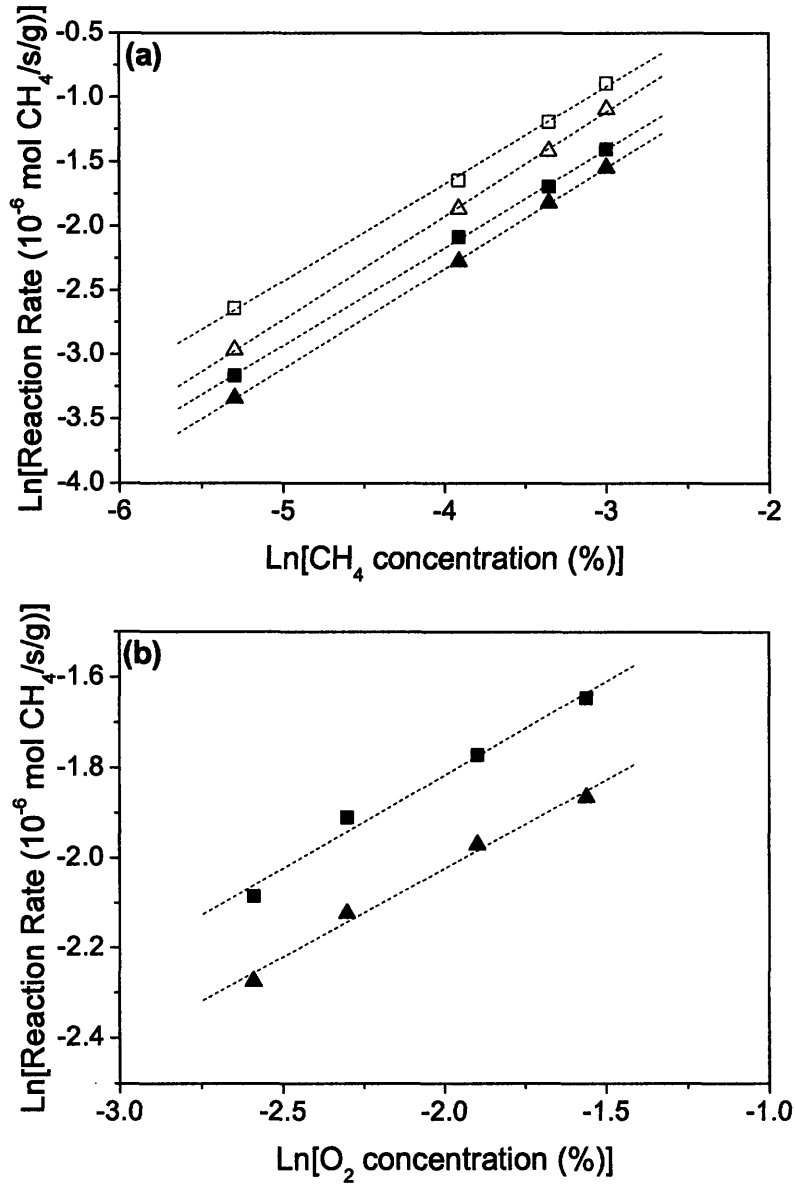
Figure 2.40 Reaction rate as a function of (a) CH_4 concentration for 7YZ (▲, △) coated and (■, □) doped with 25 wt% Mn_2O_3, with O_2 concentration of (▲, ■) 7.5% and (△, □) 21%, and (b) O_2 concentration for 7YZ (▲) coated and (■) doped with 25 wt% Mn_2O_3, with CH_4 concentration of 2.0%, after calcination at 700°C in air for 2 h. Testing was performed at 330°C under different gas concentrations at a flow rate of 100 ml/min.

The apparent activation energies for methane combustion are summarized in Table 2.11, based on the data shown in Figure 2.41. Mn_2O_3 and Mn_2O_3-modified 7YZ showed a much lowered activation energy, which corresponded to the low oxygen desorption

temperatures observed in the TPD curves for these catalysts (Figure 2.37). The most active catalyst, 25 wt% Mn_2O_3-doped 7YZ, has an activation energy of 76 kJ/mol, after calcination at 700°C in air for 2 h. Doping and coating of Mn_2O_3 successfully lowered the activation energy of 7YZ. This corresponded with the greatly reduced light-off temperatures. The remarkably low light-off temperatures were competitive even with the supported Pd and Pt catalysts,[35-37] which are significantly more expensive than our 25 wt% Mn_2O_3-coated and doped 7YZ nanocomposites.

Table 2.11 Light-off temperature and activation energy of 7YZ, and 25 wt% Mn_2O_3-coated and doped 7YZ, after calcination at 700°C in air for 2 h.

Catalysts	Light-off Temperature (°C)	Activation Energy (kJ/mol)
7YZ	558	113 ± 19
Mn_2O_3	398	89 ± 6
25 wt% Mn_2O_3-coated 7YZ	375	85 ± 5
25 wt% Mn_2O_3-doped 7YZ	358	76 ± 5
2.7 wt% Pd/Tetragonal Zirconia[35]	297	—
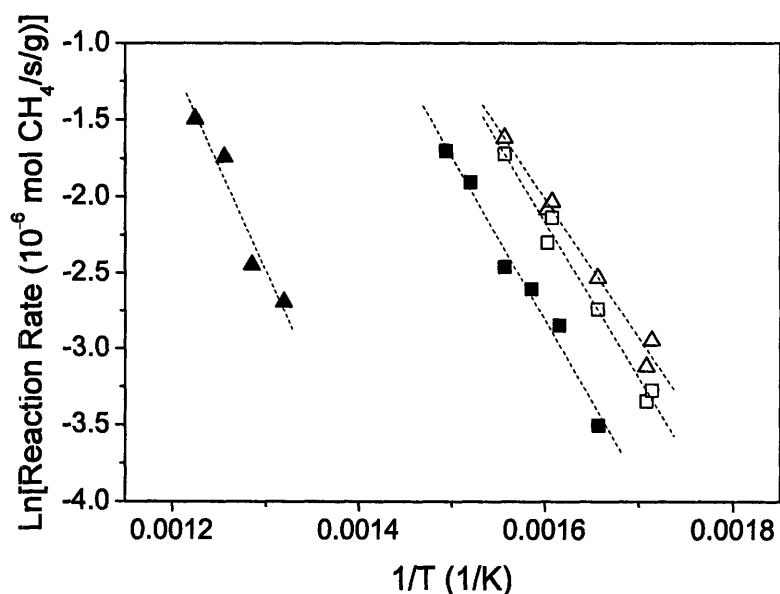
Figure 2.41 Reaction rate as a function of 1/T for (▲) 7YZ, (■) Mn_2O_3, and 7YZ (□) coated and (△) doped with 25 wt% Mn_2O_3, after calcination at 700°C in air for 2 h. Testing was performed with 1% CH_4 in air at a flow rate of 50 ml/min.

2.4 Summary

Nanocrystals of 7YZ were synthesized with ultrafine grain sizes and high surface areas by chemical co-precipitation. They were modified with secondary components, such as Al_2O_3, TiO_2, CeO_2 and Mn_2O_3, in the form of coating or dopants. These modifications led to different dispersion and interaction between the secondary components and 7YZ. They could be employed to significantly improve the thermal stability and catalytic activity of 7YZ-based systems. In particular, CeO_2- and Mn_2O_3-modified 7YZ gave rise to excellent catalytic performance in the flameless combustion of methane. 25 wt% Mn_2O_3-coated 7YZ and 25 wt% Mn_2O_3-doped 7YZ showed remarkably low light-off temperatures of 375°C and 358°C, respectively. These catalysts were highly attractive as they were competitive with the much more expensive supported noble metal catalysts. Their catalytic activity could be attributed to the availability of active surface oxygen species, which facilitated the methane activation at low temperatures.

2.5 References

[1]Energy Information Administration, *International Energy Outlook 2005*, July 2005, Report # DOE/EIA-0484(2005) (2005).

[2]R. E. Hayes, S. T. Kolaczkowski, "Introduction"; pp. 1-95 in *Introduction to Catalytic Combustion*, Gordon and Breach, Australia, (1997).

[3]J. M. Dixon, L. D. LaGrange, U. Merten, C. F. Miller, J. T. Poter II, "Electrical resistivity of stabilized zirconia at elevated temperatures," *J. Electrochem. Soc.*, 110 [4] 276-280 (1963).

[4]Y. W. Li, D. H. He, Q. M. Zhu, X. Zhang, B. Q. Xu, "Effects of redox properties and acid-base properties on isosynthesis over ZrO_2-based catalysts," *J. Catal.*, 221 [2] 584-593 (2004).

[5]M. Labaki, J. F. Lamonier, S. Siffert, E. A. Zhilinskaya, A. Aboukais, "Total oxidation of propene and toluene on copper/yttrium doped zirconia," *Kinet. Catal.*, 45 [2] 227-233 (2004).

[6]C. J. Brinker, G. W. Scherer, "Particulate sols and gels"; pp. 235-302 in *Sol-Gel Science : the Physics and Chemistry of Sol-Gel Processing*, Academic Press, Boston, MA, (1990).

[7]H. Gleiter, "Nanocrystalline materials," *Prog. Mater. Sci.*, 33 [4] 223-315 (1989).

[8]S. R. G. Carrazan, R. Mateos, V. Rives, P. Ruiz, "Influence of the solid state properties of Pd/MO$_x$ (M = Ti, Al) catalysts in catalytic combustion of methane," *Catal. Today*, 112 [1-4] 161-164 (2006).

[9]C. Mateos-Pedrero, S. R. G. Carrazan, P. Ruiz, "Surface modifications of gamma-Al$_2$O$_3$, SiO$_2$ and SnO$_2$ supports by titania grafting and their influence in the catalytic combustion of methane," *Catal. Today*, 112 [1-4] 107-111 (2006).

[10]P. Dinka, A. S. Mukasyan, "*In situ* preparation of oxide-based supported catalysts by solution combustion synthesis," *J. Phys. Chem. B*, 109 [46] 21627-21633 (2005).

[11]Q. Z. Yan, X. T. Su, Z. Y. Huang, C. C. Ge, "Sol-gel auto-igniting synthesis and structural property of cerium-doped titanium dioxide nanosized powders," *J. European Ceram. Soc.*, 26 [6] 915-921 (2006).

[12]J. H. Kim, G. M. Choi, "Mixed ionic and electronic conductivity of [(ZrO$_2$)$_{0.92}$(Y$_2$O$_3$)$_{0.08}$]$_{(1-y)}$·(MnO$_{1.5}$)$_y$," *Solid State Ion.*, 130 [1-2] 157-168 (2000).

[13]A. J. Zarur, J. Y. Ying, "Reverse microemulsion synthesis of nanostructured complex oxides for catalytic combustion," *Nature*, 403 65-67 (2000).

[14]L. Kundakovic, M. Flytzani-Stephanopoulos, "Cu- and Ag-modified cerium oxide catalysts for methane oxidation," *J. Catal.*, 179 [1] 203-221 (1998).

[15]L. H. Xiao, K. P. Sun, X. L. Xu, X. N. Li, "Low-temperature catalytic combustion of methane over Pd/CeO$_2$ prepared by deposition-precipitation method," *Catal. Commun.*, 6 [12] 796-801 (2005).

[16]C. Bozo, N. Guilhaume, E. Garbowski, M. Primet, "Combustion of methane on CeO$_2$-ZrO$_2$ based catalysts," *Catal. Today*, 59 [1-2] 33-45 (2000).

[17]N. Sangar and J. Y. Ying, to be submitted.

[18]N. Sangar, *Nanocrystalline Perovskites for Catalytic Combustion and Oxygen Separation*, Ph.D. Thesis, Massachusetts Institute of Technology, Cambridge, MA, (2002).

[19]E. S. Ahn, N. J. Gleason, A. Nakahira, J. Y. Ying, "Nanostructure processing of hydroxyapatite-based bioceramics," *Nano Lett.*, 1 [3] 149-153 (2001).

[20]E. S. Ahn, N. J. Gleason, J. Y. Ying, "The effect of zirconia reinforcing agents on the microstructure and mechanical properties of hydroxyapatite-based nanocomposites," *J. Am. Ceram. Soc.*, 88 [12] 3374-3379 (2005).

[21]T. Tsukada, S. Venigalla, A. A. Morrone, J. H. Adair, "Low-temperature hydrothermal synthesis of yttrium-doped zirconia powders," *J. Am. Ceram. Soc.*, 82 [5] 1169-1174 (1999).

[22]K. Nakagawa, K. Anzai, N. Matsui, N. Ikenaga, T. Suzuki, Y. H. Teng, T. Kobayashi, M. Haruta, "Effect of support on the conversion of methane to synthesis gas over supported iridium catalysts," *Catal. Lett.*, 51 [3-4] 163-167 (1998).

[23]A. Keshavaraja, N. E. Jacob, A. V. Ramaswamy, "Thermal-decomposition of co-precipitated oxide hydrates of zirconium and manganese," *Thermochim. Acta*, 254 267-275 (1995).

[24]D.-J. Kim, "Lattice parameters, ionic conductivities, and solubility limits in fluorite-structure MO_2 oxide (M = Hf^{4+}, Zr^{4+}, Ce^{4+}, Th^{4+}, V^{4+}) solid solutions," *J. Am. Ceram. Soc.*, 72 [8] 1415-1421 (1989).

[25]R. D. Shannon, "Revised effective ionic radii and systematic studies of interatomic distances in halides and chalcogenides," *Acta Crystallogr. A*, 32 [5] 751-767 (1976).

[26]D. J. Koh, J. S. Chung, Y. G. Kim, J. S. Lee, I.-S. Nam, S. H. Moon, "Structure of Mn-Zr mixed oxide catalysts and their catalytic properties in the CO hydrogenation reaction," *J. Catal.*, 138 [2] 630-639 (1992).

[27]J. L. Dubois, C. J. Cameron, "Common features of oxidative coupling of methane cofeed catalysts," *Applied Catalysis*, 67 [1] 49-71 (1990).

[28]A. Bielanski, J. Haber, "Oxidation of methane"; pp. 423-441 in *Oxygen in Catalysis*, M. Dekker, New York, (1991).

[29]M. Baerns, J. R. H. Ross, "Catalytic chemistry of methane conversion"; pp. 315-335 in *Perspectives in Catalysis*, Blackwell Scientific Publications, Oxford; (1992).

[30]J. H. Lunsford, "Recent advances in the oxidative coupling of methane"; pp. 1-12 in *Natural Gas Conversion II: Proceedings of the Third Natural Gas Conversion Symposium, Sydney, July 4-9, 1993*, Elsevier, Amsterdam, (1994).

[31]J. H. Lunsford, "Oxidative coupling of methane and related reactions"; pp. 1843-1856 in *Handbook of Heterogeneous Catalysis*, Wiley-VCH, Weinheim, (1997).

[32]E. R. Stobbe, B. A. de Boer, J. W. Geus, "The reduction and oxidation behaviour of manganese oxides," *Catal. Today*, 47 [1-4] 161-167 (1999).

[33]D. Dobber, D. Kiessling, W. Schmitz, G. Wendt, "MnO_x/ZrO_2 catalysts for the total oxidation of methane and chloromethane," *Appl. Catal. B - Environ.*, 52 [2] 135-143 (2004).

[34]M. I. Zaki, C. Kappenstein, "X-ray photoelectron spectroscopy and diffractometry of MnO$_x$ catalysts: Surface to bulk composition relationships," *Z. Phys. Chem.*, 176 97-116 (1992).

[35]M. Faticanti, N. Cioffi, S. De Rossi, N. Ditaranto, P. Porta, L. Sabbatini, T. Bleve-Zacheo, "Pd supported on tetragonal zirconia: Electrosynthesis, characterization and catalytic activity toward CO oxidation and CH$_4$ combustion," *Appl. Catal. B - Environ.*, 60 [1-2] 73-82 (2005).

[36]S. Guerrero, P. Araya, E. E. Wolf, "Methane oxidation on Pd supported on high area zirconia catalysts," *Appl. Catal. A - Gen.*, 298 243-253 (2006).

[37]K. Persson, A. Ersson, S. Colussi, A. Trovarelli, S. G. Jaras, "Catalytic combustion of methane over bimetallic Pd-Pt catalysts: The influence of support materials," *Appl. Catal. B - Environ.*, 66 [3-4] 175-185 (2006).

Chapter 3 – Synthesis of Nanocrystalline Yttria-Zirconia Ceramics

3.1 Introduction

Nanostructured ceramics exhibit interesting mechanical properties such as improved hardness and bending strength.[1-4] However, due to processing challenges, systematic study in the nanometer regime remains limited, due to the sensitivity of the properties to the ceramic density.[5] A synthesis/processing scheme that would produce fully dense nanocrystalline ceramics is key towards a systematic investigation of size-dependent properties of ceramics in the submicron regime.

3 mol% yttria-doped zirconia (3YZ) (tetragonal structure) and 8 mol% yttria-doped zirconia (8YZ) (cubic structure) are among the two most studied oxides because of their strong mechanical strength and high electrical conductivity, respectively. These two ceramic systems are also very interesting and challenging due to their simple structures and high sintering temperature requirements.

One of the most effective ways of limiting grain growth in fully dense, single-phase ceramics is to reduce the sintering temperature. However, it is difficult to remove pores trapped in the ceramic body at low sintering temperatures without using high pressures.[6-8] Evans[9] and Vasylkiv et al.[5,10] have indicated that the microstructural inhomogeneity (e.g. due to non-uniform particle packing and presence of agglomerates) was the main obstacle in the densification of ceramics. Efforts to remove the microstructural non-uniformity have been mainly focused on deagglomeration in liquid suspension by casting or electrochemical control of the powder suspension to achieve better particle packing in the ceramic green bodies.[11-13]

The approach presented in this study was different from the conventional strategy. The agglomeration of grains, which were formed naturally during the drying process due to the capillary force associated with water vaporization, was used to achieve a narrow pore size distribution in the green compact. This successfully avoided the formation of larger pores that would grow preferentially at high temperatures. As a result, fully dense nanocrystalline ceramics could be attained at a relatively low sintering temperature without significant grain growth.

71

3.2 Experimental

3.2.1 Synthesis

Hydrothermal treatment was used to provide the powder suspension. This method has been shown to produce finer grain size with a uniform distribution.[8,10,14] The synthesis scheme for the wet processing of nanocrystalline yttria-zirconia ceramics is shown in Figure 3.1. 3YZ and 8YZ were synthesized via chemical co-precipitation.[15] Part of the hydroxide suspension was hydrothermally treated at 180°C for 24 h.[8] The precipitate was collected by centrifuging, and washed thrice in deionized (DI) water (0.1 M). It was then either (i) dried directly to form a dried compact (DC), or (ii) dried and grounded. The powder was (i) subsequently sintered at various temperatures under pressure in a hot press (HP), or (ii) compacted by hydraulic press, and cold isostatically pressed (CIP) at 300 MPa for 3 min in a 7-liter vessel (Fluitron Inc.), followed by sintering at various temperatures without pressure as a powder compact (PC) (Figure 3.1 solid line). Hot pressing was performed under vacuum (Materials Research Furnaces Inc.). The other part of the hydroxide suspension was not hydrothermally treated (see dotted line in Figure 3.1); it was washed, dried, grounded, and calcined at 550°C in air for 2 h. The calcined powders were then hot pressed under vacuum to form the calcined compact (CC).

Figure 3.2 illustrates the processing and sintering of TOSOH© yttria-zirconia powders, non-spray-dried 3 mol% yttria-doped zirconia (TZ-3YB), spray-dried 3 mol% yttria-doped zirconia (TZ-3YSB), and non-spray-dried 8 mol% yttria-doped zirconia (TZ-8Y). These control samples were subjected to conventional ceramic processing, such as hot pressing (HP), pressureless sintering after CIP, or hot isostatic pressing (HIP). All samples were calcined or sintered in air in a Lindberg Model 54434 tube furnace if the temperature was above 1100°C, or a Lindberg Model 55122 hinged tube furnace if the temperature was below 1100°C, unless otherwise specified. CIP was performed at 300 MPa for 3 min, as in the case of PC. HIP was preformed by American Isostatic Presses Inc. (Columbus, OH).
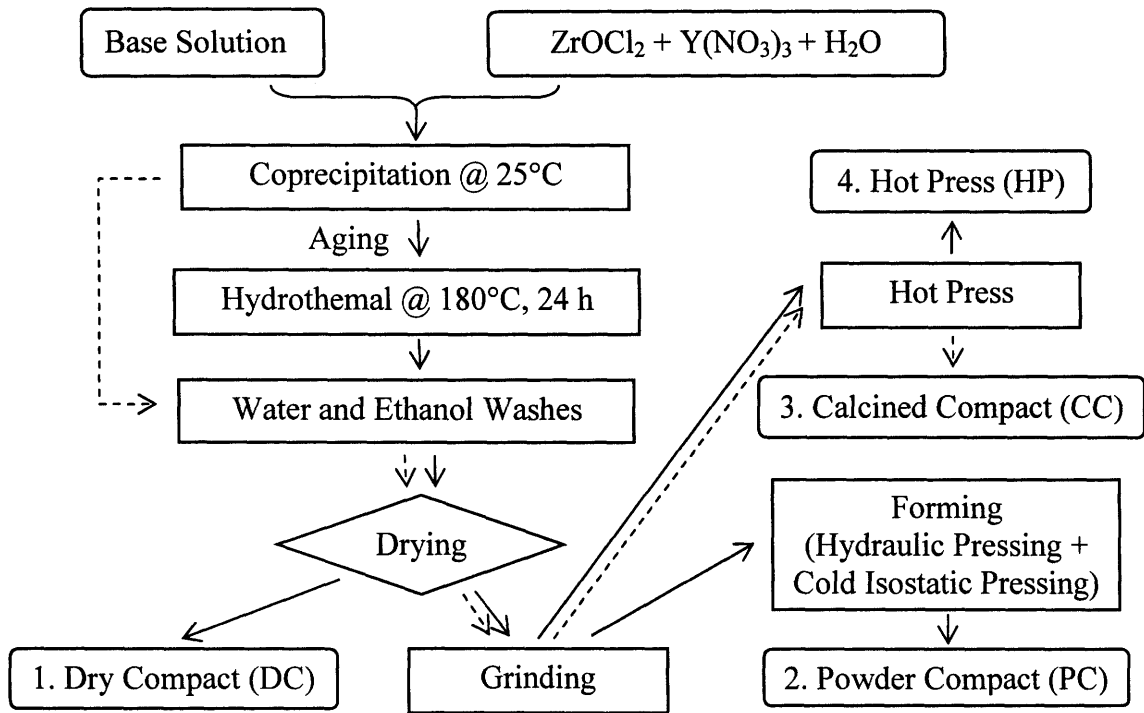
Figure 3.1 Wet processing of nanocrystalline yttria-zirconia ceramics.
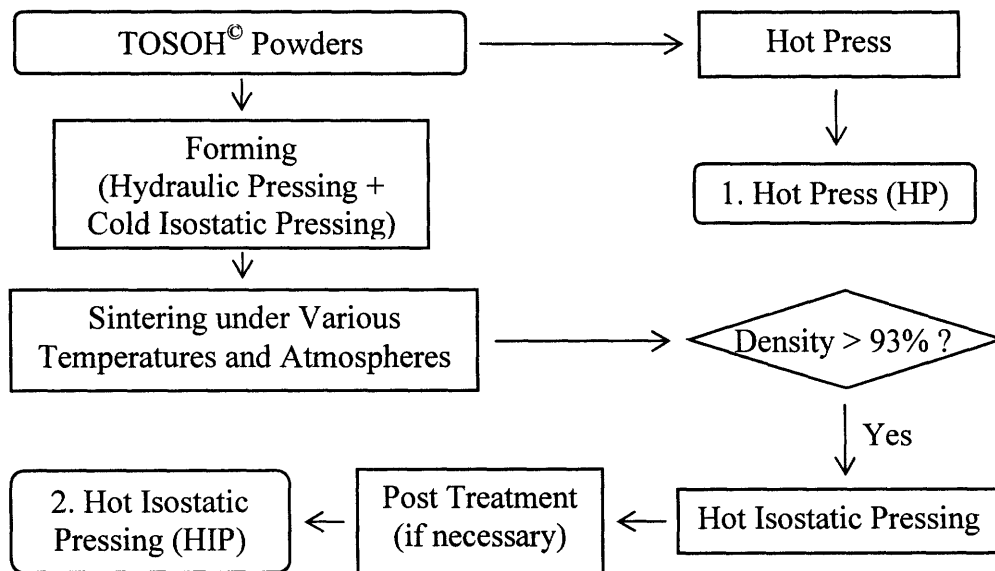
Figure 3.2 Sintering of commercial yttria-zirconia powders.

3.2.2 Characterization

A Siemens D5000 θ-θ X-ray diffractometer (Cu Kα) was used to identify the crystalline phases of powder samples. Average grain sizes were calculated based on peak broadening using Scherer's equation (for grain sizes below 100 nm). All ceramic samples were polished with 1-μm diamond suspension, and thermally etched at 50°C below sintering temperature for 30 min. Their grain sizes were examined by field-emission high-resolution scanning electron microscopy (SEM) (JEOL 6320FV) (for grain sizes below 1 μm) or environmental scanning electron microscopy (ESEM) (FEI/Philips XL30 FEG) (for grain sizes above 1 μm), and calculated according to ASTM E112-96. Archimedes' method was applied to the samples in DI water to determine the ceramic density. N_2 adsorption-desorption isotherms and B.E.T. surface area were obtained with a Micromeritics ASAP 2010 system.

3.3 Results and Discussion

3.3.1 Nanocrystalline Ceramics from Hydrothermally Treated Yttria-Zirconia

3.3.1.1 Characterization of Hydrothermally Treated Powders

3YZ and 8YZ were synthesized via hydrothermal treatment at a controlled pH of ~ 10.5. Figure 3.3 shows that the tetragonal phase and cubic phase associated with 3YZ and 8YZ, respectively, could not be distinguished after calcination at low temperatures due to the nanocrystalline grain sizes. The tetragonal phase of 3YZ was confirmed only after calcination at 1100°C.

Figure 3.4 shows that rapid grain growth occurred at ~ 1000°C for DC, PC and powders of 3YZ and 8YZ. Luo *et al.*'s dilatometric studies of 3YZ indicated that the changes in density as a function of temperature was rapid at 1000–1150°C and at 1250–1330°C.[16] Thus, it would be ideal to achieve ceramic densification below 1000–1150°C in order to suppress grain growth during sintering.
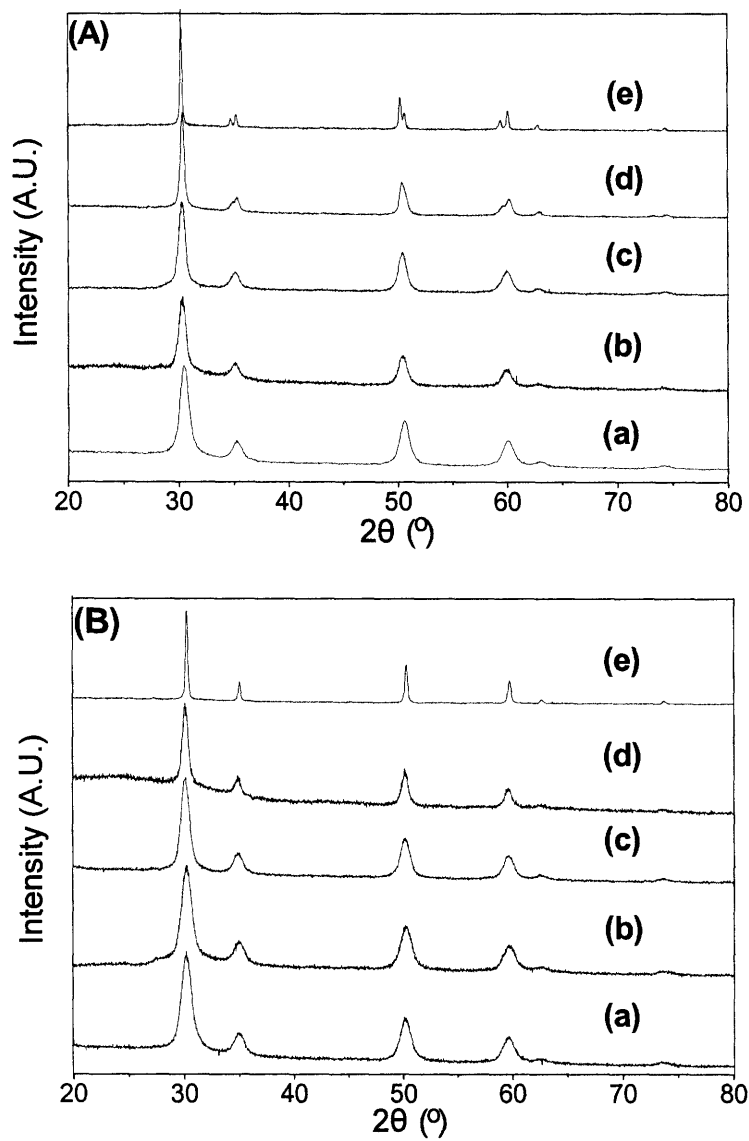
Figure 3.3 XRD patterns of (A) 3YZ and (B) 8YZ powders (a) after hydrothermal treatment at 180°C for 24 h, and after calcination at (b) 550°C, (c) 700°C, (d) 900°C and (e) 1100°C in air for 2 h.
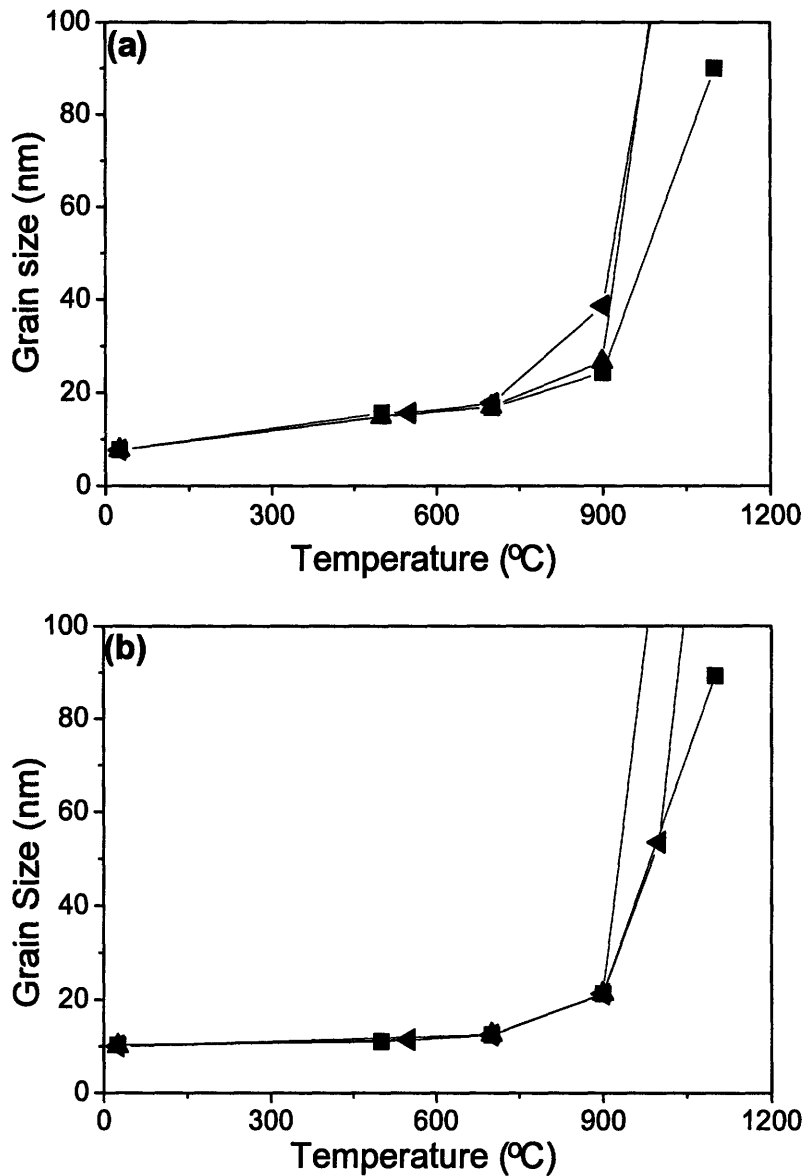
Figure 3.4 Grain sizes of hydrothermally treated (■) DC, (▲) PC and (◄) powders of (a) 3YZ and (b) 8YZ, after calcination at various temperatures in air for 2 h.

3.3.1.2 Sintering of Nanocrystalline Yttria-Zirconia

DC and PC of 3YZ and 8YZ were sintered at various temperatures in air (see Figure 3.5). The CIP samples of TOSOH© TZ-3YB and TZ-8Y were sintered for comparison. All samples started with similar green densities of 48–49%, but demonstrated different sinterability. However, DC of 3YZ and 8YZ achieved > 99% density at 1100°C and 1150°C, respectively, while the CIP samples of commercial powders only attained a density of < 75%

at 1200°C. Figure 3.6 confirmed the successful densification of DC of 3YZ and 8YZ after sintering at 1100°C and 1150°C, respectively. Ultrafine grain sizes averaging ~ 87 ± 2 nm and 85 ± 16 nm were retained at these relatively low sintering temperatures.

Unlike the DC samples, the PC samples of 3YZ and 8YZ did not achieve full densification during the first rapid change in density. Their density reached a plateau at ~ 95%, in agreement with the observation of Sagel-Ransijn et al.[17] The CIP samples TOSOH© TZ-3YB and TZ-8Y were fully densified, but at a much higher temperature of 1400°C.

DC samples of 3YZ and 8YZ were subjected to calcination at higher temperatures beyond full densification for grain growth studies (Figure 3.7 and Figure 3.8). DC of 3YZ showed some grain growth to ~ 146 ± 17 nm upon heating to 1200°C, with minor grain growth to ~ 180 ± 31 nm with further treatment to 1300°C. In contrast, the DC of 8YZ exhibited significant grain growth to ~ 537 ± 34 nm when heated to 1250°C, with continued grain growth to 819 ± 71 nm and 2.8 ± 0.4 μm with further treatment to 1300°C and 1400°C, respectively. The difference in grain evolution between 3YZ and 8YZ could be explained by the different grain growth activation energy of 105 kcal/mol for tetragonal zirconia and 69 kcal/mol for cubic zirconia.[18,19] The difficulty in achieving 8YZ with ultrafine grains under normal sintering conditions has also been noted in the literature.[7]

Hot pressing has been known to be effective in closing residual pores and in establishing a positive sintering pressure[20] to suppress grain growth. Since hydrothermally treated 3YZ and 8YZ powders could achieve full density as DC at 1100°C and 1150°C, respectively, these powders were also subjected to hot-pressing under various pressures in vaccum for 1 h at 1100°C and 1150°C, respectively. Figure 3.9 shows that increasing pressure led to improved densification for HP samples. A pressure of 150 MPa was sufficient to fully densify 3YZ at 1100°C, 8YZ at 1150°C, TZ-3YB at 1100°C, and TZ-8Y at 1150°C. Grain sizes of 75 ± 3 nm, 151 ± 10 nm, 78 ± 4 nm, and 154 ± 16 nm were attained (see Figure 3.10). When a non-hydrothermally treated 3YZ powder was hot-pressed (CC), full density was not achieved at 1100°C, even at 150 MPa.
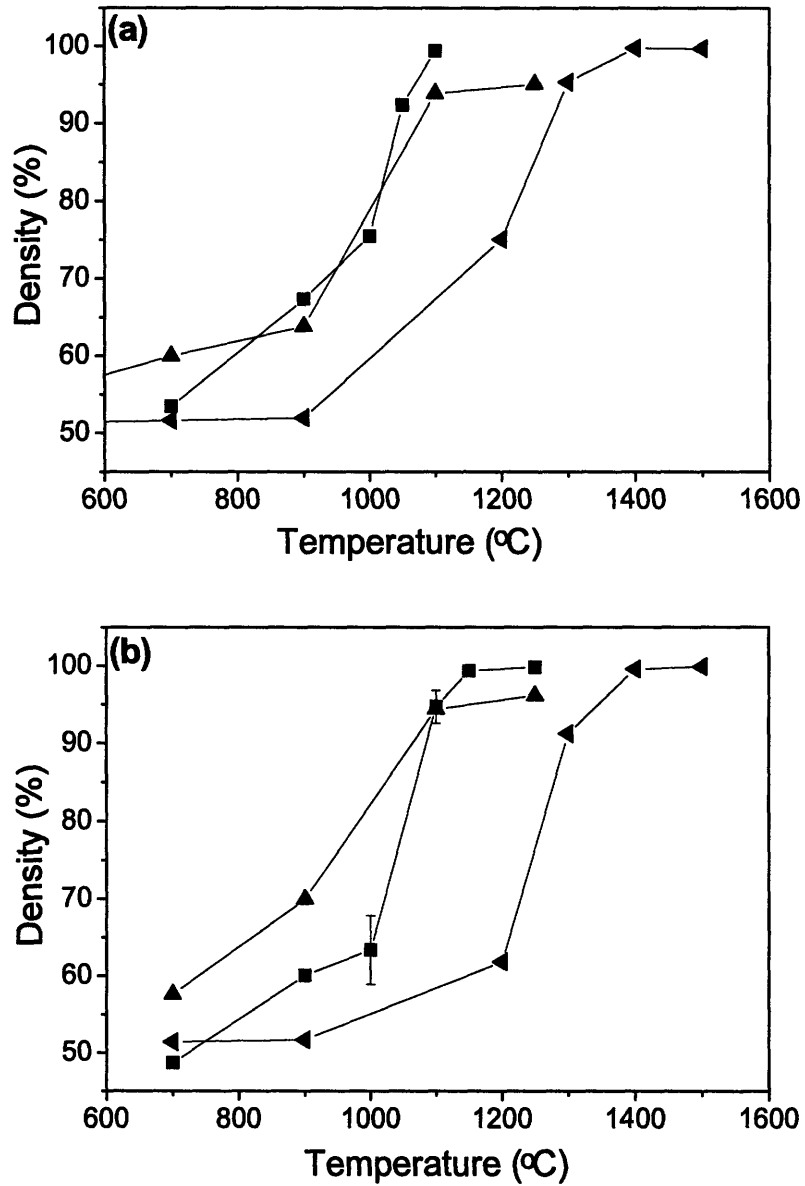
Figure 3.5 Densities of (■) DC and (▲) PC of (a) 3YZ and (b) 8YZ after sintering at various temperatures in air for 2 h. (◄) Densification curves of CIP TOSOH© (a) TZ-3YB and (b) TZ-8Y are also shown for comparison.
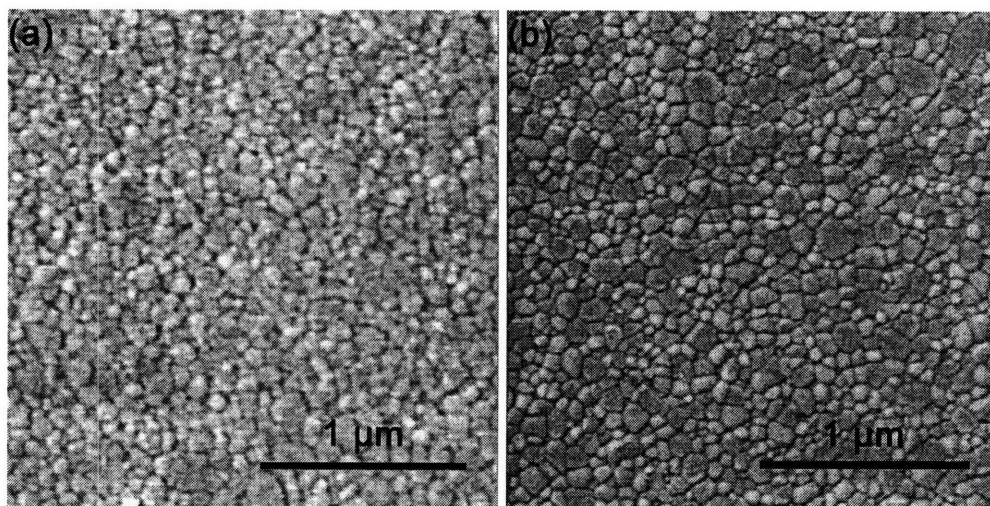
Figure 3.6 SEM images of DC of (a) 3YZ sintered at 1100°C in air for 2 h, and (b) 8YZ sintered at 1150°C in air for 2 h.
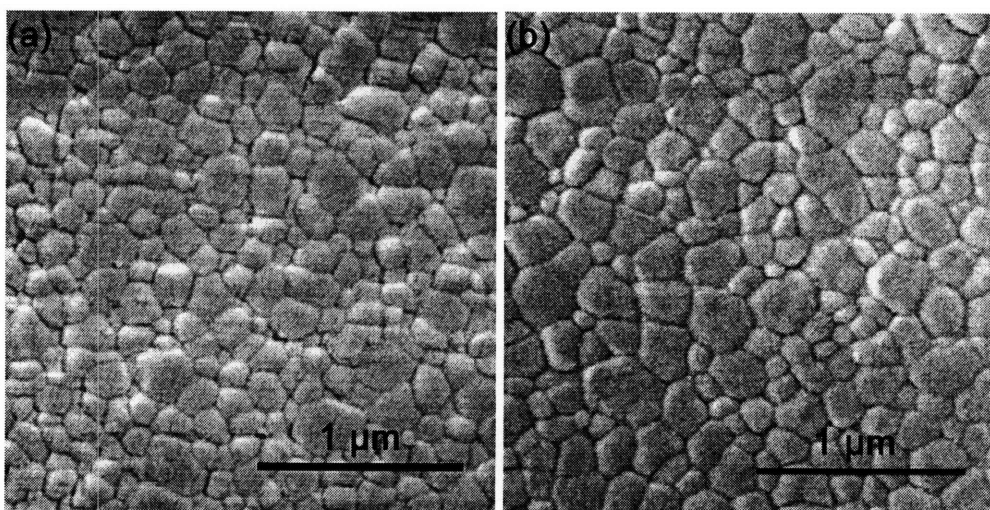
Figure 3.7 SEM images of DC of 3YZ sintered at (a) 1200°C and (b) 1300°C in air for 2 h.
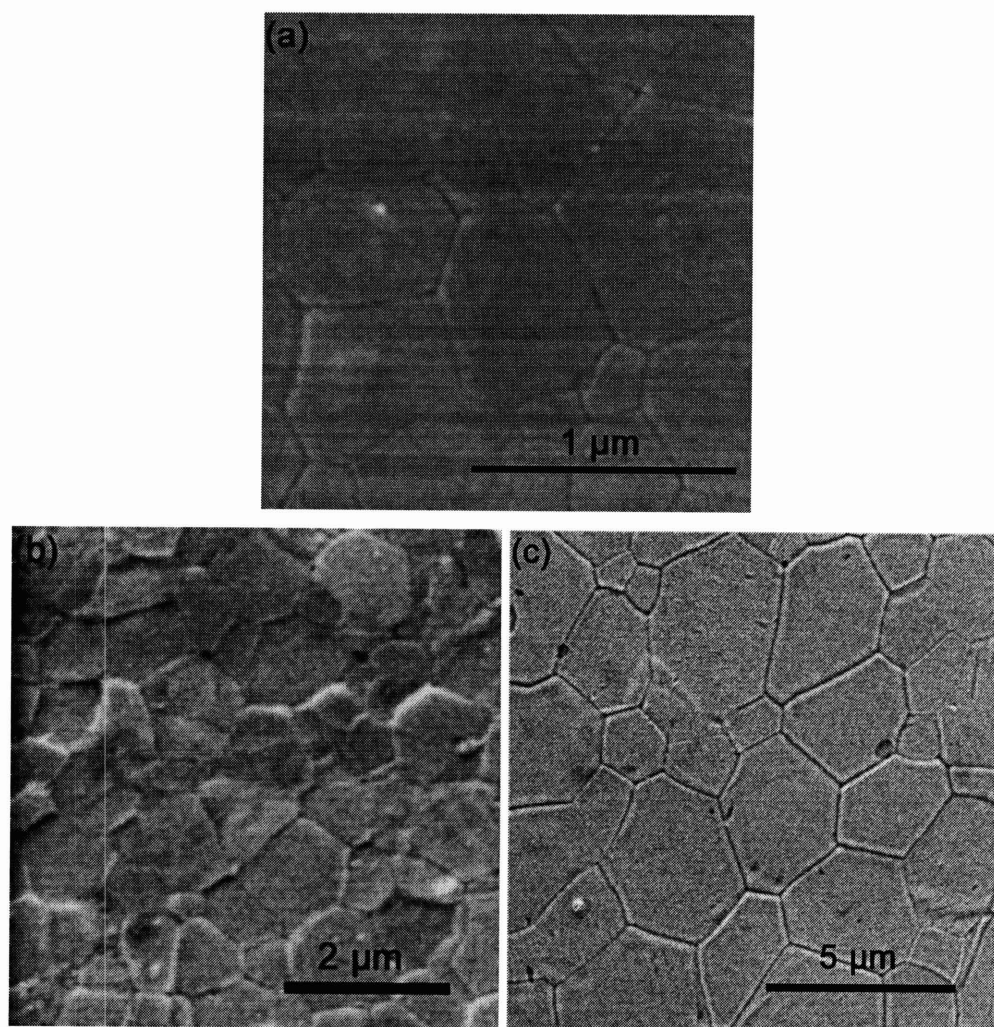
Figure 3.8 SEM/ESEM images of DC of 8YZ sintered at (a) 1250°C, (b) 1300°C and (c) 1400°C in air for 2 h.
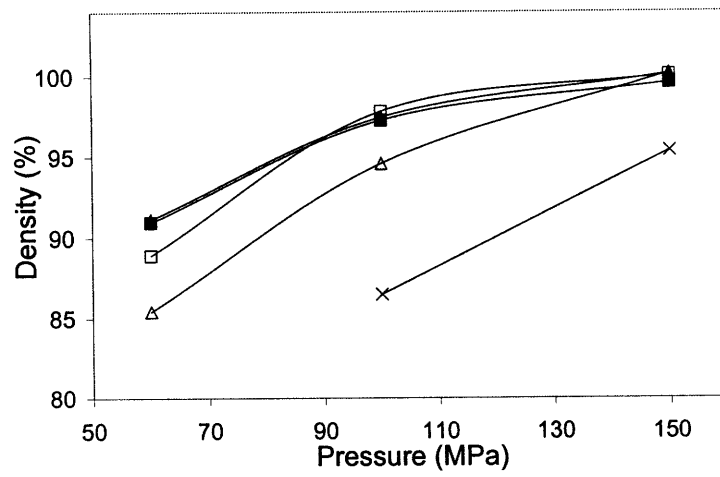
Figure 3.9 Density of HP samples of (▲) 3YZ at 1100°C, (■) 8YZ at 1150°C, (Δ) TZ-3YB at 1100°C and (□) TZ-8Y at 1150°C, and (×) CC sample of 3YZ at 1100°C under various pressures in vacuum.
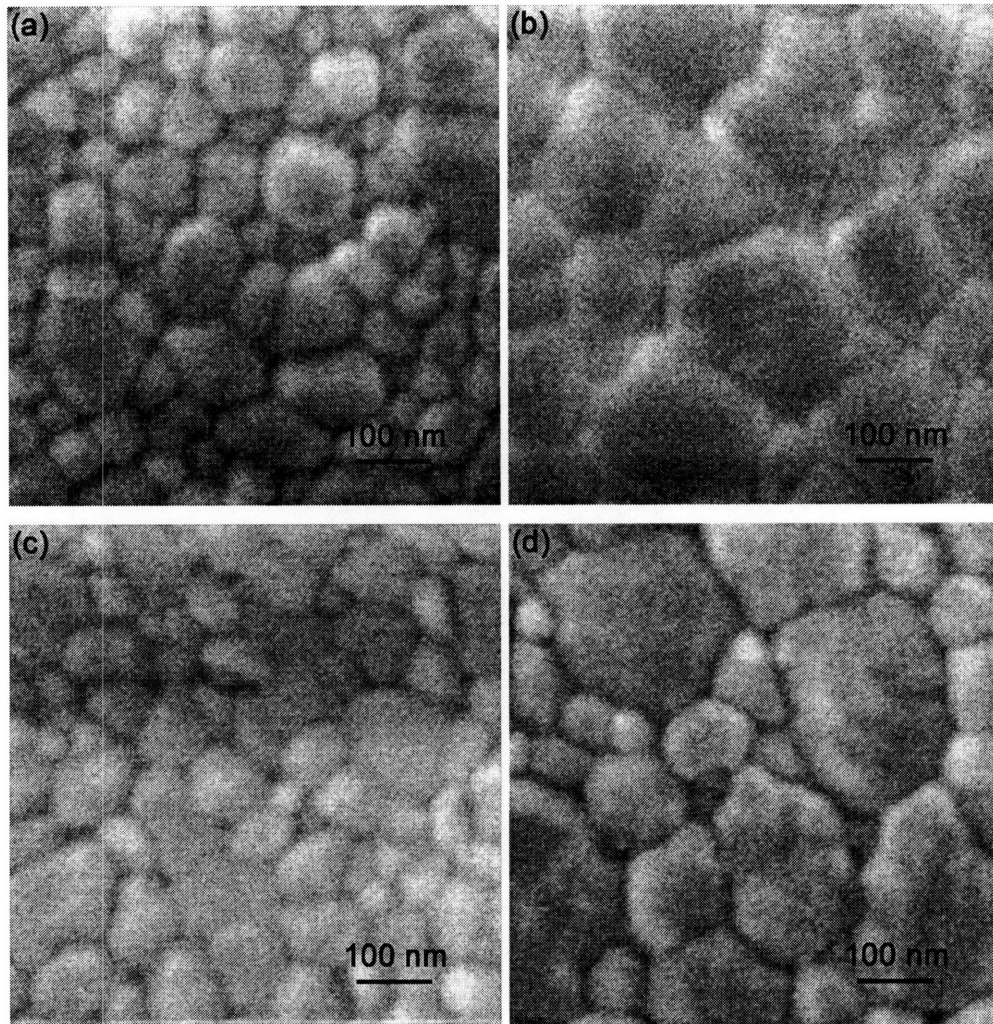
Figure 3.10 SEM images of HP samples of (a) 3YZ at 1100°C, (b) 8YZ at 1150°C, (c) TZ-3YB at 1100°C, and (d) TZ-8Y at 1150°C under 150 MPa in vacuum.

3.3.1.3 Discussion

DC was shown to have a better sinterability than other compacts. Thus, DC of 8YZ was further examined to elucidate its characteristics in relation to sintering kinetics.

Porosimetry of 8YZ

Hydrothermally treated 8YZ powders calcined to various temperatures consisted of near-spherical grains with a uniform size distribution (Figure 3.11). It has a similar pore size distribution as its DC before calcination (Figure 3.12(a)). At low temperatures (< 700°C), both 8YZ powders and DC showed only one peak at a pore size below 20 nm, while 8YZ PC showed an additional peak at ~ 30 nm. The presence of two peaks in pore size distribution has

also been reported by Luo *et al.* on ceramics based on calcined powders.[16] Sintering studies indicated that densification was not initiated below 900°C (Figure 3.5(b)). Thus, the fine pores in 8YZ powders and DC at low temperatures were intraagglomerate pores. The additional peak at ~ 30 nm in 8YZ PC could be attributed to the forming process, which included CIP at 300 MPa. These 30-nm pores might be due to interagglomerate pores, which were finer than the typical micron-sized pores observed in the conventional systems.[21]
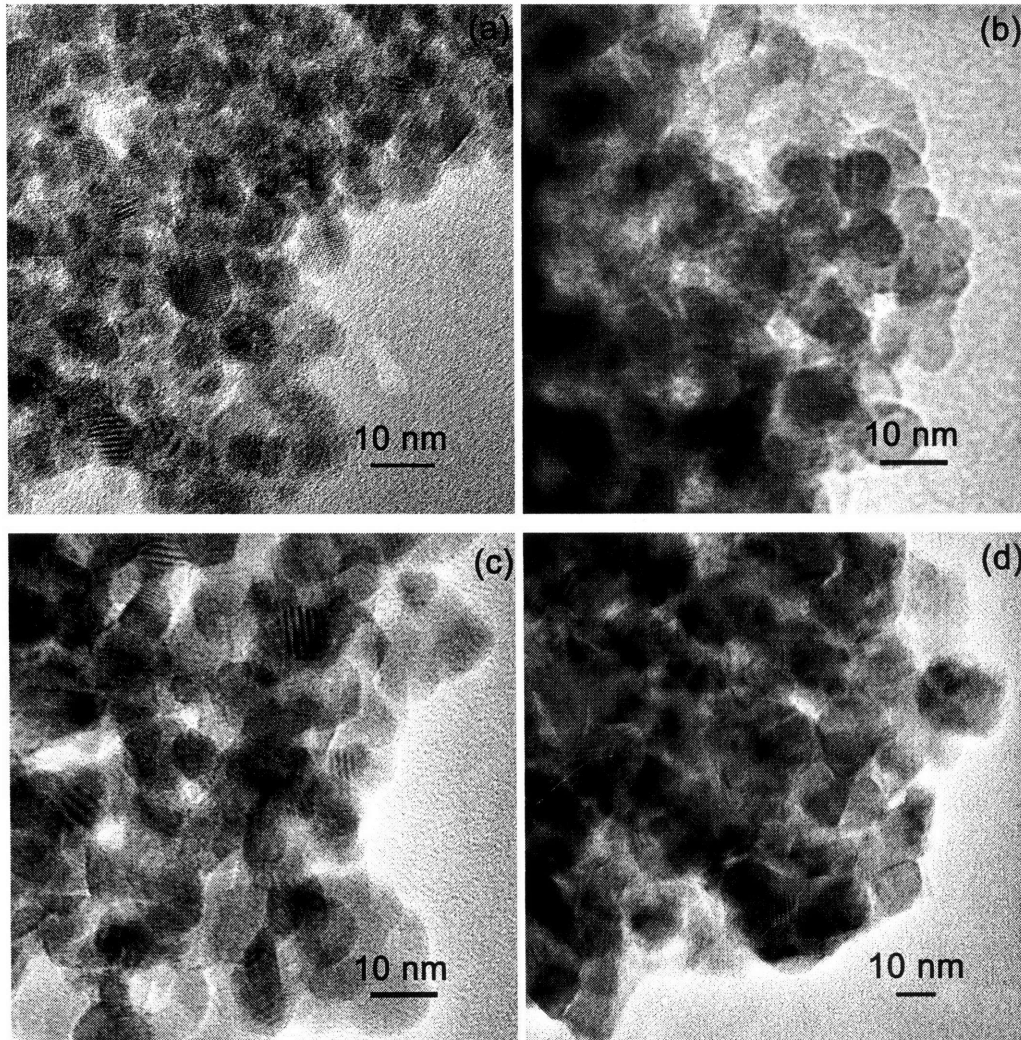
Figure 3.11 TEM micrographs of hydrothermally treated 8YZ powders (a) before calcination, and after calcination at (b) 550°C, (c) 700°C and (d) 900°C in air for 2 h.
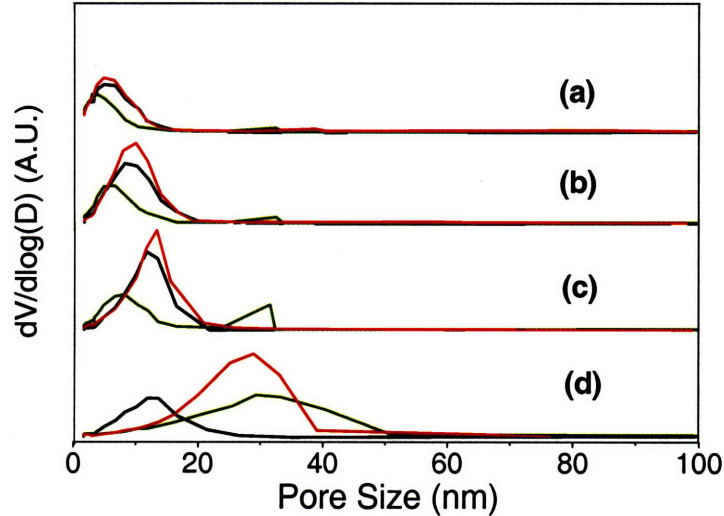
Figure 3.12 Pore size distributions of hydrothermally treated 8YZ (—) powders, (—) DC and (—) PC (a) before calcination, and after calcination at (b) 550°C, (c) 700°C and (d) 900°C in air for 2 h.

After calcination at 900°C, 8YZ powders and PC showed broad pore size distributions of 10–40 and 10–50 nm, respectively, while the DC displayed a sharp pore size distribution of < 20 nm. The broadening of the pore size distribution in 8YZ PC could be attributed to the pore growth and evolution at the expense of finer pores. The single, narrow pore size distribution of the DC greenbody prevented the pore growth during sintering at higher temperatures. This allowed the DC to be completely densified in one step between 900°C and 1150°C (see Figure 3.5(b)). According to Luo *et al.*'s dilatometry findings,[16] the small pores would collapse in the first sintering step at 1000–1150°C, while the larger pores could only be eliminated in a second sintering step. This explained why the PC could only be densified to 95% at 1200°C; a second sintering step would be needed to collapse its larger pores of > 20 nm.

Effect of pH on 8YZ DC

8YZ DC was formed by direct drying of the washed powders. The uniform greenbody of the DC was key towards rapid sintering in one step. The low-temperature sinterability of 8YZ DC in turn allowed a dense nanocrystalline ceramic to be attained. Therefore, pH adjustment aimed at breaking up agglomerates during casting[11] should not have a significant impact on the sinterability of 8YZ DC. This was demonstrated in Figure 3.13, which showed

that the effect of suspension pH was negligible on the final density of 8YZ DC. We note that only a narrow pH range could be examined since stoichiometric 8YZ has to be processed in a narrow pH range due to the solubility difference between yttrium and zirconium ions in water.[14]
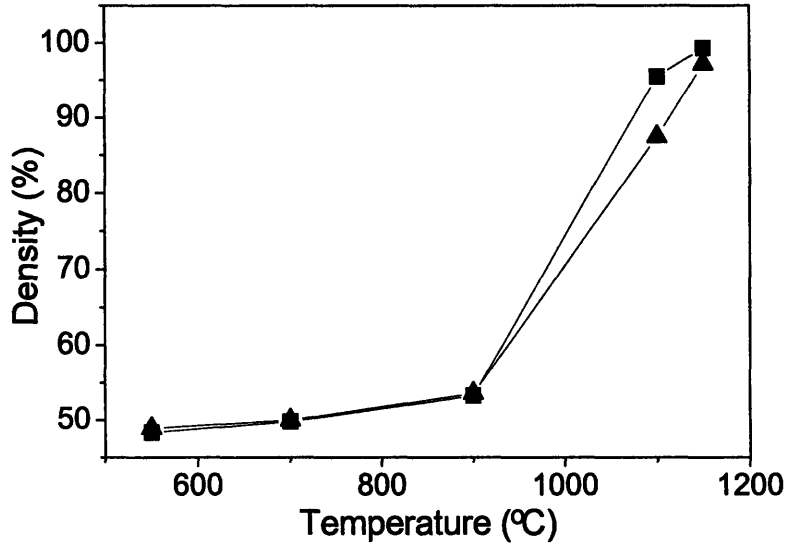
Figure 3.13 Densification of 8YZ DC at various temperatures in air for 2 h. The samples were first processed at a pH of (▲) 10.0 and (■) 10.5.

Sintering Kinetics

Coarsening (grain growth) and densification are the two processes that often occurred simultaneously during ceramic sintering. The relative rate of these processes determines the microstructure of the sintered body. To study the sintering kinetics of various systems in their final sintering stages, Cannon and Yan developed a model for normal coarsening and densification.[22,23] In this model, standard graphs of relative grain size (D/D_0) vs. density were calculated for different coarsening and densification mechanisms, and values of relative coarsening/densification ratios were presented graphically. Comparing our experimental graphs with these standard graphs, we could gain insights into the microstructural evolution during the final-stage sintering.

Using this model, the relative grain size (D/D_0) for 8YZ DC and PC was studied as a function of density, with D_0 represented the grain size of 8YZ DC and PC at 70% density

(21.3 nm and 22.0 nm, respectively). Compared to the PC, the DC possessed negligible pores of > 20 nm (Figure 3.12). This facilitated the low-temperature sintering, allowing one-step densification with little grain growth. The main difference between DC and PC of 8YZ was the geometric factors along the grain boundaries of the green body. Since pores were not present within the grains, grain boundary diffusion would control the densification process during sintering. Thus, the extent of grain growth during the final stage of sintering could be given by the relative coarsening/densification ratio (Γ),[23]

$$\Gamma = \frac{3}{176} \frac{\omega D_s}{\delta D_{gb}} \frac{\gamma_{gb}}{\gamma_s}$$

(3.1)

where D_s and D_{gb} = surface and grain boundary diffusivities, respectively, γ_s and γ_{gb} = surface and grain boundary energies, respectively, and ω and δ = effective widths of surface and grain boundary diffusion, respectively. Since it can be assumed that the surface and grain boundary diffusivities and energies are fixed values for a given system, only the geometric values ω and δ may be varied. Further examination of these two values suggested that ω should also be a fixed value for 8YZ DC and PC. By comparing Figure 3.14 with the standard graph of grain boundary and surface diffusion controlled sintering,[22] Γ value of 8YZ DC was determined to be ~ 3–6 times higher than that of 8YZ PC. Thus, the grain boundary diffusion width in 8YZ PC should be ~ 3–6 times that of 8YZ DC. This calculation agreed with the difference in pore size between 8YZ PC (~ 30 nm) and DC (~ 10 nm) (Figure 3.14).
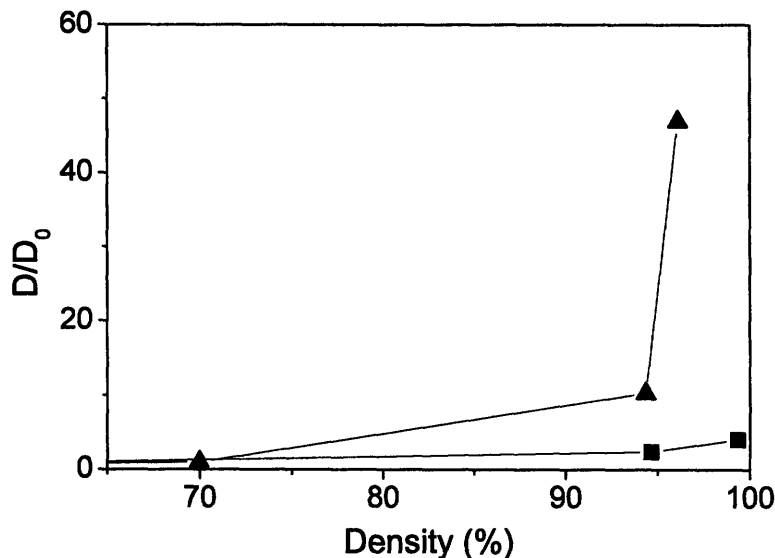
Figure 3.14 Relative grain size as a function of density for 8YZ (■) DC and (▲) PC.

3.3.2 Yttria-Zirconia Ceramics from TOSOH[©] Powders

3.3.2.1 Pressureless Sintering of TOSOH[©] Powders

Due to the low grain growth activation energy of 8YZ, 3YZ was examined in detail for the processing of commercial powders. Non-spray-dried TZ-3YB and spray-dried TZ-3YSB from TOSOH[©] were selected based on the study of Gibson et al.[24] Their characteristics are summarized in Table 3.1. After CIP under 300 MPa for 3 min, the green densities of all TZ-3YB and TZ-3YSB samples were ~ 48–49%.

Table 3.1 Characteristics of TOSOH[©] TZ-3YB and TZ-3YSB powders.

	Grain Size (nm)	Surface Area (m^2/g)	Pore Volume (cm^3/g)
TZ-3YB	54	11	0.044
TZ-3YSB	98	5	0.013

Figures 3.15–3.17 show the evolution of grain size and density of TZ-3YB and TZ-3YSB with sintering. TZ-3YB and TZ-3YSB grew to 265 ± 6 nm and 186 ± 11 nm, respectively by 1300°C. Further grain growth was observed at 1500°C, especially when the sample was sintered for 24 h instead of 2 h. 1400°C and 1500°C were required for the full densification of TZ-3YB and TZ-3YSB, respectively, in pressureless sintering in air. The non-

spray-dried TZ-3YB powder was more easily sintered than the spray-dried TZ-3YSB powder, possibly due to its starting powder characteristics, i.e. finer grain size and higher surface area. Compared to TZ-3YB and TZ-3YSB, the hydrothermally treated nanocrystalline 3YZ DC could be sintered at a much lower temperature of 1100°C (Figure 3.5(a)). As a result, its grain size could be effectively controlled in the fully densified ceramics to be < 100 nm (Figure 3.5(a)), unlike the commercial TOSOH[©] samples.
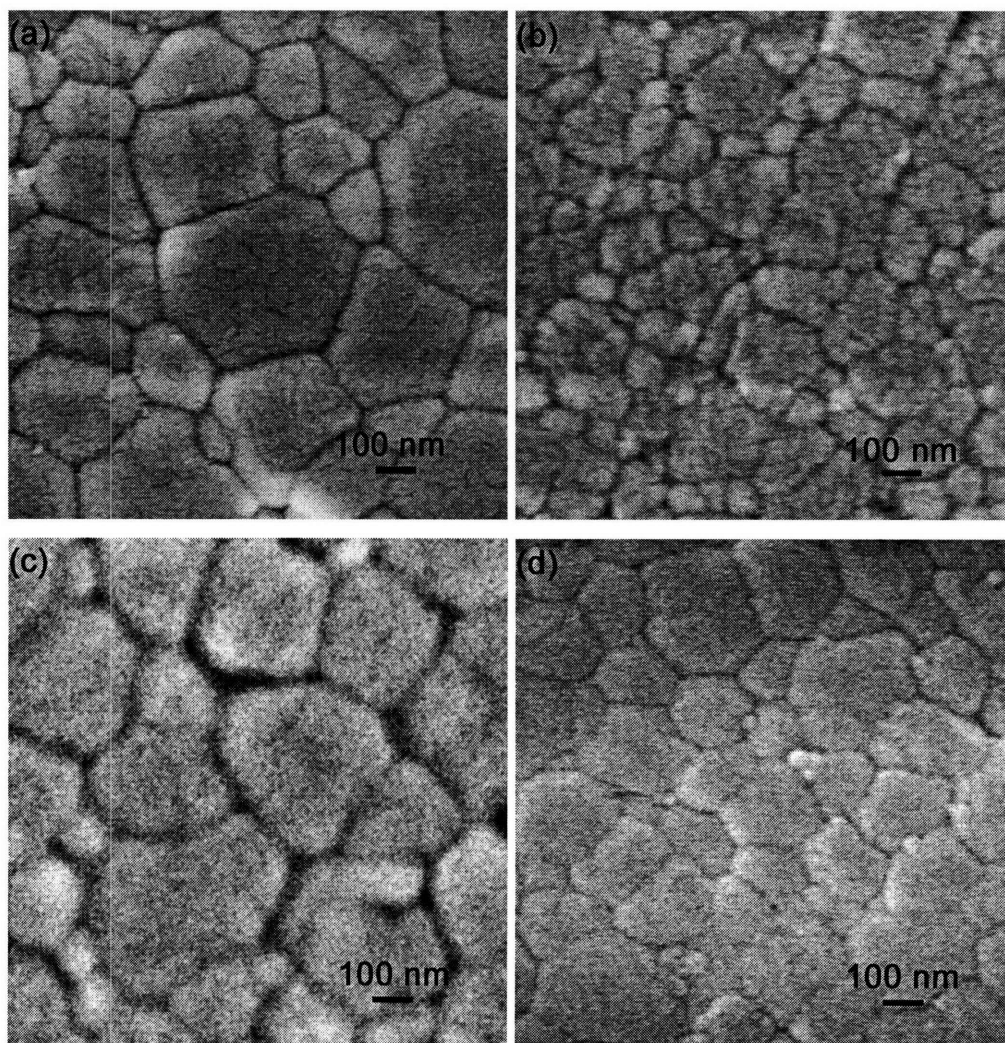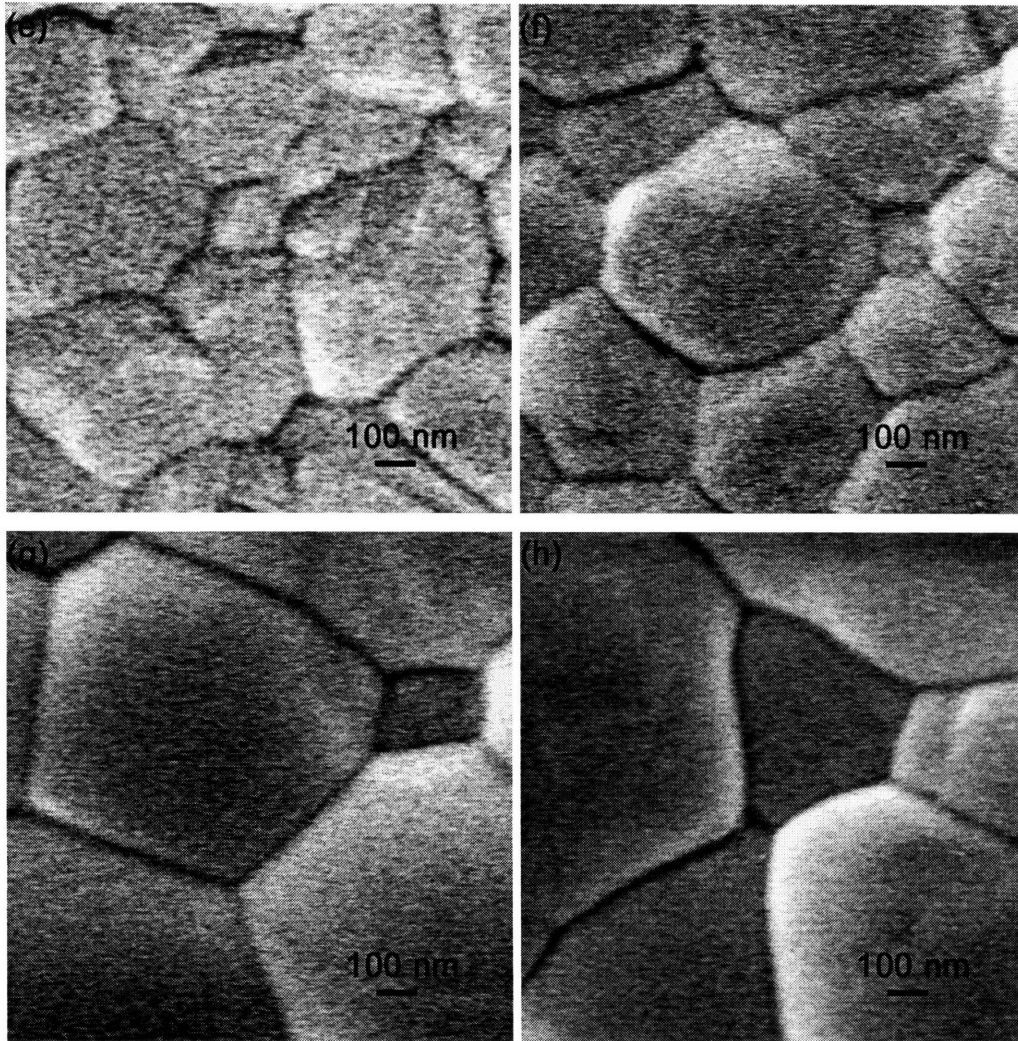
Figure 3.15 SEM/ESEM images of (a,c,e,g) TZ-3YB and (b,d,f,h) TZ-3YSB after sintering in air at (a,b) 1300°C for 2 h, (c,d) 1400°C for 2 h, and 1500°C for (e,f) 2 h and (g,h) 24 h.
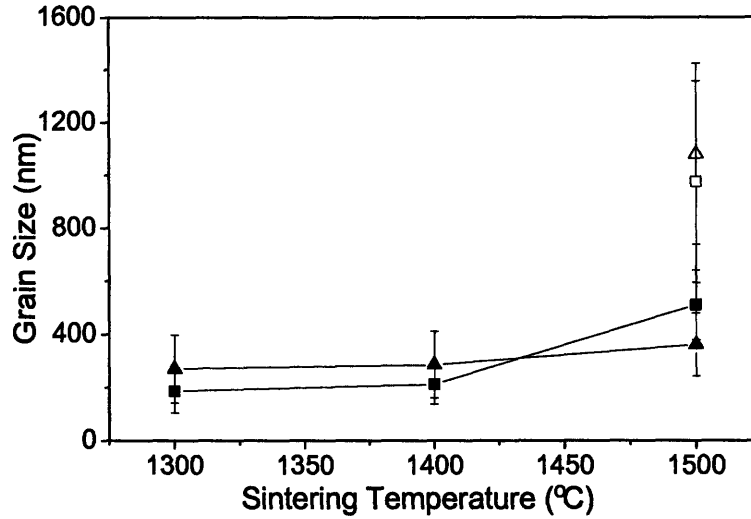
Figure 3.16 Grain size of (▲,△) TZ-3YB and (■,□) TZ-3YSB after sintering at various temperatures in air for (▲,■) 2 h and (△,□) 24 h.
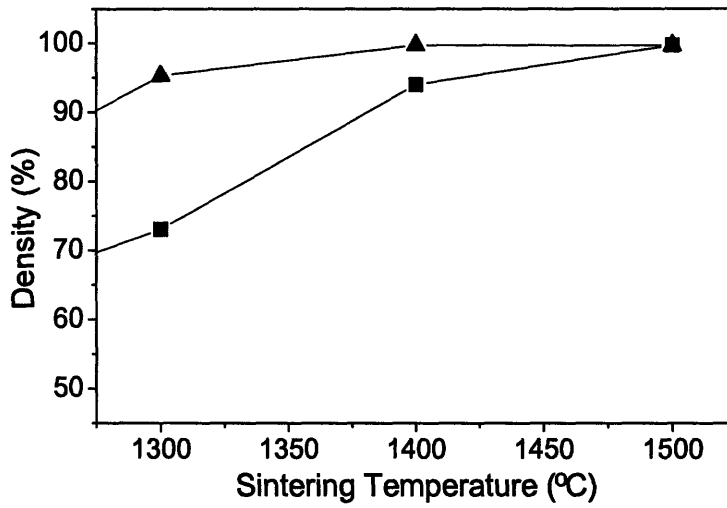
Figure 3.17 Density of (▲) TZ-3YB and (■) TZ-3YSB after sintering at various temperatures in air for 2 h.

To reduce grain size in densification, an inert gas atmosphere (argon) was used during sintering as recommended by Yan.[22] Figure 3.18 illustrates that the grain growth of TZ-3YB was suppressed in inert atmosphere only at sintering temperatures of ≤ 1400°C. Since TZ-3YB could be densified at 1400°C in argon, there was some benefit in using the inert

atmosphere for its sintering, which lowered the grain size of the densified TZ-3YB ceramics from 285 ± 6 nm (Figure 3.15(c)) to 236 ± 3 nm (Figure 3.19(b)).
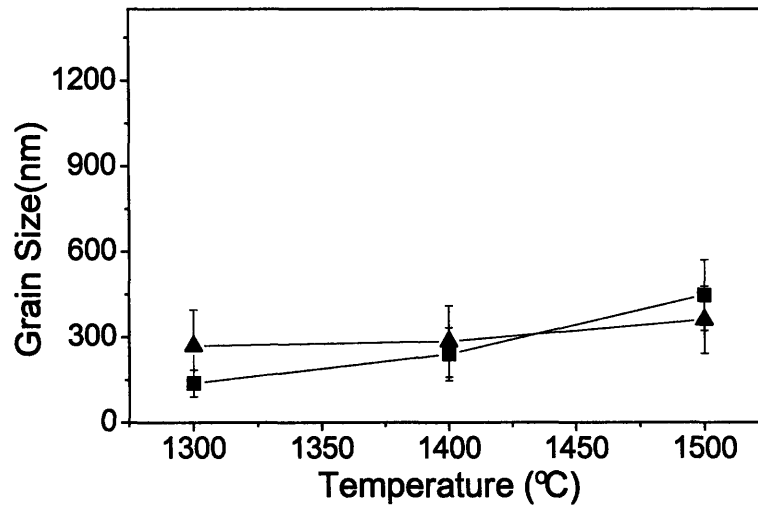
Figure 3.18 Grain size of TZ-3YB after sintering at various temperatures for 2 h in (▲) air and (■) argon.
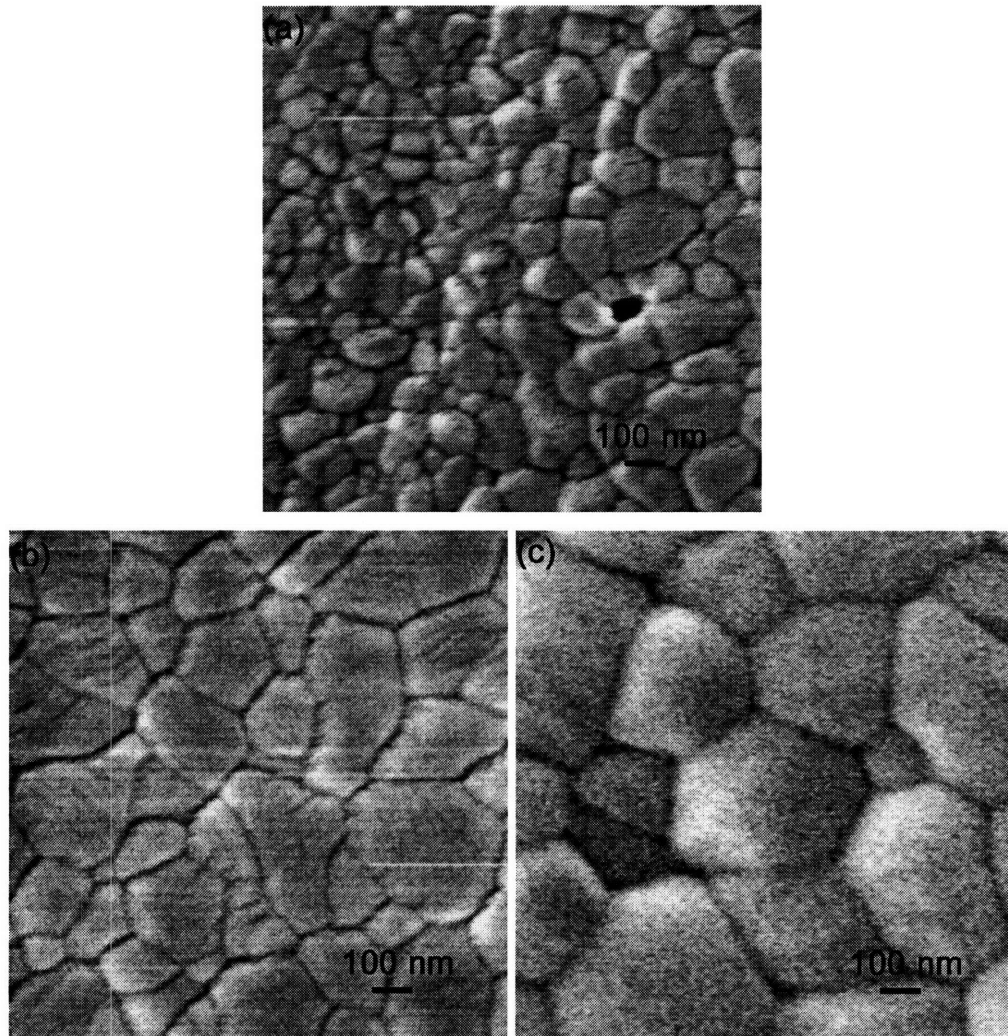
Figure 3.19 SEM images of TZ-3YB after sintering at (a) 1300°C, (b) 1400°C and (c) 1500°C in argon for 2 h.

3.3.2.2 Hot Isostatic Pressing of TOSOH© Powders

For the TOSOH© powders, pressureless sintering in argon presented some benefits in suppressing grain growth for sintering at ≤ 1400°C. In this study, HIP was applied to close the residual pores in TZ-3YB and TZ-3YSB samples that have been presintered under argon. Table 3.2 shows that TZ-3YB could be successfully densified by HIP at 1200°C in argon after presintering at 1300°C in argon. In contrast, TZ-3YSB could not be densified by HIP at 1200–1300°C in argon after presintering at 1300°C in argon. This was due to the limited density of the 1300°C-presintered TZ-3YSB. For this spray-dried powder, it was necessary to presinter at 1400°C in argon prior to HIP. The smallest grains achieved by 3YB and 3YSB

HIP samples that were fully densified were ~ 150 nm and 220 nm, respectively (see Figure 3.20(a) and (b), respectively). It was found that HIP did not give rise to substantial grain growth when performed at temperatures lower than the presintering temperature. Thus, HIP could be effectively applied to remove the residual pores after > 93% density has been achieved with presintering. This allowed lower temperatures to be used for densification, and thereby provided for dense ceramics with finer grains. Nevertheless, the finest grain sizes achieved by the fully dense TOSOH© TZ-3YB and TZ-3YSB via presintering and HIP were still coarser than the finest grain size attained by hydrothermally treated nanocrystalline 3YZ DC (~ 87 nm). This could be attributed to the nanocrystalline 3YZ synthesis that provided ultrafine grain size of < 10 nm, and the DC processing that led to uniform pores of < 20 nm.

Table 3.2 Densities of TZ-3YB and TZ-3YSB subjected to HIP at 200 MPa at various temperatures in argon for 1 h, after presintering at 1300°C or 1400°C in argon for 2 h.

	Presintering Temperature (°C)	% Density Achieved after HIP		
		HIP @ 1200°C	HIP @ 1250°C	HIP @ 1300°C
3YB	1300	99.8	99.9	99.9
	1400	99.8	99.8	100.0
3YSB	1300	73.2	75.1	77.9
	1400	99.0	99.9	99.5
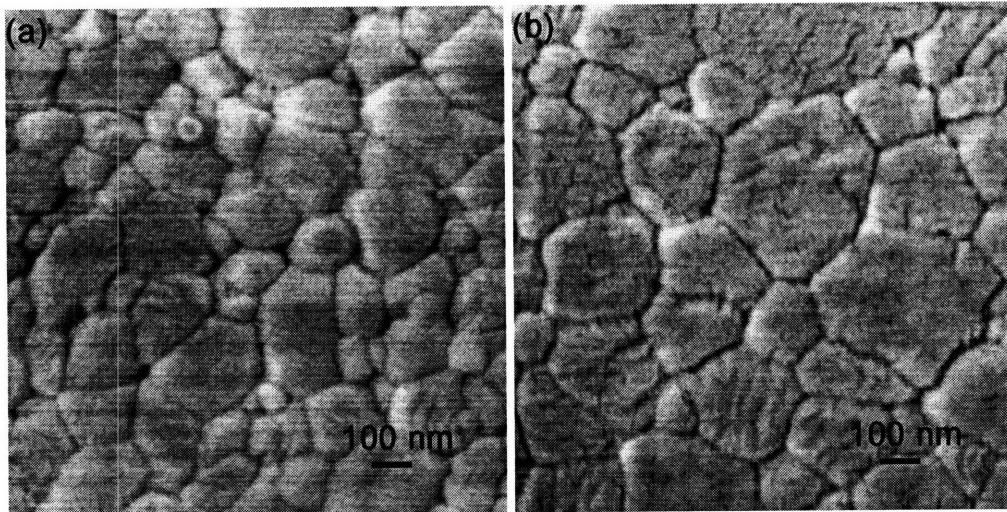
Figure 3.20 SEM images (a) 3YB presintered at 1300°C in argon for 2 h and HIP at 200 MPa and 1200°C in argon for 1 h, and (b) 3YSB presintered at 1400°C in argon for 2 h and HIP at 200 MPa and 1200°C in argon for 1 h.

3.4 Summary

Nanocrystalline 3 mol% and 8 mol% yttria-zirconia ceramics with an ultrafine grain size of < 90 nm were successfully achieved by pressureless sintering at 1100°C and 1150°C, respectively. The low-temperature sinterability could be attributed to the well-defined nanocrystalline particles obtained via hydrothermal synthesis, and the elimination of secondary porosity through the dry compact processing.

Submicron-sized 3 mol% yttria-zirconia ceramics with a grain size of ~ 150 nm was obtained with commercial TOSOH© powders. Grain growth during densification was successfully suppressed by presintering to 93% density under an argon atmosphere (i.e. at 1300°C), followed by HIP in argon at a temperature lower than the presintering temperature (i.e. 1200°C).

Using different starting powders and processing approaches, dense yttria-zirconia ceramics with controlled grain sizes of ≥ 85 nm could be attained. This would be very useful for the systematic studies of various ceramic properties as a function of grain size.

3.5 References

[1]R. W. Rice, C. C. Wu, F. Boichelt, "Hardness-grain-size relations in ceramics," *J. Am. Ceram. Soc.*, 77 [10] 2539-2553 (1994).

[2]R. Vassen, D. Stover, "Processing and properties of nanophase ceramics," *J. Mater. Process. Technol.*, 93 77-84 (1999).

[3]E. S. Ahn, N. J. Gleason, A. Nakahira, J. Y. Ying, "Nanostructure processing of hydroxyapatite-based bioceramics," *Nano Lett.*, 1 [3] 149-153 (2001).

[4]E. S. Ahn, N. J. Gleason, J. Y. Ying, "The effect of zirconia reinforcing agents on the microstructure and mechanical properties of hydroxyapatite-based nanocomposites," *J. Am. Ceram. Soc.*, 88 [12] 3374-3379 (2005).

[5]O. Vasylkiv, Y. Sakka, V. V. Skorokhod, "Low-temperature processing and mechanical properties of zirconia and zirconia-alumina nanoceramics," *J. Am. Ceram. Soc.*, 86 [2] 299-304 (2003).

[6]J. Li, H. Liao, L. Hermansson, "Sintering of partially-stabilized zirconia and partially-stabilized zirconia-hydroxyapatite composites by hot isostatic pressing and pressureless sintering," *Biomaterials*, 17 [18] 1787-1790 (1996).

[7]U. Anselmi-Tamburini, J. E. Garay, Z. A. Munir, "Fast low-temperature consolidation of bulk nanometric ceramic materials," *Scr. Mater.*, 54 [5] 823-828 (2006).

[8]N. Sangar, J. Y. Ying, To be submitted.

[9]A. G. Evans, "Considerations of inhomogeneity effects in sintering," *J. Am. Ceram. Soc.*, 65 [10] 497-501 (1982).

[10]O. Vasylkiv, Y. Sakka, "Synthesis and colloidal processing of zirconia nanopowder," *J. Am. Ceram. Soc.*, 84 [11] 2489-2494 (2001).

[11]A. Krell, P. Blank, H. W. Ma, T. Hutzler, M. P. B. van Bruggen, R. Apetz, "Transparent sintered corundum with high hardness and strength," *J. Am. Ceram. Soc.*, 86 [1] 12-18 (2003).

[12]J. Helbig, *Wet processing of nanosized ceramic particles*, D.Tech.Sc. Thesis, Swiss Federal Institute of Technology, Zurich, Switzerland, (2000).

[13]W. H. Rhodes, "Agglomerate and particle-size effects on sintering yttria-stabilized zirconia," *J. Am. Ceram. Soc.*, 64 [1] 19-22 (1981).

[14]T. Tsukada, S. Venigalla, A. A. Morrone, J. H. Adair, "Low-temperature hydrothermal synthesis of yttrium-doped zirconia powders," *J. Am. Ceram. Soc.*, 82 [5] 1169-1174 (1999).

[15]J. Cui, J. Y. Ying, To be submitted.

[16]J. Luo, S. Adak, R. Stevens, "Microstructure evolution and grain growth in the sintering of 3Y-TZP ceramics," *J. Mater. Sci.*, 33 [22] 5301-5309 (1998).

[17]C. D. Sagel-Ransijn, A. J. A. Winnubst, B. Kerkwijk, A. J. Burggraaf, H. Verweij, "Production of defect-poor nanostructured ceramics of yttria-zirconia," *J. Eur. Ceram. Soc.*, 17 [6] 831-841 (1997).

[18]I.-W. Chen, L. A. Xue, "Development of superplastic structural ceramics," *J. Am. Ceram. Soc.*, 73 [9] 2585-2609 (1990).

[19]I. G. Lee, I.-W. Chen, "Sintering and grain growth in tetragonal and cubic zirconia"; pp. 340-345 in *Sintering '87*, Elsevier Applied Science, New York, NY, USA, (1988).

[20]V. V. Srdic, M. Winterer, H. Hahn, "Sintering behavior of nanocrystalline zirconia prepared by chemical vapor synthesis," *J. Am. Ceram. Soc.*, 83 [4] 729-736 (2000).

[21]P. Bowen, C. Carry, "From powders to sintered pieces: forming, transformations and sintering of nanostructured ceramic oxides," *Powder Technol.*, 128 [2-3] 248-255 (2002).

[22]M. F. Yan, "Microstructural control in the processing of electronic ceramics," *Mater. Sci. Eng.*, 48 [1] 53-72 (1981).

[23]N. J. Shaw, "Densification and coarsening during solid-state sintering of ceramics - A review of the models .3. Coarsening," *Powder Metall. Int.*, 21 [6] 25-29 (1989).

[24]I. R. Gibson, G. P. Dransfield, J. T. S. Irvine, "Sinterability of commercial 8 mol% yttria-stabilized zirconia powders and the effect of sintered density on the ionic conductivity," *J. Mater. Sci.*, V33 [17] 4297-4305 (1998).

Chapter 4 – Mechanical Properties of Nanocrystalline Yttria-Zirconia Ceramics

4.1 Introduction

Ceramics with ultrafine grain sizes exhibit interesting mechanical properties such as improved hardness and bending strength.[1-4] However, due to processing challenges, systematic studies of ceramics with nanometer-sized grains have been limited, especially for properties sensitive to ceramic density.[5] Consequently, in contrast to the significant literature in nanocrystalline metals, much less research has been reported on nanostructured ceramics. Existing literature on nanocrystalline ceramics is mostly focused on synthesis.[5,6] Thus, this chapter is devoted towards establishing a relationship between mechanical properties and grain sizes for nanocrystalline ceramics.

3 mol% yttria-zirconia (3YZ) and 8 mol% yttria-zirconia (8YZ) are among the most studied ceramic systems due to their high mechanical strength and electrical conductivity, respectively. Through novel processing, we have shown that the grain sizes of these ceramics could be successfully maintained below 100 nm while achieving > 99% density (Chapter 3).[7] The availability of such ultrafine-grained ceramics and the possibility to attain controlled grain sizes in 3YZ and 8YZ would allow us to examine the nanocrystalline and polycrystalline ceramics systematically.

Traditional micro-indentation and instrumented indentation with a maximum load in the milliNewton range were used to investigate the hardness and Young's modulus. The sensitivity of the local structure of ceramics to the instrumented indentation would provide insights into the mechanical properties of nanocrystalline ceramics. The fracture toughness of the materials was also calculated in this study.

4.2 Experimental

4.2.1 Sample Preparation

Nanocrystalline and submicron 3YZ and 8YZ ceramics synthesized in Chapter 3[7] were calcined to various temperatures to achieve the desired grain sizes. 3YZ was stabilized in the tetragonal phase, while 8YZ possessed a cubic structure, as confirmed by X-ray diffraction

(XRD) patterns. The ceramics were polished and finished with 1-μm diamond suspension. The samples were treated so as to reveal the grain structures after the mechanical testing, and to release residual stresses created during synthesis, if any, prior to each test. They were annealed at 50°C below the previous calcination temperature in air for 30 min, and then cooled to room temperature at a controlled rate of -100°C/h.

4.2.2 Materials Characterization

Micro-indentation was performed on polished ceramic surfaces for a duration of 15 sec with a LECO DM-400 hardness tester equipped with Vickers diamond indenter. A load of 300 gf was selected to avoid undesired fractures on 8YZ indentation surface under high loadings. Both 1 kgf and 300 gf loads were applied to 3YZ samples. All test results were averaged over 10 points.

Instrumented indentation via a Micro Materials NanoTest with NT2 and MT pendulums was used to record real-time relationship between the load (30–500 mN and > 500 mN, respectively) and the displacement. Based on the information obtained in nano-indentation, the Young's modulus E, Vickers hardness H_V, and fracture toughness K_C were calculated based on the following equations.[8-11]

$$E = \left(1 - \nu^2\right)\left(\frac{1}{E_r} - \frac{1 - \nu_i^2}{E_i}\right)^{-1} \qquad \text{Eq. (4.1)}$$

$$\text{where} \quad E_r = \frac{1}{2}\sqrt{\frac{\pi}{A}}\frac{dP}{dh} \qquad \text{Eq. (4.2)}$$

$$\text{and} \quad H_v = \frac{P}{26.43h^2} \qquad \text{Eq. (4.3)}$$

$$K_C = \alpha\sqrt{\frac{E}{H_v}}\frac{P_{max}}{c^{3/2}} \qquad \text{Eq. (4.4)}$$

where ν is the Poisson's ratio of the sample, E_r is the reduced modulus, and E_i and ν_i are the Young's modulus and the Poisson's ratio of the indenter, respectively. Only the values from non-cracked indents were evaluated. The data were obtained for each unloading curve in the range of 60–100% for NT2 pendulum, or 80–100% for the MT pendulum, and averaged over

10 points. A, h and P are the indentation area, indentation depth and load during the test, respectively. a and c are geometrical constant and radial/median crack length, respectively.

The indents were examined right after each test with a field emission high-resolution scanning electron microscope (FE-SEM) (JEOL 6320FV) for ceramics with grain sizes of < 1 μm, or with an environmental scanning electron microscope (ESEM) (FEI/Philips XL30 FEG) for ceramics with grain sizes of ≥ 1 μm. The grain sizes were calculated according to ASTM E112-96. The existence of surface cracks (if any) around the indents was verified with SEM/ESEM. Due to the methods employed in this study, sub-surface cracks could be missed.

4.3 Results and Discussion

4.3.1 Grain Size Control of Yttria-Zirconia Ceramics

The study of mechanical properties as a function of ceramic grain size required fully dense ceramic samples with a specified grain size over the nanometer and micrometer ranges. Chapter 3[7] showed that ceramics with > 99% density could be achieved with a grain size of ~ 90 nm for hydrothermally treated 3YZ and 8YZ, and a grain size of ~ 150 nm for TOSOH© 3YZ after hot isostatic pressing (HIP) at 200 MPa in argon for 1 h.

Hydrothermally treated 3YZ and 8YZ could attain full density by pressureless sintering at 1100°C and 1150°C, respectively. Their grain sizes could be increased in a controlled manner by raising the sintering temperatures. In contrast, fully dense ceramics of TOSOH© powders could only be achieved at temperatures above 1500°C via pressureless sintering. Thus, TOSOH© TZ-3YB and TZ-3YSB ceramics were obtained by HIP, and then subjected to post-treatment to attain grain size control. They were annealed at various temperatures for different periods as shown in Table 4.1.

The grain sizes of tetragonal 3YZ ceramics were controlled between ~ 90 nm and ~ 1 μm (Figure 4.1), while the grain sizes of cubic 8YZ could be varied between ~ 150 nm and ~ 5 μm (Figure 4.2). In 3YZ, a cubic phase was found to crystallize in the tetragonal matrix when grains grew to the micron level (Figure 4.3). Matsui et al. suggested that this phenomenon was due to the segregation of yttrium ions to the tetragonal grain boundaries at elevated temperatures.[12] Therefore, 3YZ was not examined beyond a grain size of 1 μm.

Table 4.1 Grain size of ceramics derived from TOSOH© powders, after sintering by HIP and after post-treatment at various conditions.

| Grain Size (nm) | Sintering | | Post-Treatment | | | |
| | HIP @ 200 MPa | | Anneal @ 1350°C | | Anneal @ 1400°C | |
	1200°C	1300°C	2 h	12 h	2 h	12 h
TZ-3YB	156	—	201	270	213	354
TZ-3YSB	—	218	262	304	276	397
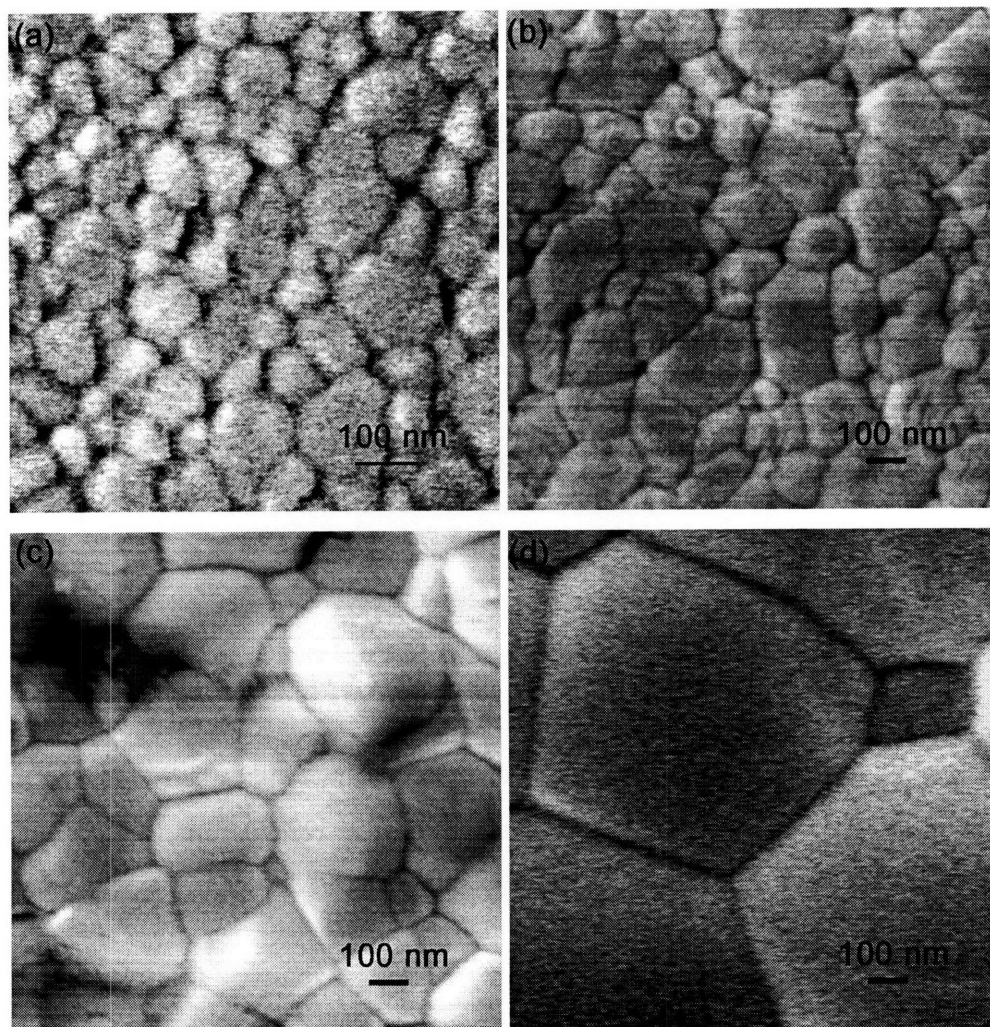
Figure 4.1 SEM images of 3YZ with a grain size of (a) ~ 90 nm, (b) ~ 150 nm, (c) ~ 330 nm, and (d) ~ 1.1 μm.
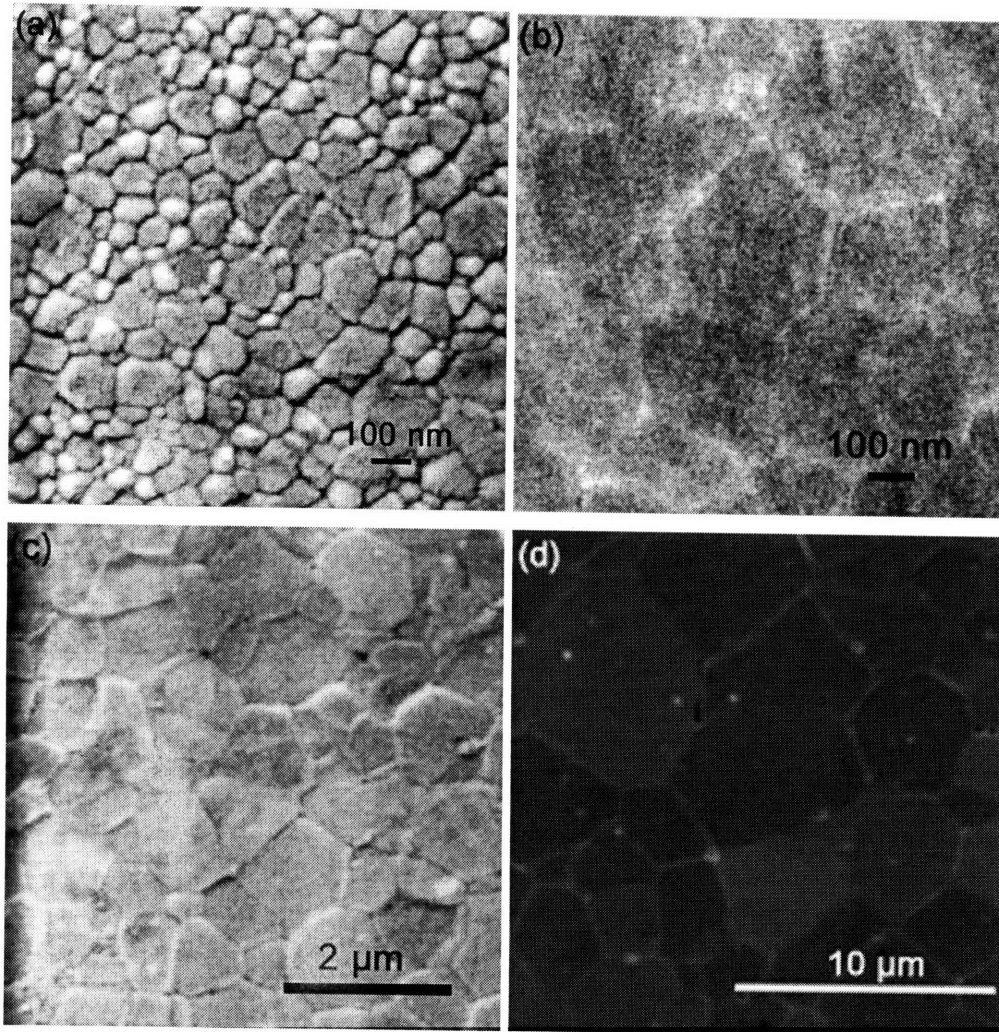
Figure 4.2 ESEM/SEM images of 8YZ with a grain size of (a) ~ 150 nm, (b) ~ 350 nm, (c) ~ 850 nm, and (d) ~ 5.0 μm

Our study indicated that there was no detectable difference in mechanical properties between ceramics derived by hydrothermal treatment and from commercial powders for a given grain size. Thus, no specification on the source of ceramics would be made in the following discussion.
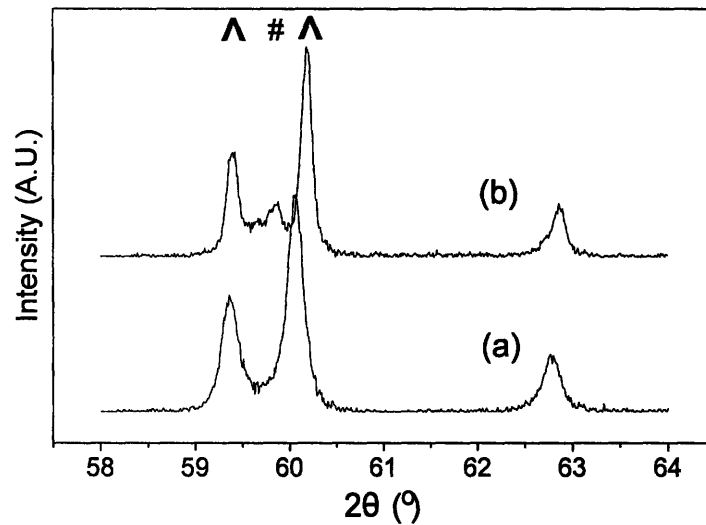
Figure 4.3 XRD patterns of 3YZ with a grain size of (a) 250 nm and (b) 1.0 μm. Peaks of the tetragonal and cubic phases were denoted by ^ and #, respectively.

4.3.2 Mechanical Properties

Vickers hardness H_V, Young's modulus E, and fracture toughness K_C were studied as a function of ceramic grain size. All ceramic samples examined were > 99% dense. Thus, the effect of porosity on mechanical properties, as discussed by various reports,[5,13] was minimized.

4.3.2.1 Vickers Hardness

Microhardness Studies

As observed previously with grain sizes in the submicron and micron regimes, 3YZ demonstrated the Hall-Petch effect, i.e. increased hardness with decreased grain size. This is due to an induced resistance to deformation from the pile-up of dislocations at grain boundaries, with Vickers hardness H_V being proportional to $D^{-\frac{1}{2}}$, where D is the average ceramic grain size.[2,14] This effect was extended to the nanometer regime, as shown in Figure 4.4. Under the test condition examined, a Vickers hardness of 14.0–19.6 GPa was obtained for 3YZ. 8YZ followed a similar trend at larger grain sizes (Figure 4.5). However, Vickers hardness remained essentially unchanged instead of further increasing with increasing $D^{-\frac{1}{2}}$, as the grain size was decreased below 350 nm.
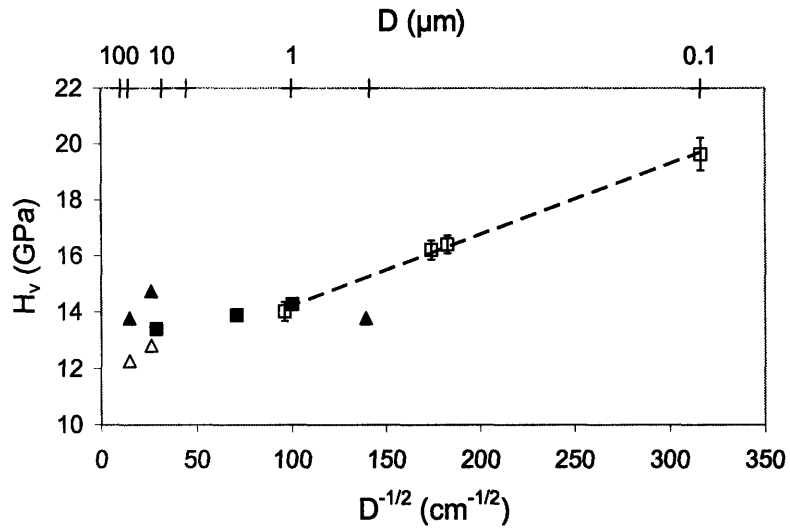
Figure 4.4 Vickers hardness as a function of grain size for 3YZ under a load of (▲) 0.1 kg,^{2} (□) 0.3 kg (this work), (△) 0.5 kg,^{2} and (■) 1 kg.[14]
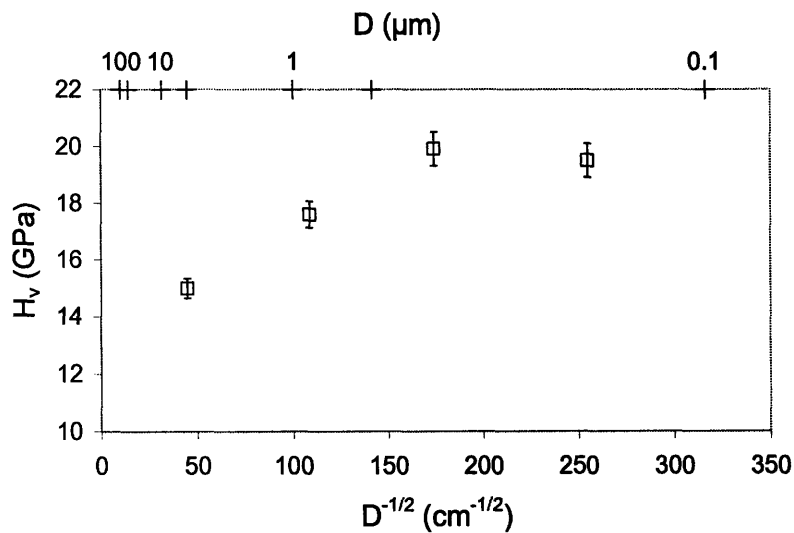
Figure 4.5 Vickers hardness as a function of grain size for 8YZ under a load of 0.3 kg.

Nanohardness Studies

The indentation area would be reduced when the load was decreased. As the indentation area A approached the sample's average grain size D, the Hall-Petch effect would no longer apply because this model assumes plasticity among many grains. This was illustrated in both 3YZ and 8YZ (Figure 4.6 and Figure 4.7, respectively). However, when hardness was represented as a function of A/D^2, which characterized the number of grains

103

affected by the indenter, a peak in H_V value was observed when A/D^2 approached ~ 10 (Figure 4.8). Student t-test analysis confirmed that this local maximum in indentation hardness was a statistically higher value than the value obtained at other points ($p \ll 0.01$).
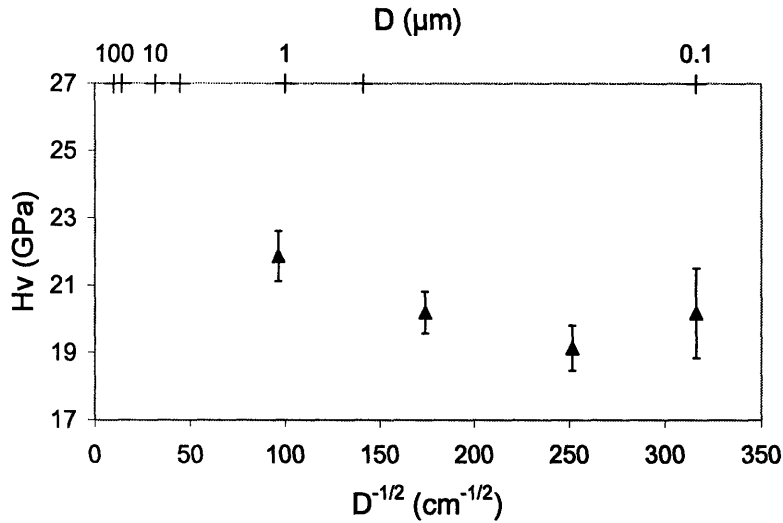
Figure 4.6 Vickers hardness as a function of grain size for 3YZ under a load of 0.5 N (0.05 kg).
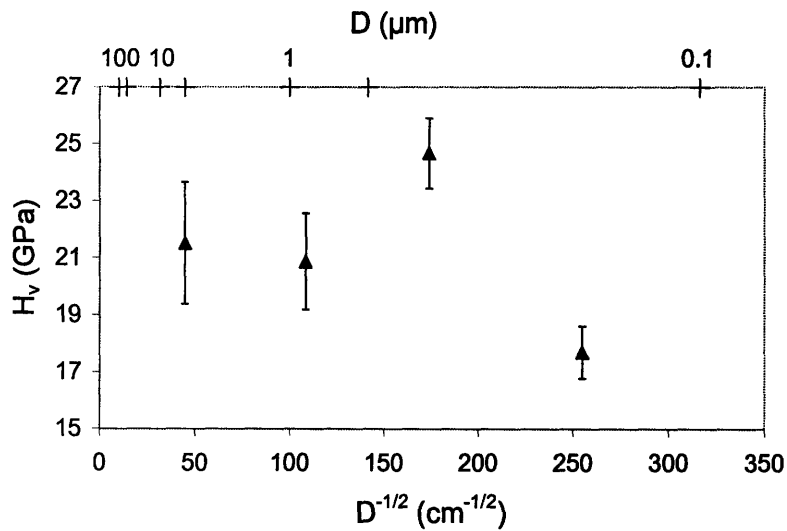
Figure 4.7 Vickers hardness as a function of grain size for 8YZ under a load of 0.06 N (0.006 kg).
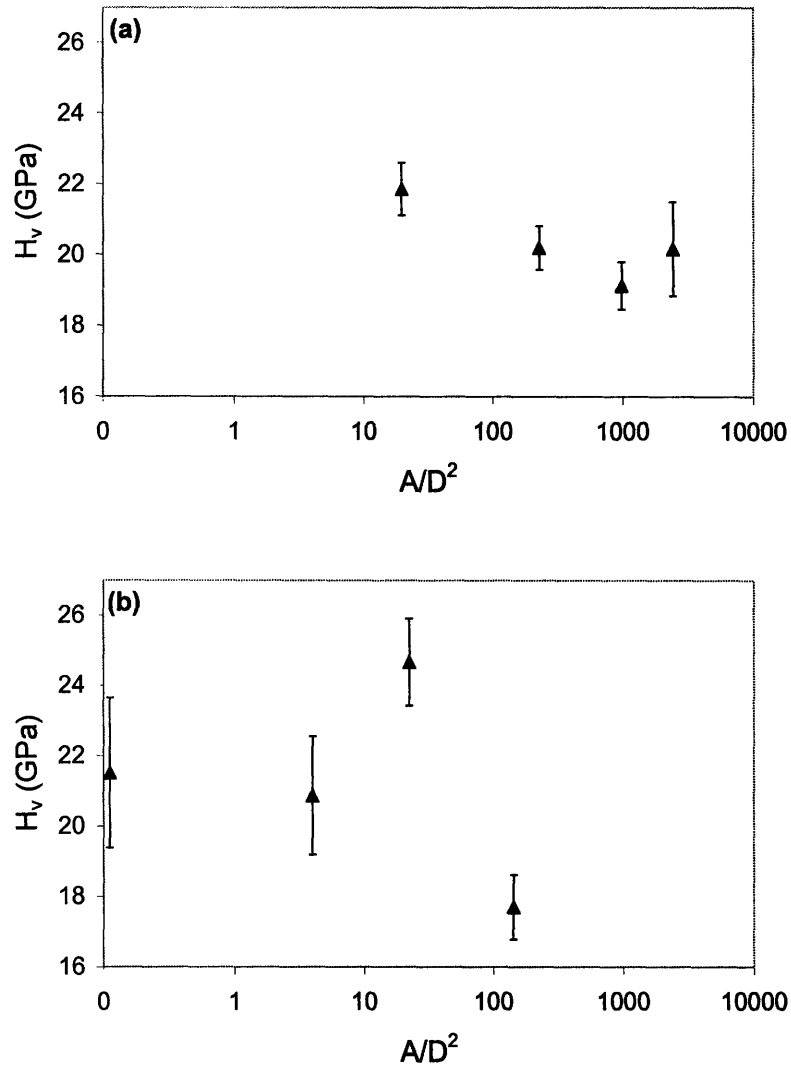
Figure 4.8 Vickers hardness as a function of A/D^2 for (a) 3YZ under a load of 0.5 N (0.05 kg) and (b) 8YZ under a load of 0.06 N (0.006 kg).

Fully dense polycrystalline ceramics show a lower hardness than their single crystal counterparts.[15] This implies that grain boundary motion (local strain accommodation mechanisms) can contribute towards decreasing the resistance to plastic flow. Therefore, as the indentation area approaches the same dimension as the average grain size of a ceramic, the hardness value is expected to increase and approach the value of the single crystal. On the other hand, however, the grain boundaries create barriers for the plastic deformation for each individual grain.[2] When the number of grains affected by the indenter was large, the first

factor was not significant, as observed in the microhardness studies (Figure 4.4 and Figure 4.5) Therefore, the 'pinning' of grain boundaries to the dislocation was the dominant mechanism, resulting in an increase in H_V as the grain size decreased. Since the sample volume affected by the indenter was larger than the size of the indentation itself, the two factors mentioned were balanced at $A/D^2 \sim 10$ in both systems, reaching a local maximum value in H_V.

4.3.2.2 Young's Modulus

Based on Oliver and Pharr's analysis of the load-depth responses,[8,9] Young's modulus of 3YZ and 8YZ were determined from the unloading curve of nanoindentation, while the formation of cracks were avoided by reducing the maximum load during indentation. The threshold for crack generation was listed in Table 4.2, and the loads applied for Young's modulus determination were 0.5 N and 0.06 N for 3YZ and 8YZ, respectively. The loading associated with crack initiation reached a peak at a grain size of $\sim$ 1 μm for 3YZ and $\sim$ 350 nm for 8YZ.

Table 4.2 Maximum indentation loading without crack formation.

	Grain Size (nm)	Maximum Indentation Loading (N) Without Crack Initiation	Increments in Loading (N)
3YZ	90	0.5	
	150	2.0	0.25
	330	2.5	
	1080	5.0	
8YZ	150	0.085	
	350	0.165	0.01
	850	0.100	
	5000	0.060	

Figure 4.9 and Figure 4.10 show that the Young's moduli of the yttria-zirconia ceramics were reduced with decreasing grain size. Young's modulus was lowered from 320 GPa to 221 GPa for 3YZ as the grain size decreased from 1.1 μm to 100 nm. Young's modulus was decreased from 386 GPa to 262 GPa for 8YZ as the grain size varied from 5.0

μm to 150 nm. Reduction of Young's modulus with decreasing grain size was also observed by Chaim and Hefetz in the 3YZ system,[13] and predicted for MgO by the calculation of Yeheskel et al. through a percolation model.[16] Yeheskel et al.'s model[16] and Chaim's model[17] stated that the physical properties of a material depend on those of its constituents and their respective volume fractions. The property associated with one component would become measurable only if the volume fraction of this component reached a critical value (percolation threshold). In contrast to nanocrystalline metals, the grain boundary in nanocrystalline ceramics has a considerable effective thickness due to the ionic/covalent nature of the interatomic bonding. It is presumed that the effective elastic modulus of the grain boundary region is lower than that of the grain interior. As a result, when grain size is reduced sufficiently such that the grain boundary represents a significant volume fraction, the elastic modulus of the nanocrystalline ceramic is expected to decrease. The grain size at which the elastic modulus started to decrease was larger than that reported by Chaim and Hefetz[13] (< 70 nm), but the reduction in elastic modulus was not as dramatic as that observed for this same material (3YZ) by Chaim and Hafetz.[13] This difference could be explained by the existence of either a greater grain boundary thickness or a lower percolation threshold for the grain packing in the percolating network of our materials, compared to that of Chaim and Hefetz.[13]
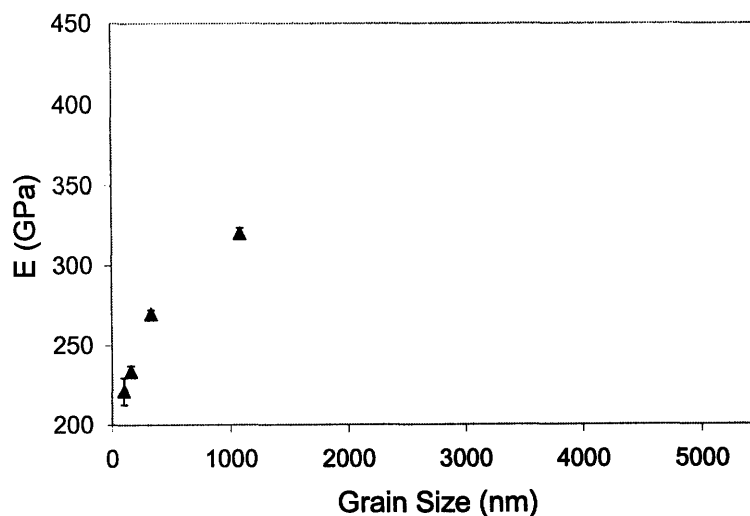

Figure 4.9 Young's modulus as a function of grain size for 3YZ under a load of 0.5 N.
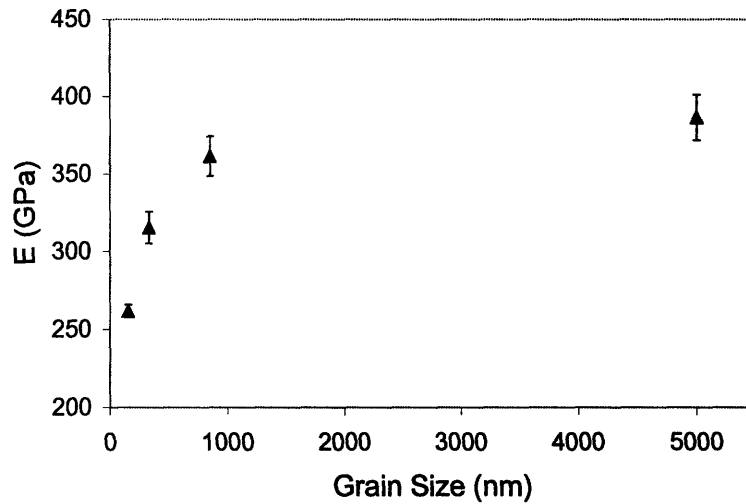
Figure 4.10 Young's modulus as a function of grain size for 8YZ under a load of 0.06 N.

4.3.2.3 Fractography of Indentation Area

Anstis *et al.* have reported that the fractography of Vickers indentation was affected by the relative grain size with respect to fracture length.[11] For grain size $D \ll$ fracture length c, an intergranular fracture path was observed. As D approached c, a heavily disrupted pattern was noted. For $D \gg c$, a transgranular fracture path was shown. However, these findings only partially agreed with our observations.

Figure 4.11(b), (c) and (d) showed that the 3YZ system followed the expected intergranular fracture path for $0.007 \leq D/c \leq 0.05$. This could be explained by the higher stress concentrations over grain boundary facets in ceramics with small grain sizes.[15] However, as the grain size decreased further to ~ 100 nm ($D/c = 0.003$), a transgranular fracture was observed (Figure 4.11(a)). Similar transgranular fracture was observed in 8YZ ceramics for $D/c \ll 1$ (Figure 4.12(a) and (b)). In fact, a transgranular fracture path dominated over a broader range of D/c values (0.006–0.5) for 8YZ, and no intergranular fractures were observed (Figure 4.12(c) and (d)). In our studies, the ceramic samples were essentially fully dense, allowing fractography to be examined for ultrafine-grained systems without the complication of porosity. The dominance of the transgranular fracture path within nanocrystalline 3YZ and submicron 8YZ could be due to a larger area of influence for the enhanced stress concentration along the grain boundaries compared to the grains. Assuming

108

this stress concentration area was comparable in 3YZ and 8YZ, the relative strength of grain interior and grain boundary in 3YZ would have increased more dramatically than that in 8YZ as the grain sizes increased. However, more detailed studies would be needed to confirm this speculation.
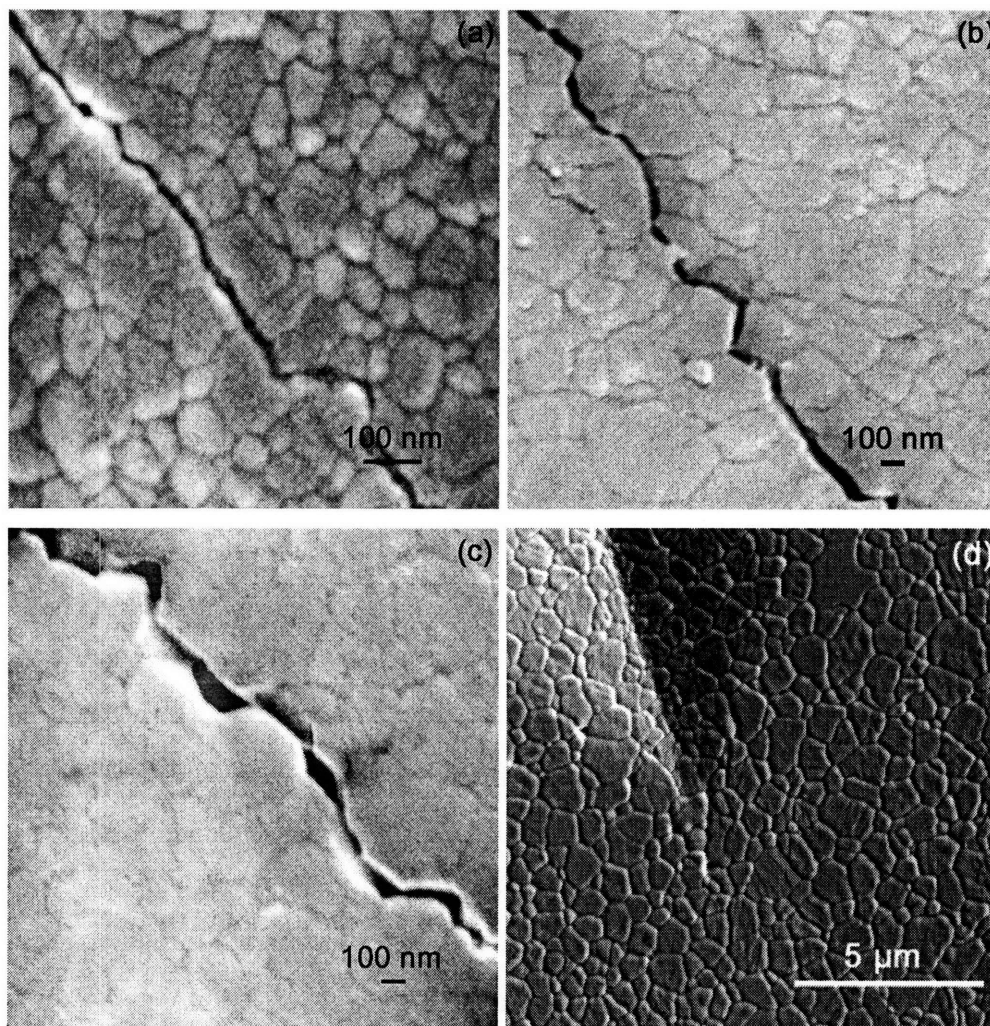
Figure 4.11 Fractography of 3YZ with a grain size of (a) ~ 100 nm (D/c ~ 0.003 << 1), (b) ~ 150 nm (D/c ~ 0.007 << 1), (c) ~ 330 nm (D/c ~ 0.02 << 1), and (d) ~ 1.1 μm (D/c ~ 0.05 < 1), after indentation at 1 kgf for 15 sec.
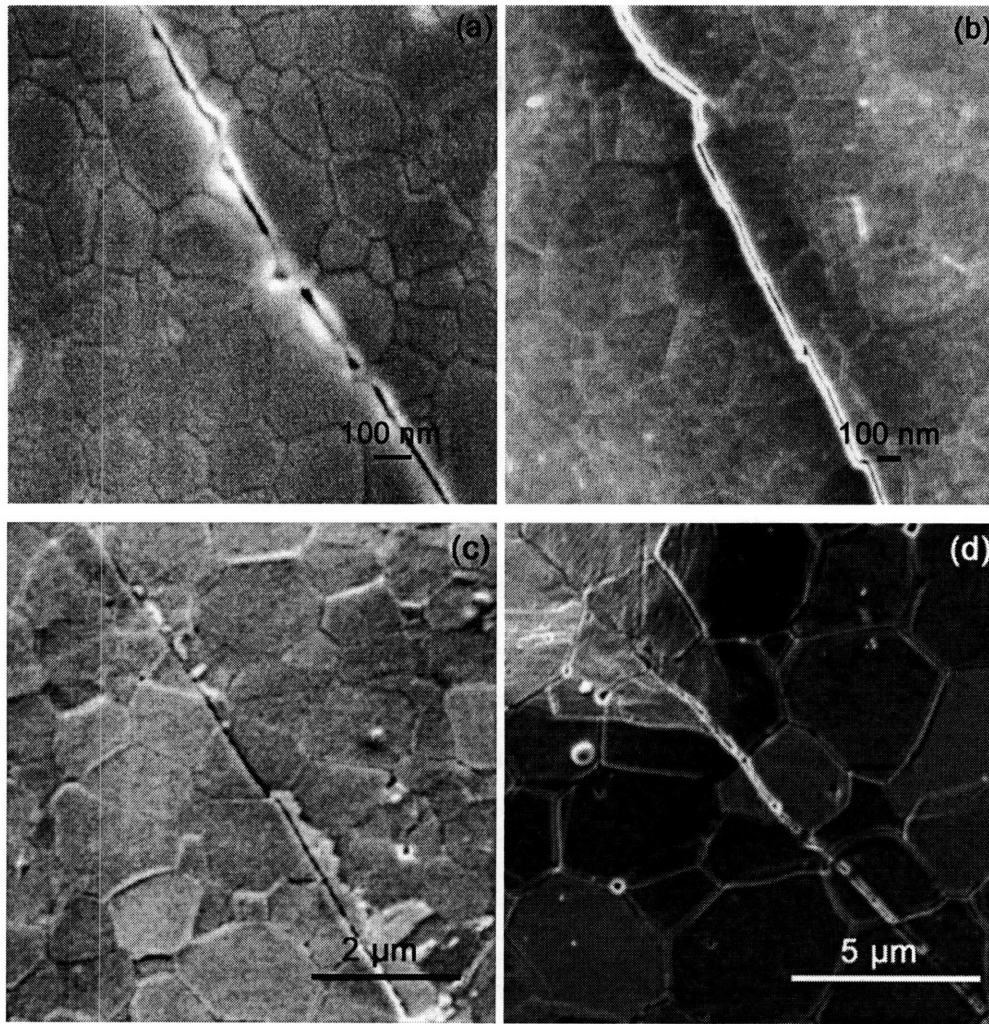
Figure 4.12 Fractography of 8YZ with a grain size of (a) ~ 150 nm (D/c ~ 0.006 << 1), (b) ~ 350 nm (D/c ~ 0.01 << 1), (c) ~ 850 nm (D/c ~ 0.03 << 1), and (d) ~ 5.0 μm (D/c ~ 0.5), after indentation at 0.3 kgf for 15 sec.

4.3.2.4 Fracture toughness

As the fracture path changed from intergranular to transgranular with decreasing grain size, 3YZ showed a reduction in fracture toughness (Figure 4.13).

Cottom and Mayo[18] have suggested that the thermal stability of ultrafine tetragonal grains prevented the transformation toughing of 3YZ. This might have given rise to the almost 3-fold reduction in fracture toughness from 7.9 MPa·m$^{-1/2}$ to 3.1 MPa·m$^{-1/2}$ as the grain size was reduced from 1.1 μm to 100 nm (Figure 4.13). Assuming the strength of grain boundary remained unchanged as the grain size varied, this inability for phase transformation

in 3YZ suggested a weakening of the grain interior, which would contribute to the transformation from intergranular fracture to transgranular fracture as the grain size of 3YZ was reduced to 100 nm (Figure 4.11). Cottom and Mayo[18] also noted a reduction in fracture toughness from 8.2 MPa·m$^{-1/2}$ to 2.25–4.25 MPa·m$^{-1/2}$ when the grain size of their 3YZ samples was reduced from 1.4 µm to 55–160 nm. However, their samples varied in porosity from 90.4 % to 99.3%.

Compared to 3YZ, 8YZ showed much lower fracture toughness values, with only very minor reduction in fracture toughness with decreasing grain size (Figure 4.14). Similar observations were made by Anselmi-Tamburini *et al.* in their plasma-sintered 8YZ samples.[6] The minor reduction in 8YZ fracture toughness with decreasing grain size also agreed with the common observation for cubic materials in the micron regime.[15] The existence of transformation toughening provided for the higher fracture toughness value of 3YZ compared to 8YZ.[19] Likewise, the prevention of transformation toughening in 3YZ gave rise to the strong dependence of fracture toughness on grain size.
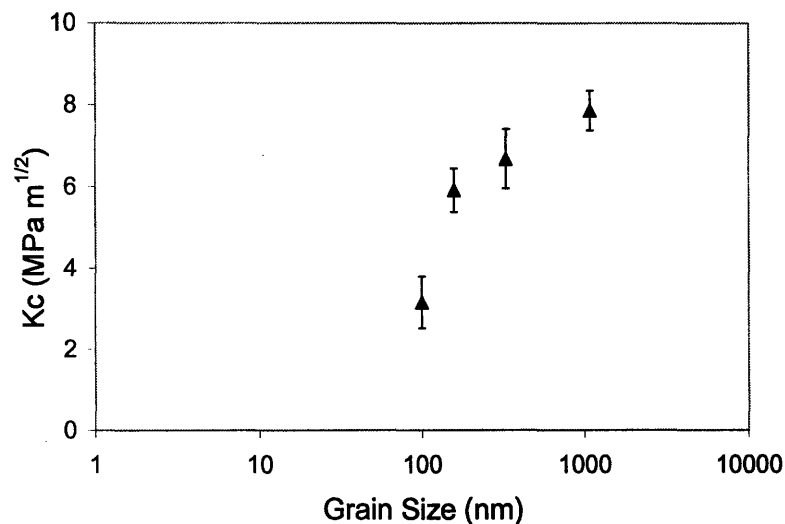
Figure 4.13 Fracture toughness as a function of grain size for 3YZ, after indentation at 1 kgf for 15 sec.

Kc (MPa m$^{1/2}$)
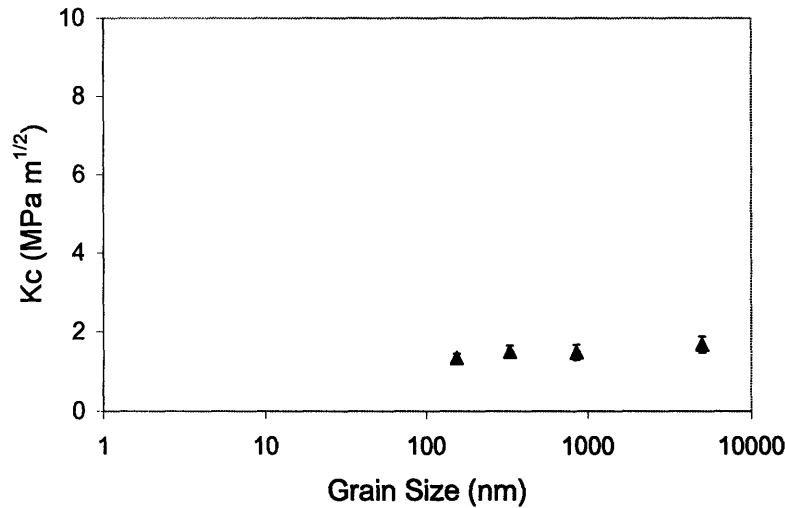
Grain Size (nm)

Figure 4.14 Fracture toughness as a function of grain size for 8YZ, after indentation at 0.3 kgf for 15 sec.

4.4 Summary

3YZ and 8YZ were successfully densified and stabilized in tetragonal and cubic phases, respectively. The mechanical properties of these yttria-zirconia ceramics were examined as a function of grain size systematically in the nanometer and micrometer regimes.

The Hall-Petch effect was found to be extended to the nanocrystalline regime for 3YZ, with Vickers hardness H_V being proportional to $D^{-\frac{1}{2}}$. 8YZ showed the Hall-Petch effect only in the micrometer and submicrometer regimes. Vickers hardness remained essentially unchanged for 8YZ as the grain size was decreased into the nanocrystalline regime. Maximum H_V values of 19 and 20 GPa were achieved for 3YZ and 8YZ, respectively. Local conditions would become significant when the indentation load was reduced, affecting the Vickers hardness values. A local maximum value in H_V was obtained at $A/D^2 \sim 10$ for both 3YZ and 8YZ.

A continuous decrease in Young's modulus with decreasing grain size was observed in both 3YZ and 8YZ. Young's modulus was decreased from 320 GPa to 221 GPa as the grain size decreased from 1.1 µm to 100 nm. Young's modulus was reduced from 386 GPa to 262 GPa for 8YZ as the grain size was varied from 5.0 µm to 150 nm. Such reduction could be partially explained by a percolative composite model.

Trans   granular fracture was observed in 3YZ as the grain size approached ~ 100 nm. This was in contrast with the dominant intergranular fracture mode observed in ceramics with fine grain sizes. Transgranular fracture was found in 8YZ over an even broader range of grain sizes (150 nm to 5.0 μm).

A significant reduction in fracture toughness from 7.9 $MPa \cdot m^{-1/2}$ to 3.1 $MPa \cdot m^{-1/2}$ was observed as the grain size was reduced from 1.1 μm to 100 nm in 3YZ. Compared to 3YZ, fracture toughness was much lower for 8YZ, and showed little dependence on grain size. For 3YZ, transformation toughening could account for the high facture toughness at larger grain sizes, while the enhanced stability of tetragonal phase at finer grain sizes would explain the reduced fracture toughness and the transformation from the intergranular to transgranular fracture mode with decreasing grian size.

4.5 References

[1]R. Vassen, D. Stover, "Processing and properties of nanophase ceramics," *J. Mater. Process. Technol.*, 93 77-84 (1999).

[2]R. W. Rice, C. C. Wu, F. Borchelt, "Hardness grain-size relations in ceramics," *J. Am. Ceram. Soc.*, 77 [10] 2539-2553 (1994).

[3]E. S. Ahn, N. J. Gleason, A. Nakahira, J. Y. Ying, "Nanostructure processing of hydroxyapatite-based bioceramics," *Nano Lett.*, 1 [3] 149-153 (2001).

[4]E. S. Ahn, N. J. Gleason, J. Y. Ying, "The effect of zirconia reinforcing agents on the microstructure and mechanical properties of hydroxyapatite-based nanocomposites," *J. Am. Ceram. Soc.*, 88 [12] 3374-3379 (2005).

[5]O. Vasylkiv, Y. Sakka, V. V. Skorokhod, "Low-temperature processing and mechanical properties of zirconia and zirconia-alumina nanoceramics," *J. Am. Ceram. Soc.*, 86 [2] 299-304 (2003).

[6]U. Anselmi-Tamburini, J. E. Garay, Z. A. Munir, A. Tacca, F. Maglia, G. Chiodelli, G. Spinolo, "Spark plasma sintering and characterization of bulk nanostructured fully stabilized zirconia: Part II. Characterization studies," *J. Mater. Res.*, 19 [11] 3263-3269 (2004).

[7]J. Cui, J. Y. Ying, to be submitted.

[8]W. C. Oliver, G. M. Pharr, "Measurement of hardness and elastic modulus by instrumented indentation: Advances in understanding and refinements to methodology," *J. Mater. Res.*, 19 [1] 3-20 (2004).

[9]W. C. Oliver, G. M. Pharr, "An improved technique for determining hardness and elastic-modulus using load and displacement sensing indentation experiments," *J. Mater. Res.*, 7 [6] 1564-1583 (1992).

[10]K. Niihara, R. Morena, D. P. H. Hasselman, "Evaluation of K_{Ic} of brittle solids by the indentation method with low crack-to-indent ratios," *J. Mater. Sci. Lett.*, 1 [1] 13-16 (1982).

[11]G. R. Anstis, P. Chantikul, B. R. Lawn, D. B. Marshall, "A critical evaluation of indentation techniques for measuring fracture-toughness: I, Direct crack measurements," *J. Am. Ceram. Soc.*, 64 [9] 533-538 (1981).

[12]K. Matsui, H. Horikoshi, N. Ohmichi, M. Ohgai, H. Yoshida, Y. Ikuhara, "Cubic-formation and grain-growth mechanisms in tetragonal zirconia polycrystal," *J. Am. Ceram. Soc.*, 86 [8] 1401-1408 (2003).

[13]R. Chaim, M. Hefetz, "Effect of grain size on elastic modulus and hardness of nanocrystalline ZrO_2-3 wt% Y_2O_3 ceramic," *J. Mater. Sci.*, 39 [9] 3057-3061 (2004).

[14]S. Higuchi, Y. Takeda, K. Maeda, T. Miyoshi, "Effect of reducing grain-size on mechanical-properties of stabilized ZrO_2 ceramics," *J. Ceram. Soc. Jpn.*, 96 [10] 997-1002 (1988).

[15]R. W. Rice, "Grain dependence of microcracking, crack propagation, and fracture toughness at ~ 22°C" and "Grain dependence of indentation hardness at ~ 22°C"; pp. 43-126, 245-294 in *Mechanical Properties of Ceramics and Composites: Grain and Particle Effects*, Marcel Dekker, New York, NY, (2000).

[16]O. Yeheskel, R. Chaim, Z. J. Shen, M. Nygren, "Elastic moduli of grain boundaries in nanocrystalline MgO ceramics," *J. Mater. Res.*, 20 [3] 719-725 (2005).

[17]R. Chaim, "Percolative composite model for prediction of the properties of nanocrystalline materials," *J. Mater. Res.*, 12 [7] 1828-1836 (1997).

[18]B. A. Cottom, M. J. Mayo, "Fracture toughness of nanocrystalline ZrO_2-3 mol% Y_2O_3 determined by Vickers indentation," *Scr. Mater.*, 34 [5] 809-814 (1996).

[19]A. G. Evans, A. H. Heuer, "Transformation toughening in ceramics – Martensitic transformations in crack-tip stress-fields," *J. Am. Ceram. Soc.*, 63 [5-6] 241-248 (1980).

Chapter 5 – Conclusions and Recommendations for Future Work

5.1 Conclusions

This thesis examined nanocrystalline yttria-zirconia powders and ceramics for catalytic and structural ceramic applications. Nanocrystals of 7 mol% Y_2O_3-ZrO_2 (7YZ) were synthesized with ultrafine grain sizes and high surface areas by chemical co-precipitation. They were modified with secondary components, such as Al_2O_3, TiO_2, CeO_2 and Mn_2O_3, in the form of coating or dopants. The resulting nanocomposites demonstrated improved thermal stability and catalytic activity in the flameless combustion of methane. In particular, 25 wt% Mn_2O_3-coated 7YZ and 25 wt% Mn_2O_3-doped 7YZ showed remarkably low light-off temperatures of 375°C and 358°C, respectively. These catalysts were highly attractive as they were competitive with the much more expensive supported noble metal catalysts. Their catalytic activity could be attributed to the availability of active surface oxygen species, which facilitated the methane activation at low temperatures.

Nanocrystalline 3 mol% and 8 mol% Y_2O_3-ZrO_2 (3YZ and 8YZ) were successfully densified with an ultrafine grain size of < 90 nm by pressureless sintering at 1100°C and 1150°C, respectively. The low-temperature sinterability could be attributed to the well-defined nanocrystalline particles obtained via hydrothermal synthesis, and the effective elimination of secondary porosity through the dry compact processing. Submicron-sized 3 mol% Y_2O_3-ZrO_2 ceramics with a grain size of ~ 150 nm was also obtained with commercial TOSOH© powders. Grain growth during densification of TOSOH© powders was successfully suppressed by presintering to 93% density under an argon atmosphere (i.e. at 1300°C), followed by hot isostatic pressing in argon at a temperature lower than the presintering temperature (i.e. 1200°C).

Using different starting powders and processing approaches, dense 3YZ and 8YZ ceramics with controlled grain sizes of ≥ 85 nm could be attained. This allowed for the systematic studies of various ceramic properties as a function of grain size in the nanometer and micrometer regimes. The Hall-Petch effect was found to be extended to the nanocrystalline regime for 3YZ, with Vickers hardness H_V being proportional to $D^{-1/2}$. 8YZ showed the Hall-Petch effect only in the micrometer and submicrometer regime. Vickers

115

hardness remained essentially unchanged for 8YZ as the grain size was decreased below 350 nm. Maximum H_V values of 19 and 20 GPa were achieved for 3YZ and 8YZ, respectively. Local conditions would become significant when the indentation load was reduced, affecting the Vickers hardness values. A local maximum value in H_V was obtained at $A/D^2 \sim 10$ for both 3YZ and 8YZ.

A continuous decrease in Young's modulus with decreasing grain size was observed in both 3YZ and 8YZ. Young's modulus was decreased from 320 GPa to 221 GPa for 3YZ as the grain size decreased from 1.1 μm to 100 nm. Young's modulus was reduced from 386 GPa to 262 GPa for 8YZ as the grain size was varied from 5.0 μm to 150 nm. Transgranular fracture was observed in 3YZ as the grain size approached ~ 100 nm. This was in contrast with the dominant intergranular fracture mode observed in ceramics with fine grain sizes. Transgranular fracture was found in 8YZ over an even broader range of grain sizes (150 nm to 5.0 μm). A significant reduction in fracture toughness from 7.9 MPa·m$^{-1/2}$ to 3.1 MPa·m$^{-1/2}$ was observed as the grain size was reduced from 1.1 μm to 100 nm in 3YZ. Fracture toughness was much lower for 8YZ than for 3YZ, and showed little dependence on grain size.

5.2 Recommendations for Future Work

25 wt% Mn$_2$O$_3$-doped 7YZ showed the lowest light-off temperature of 358°C among the yttria-zirconia-based nanocomposite catalysts tested. However, its methane combustion activity would decay at high temperatures due to grain growth. In contrast, CeO$_2$-coated 7YZ showed superior thermal stability to 950°C in preliminary studies. Therefore, it would be of interest to develop Mn$_2$O$_3$-doped 7YZ with CeO$_2$ coating to further optimize the light-off temperature and thermal stability of the yttria-zirconia-based nanocomposite catalysts.

Fully dense nanocrystalline yttria-zirconia ceramics have been achieved at low temperatures by pressureless sintering. This was accomplished by hydrothermal synthesis and dry compact processing. This combination of synthesis and processing could be broadly applied to other oxides to facilitate the densification of nanostructured ceramics. It would reduce the cost of ceramics sintering associated with conventional high-temperature and high-pressure processes, and allow ceramics with ultrafine grain sizes in the submicron and nanometer regimes to be achieved. The latter are of broad interest in both structural and

functional ceramic applications, and would allow for the systematic studies of mechanical, electrical and optical properties as a function of grain size.